MASS AND HEAT FLOW THROUGH SNOWPACKS

A Thesis Submitted to the College of

Graduate and Postdoctoral Studies

In Partial Fulfillment of the Requirements

For the Degree of Doctorate of Philosophy

In the Department of Geography and Planning

(Centre for Hydrology)

University of Saskatchewan

Saskatoon

By

NICOLAS ROMAIN LEROUX

PERMISSION TO USE

In presenting this thesis/dissertation in partial fulfillment of the requirements for a Postgraduate degree from the University of Saskatchewan, I agree that the Libraries of this University may make it freely available for inspection. I further agree that permission for copying of this thesis/dissertation in any manner, in whole or in part, for scholarly purposes may be granted by the professor or professors who supervised my thesis/dissertation work or, in their absence, by the Head of the Department or the Dean of the College in which my thesis work was done. It is understood that any copying or publication or use of this thesis/dissertation or parts thereof for financial gain shall not be allowed without my written permission. It is also understood that due recognition shall be given to me and to the University of Saskatchewan in any scholarly use which may be made of any material in my thesis/dissertation.

DISCLAIMER

Reference in this thesis/dissertation to any specific commercial products, process, or service by trade name, trademark, manufacturer, or otherwise, does not constitute or imply its endorsement, recommendation, or favouring by the University of Saskatchewan. The views and opinions of the author expressed herein do not state or reflect those of the University of Saskatchewan, and shall not be used for advertising or product endorsement purposes.

Requests for permission to copy or to make other uses of materials in this thesis/dissertation in whole or part should be addressed to:

Head of the Department of Geography and Planning
117 Science Place
University of Saskatchewan
Saskatoon, Saskatchewan S7N 1J9
Canada

OR

Dean
College of Graduate and Postdoctoral Studies
University of Saskatchewan
116 Thorvaldson Building, 110 Science Place
Saskatoon, Saskatchewan S7N 5C9
Canada

ABSTRACT

Accurate estimation of snowmelt runoff is of primary importance in streamflow prediction for water management and flood forecasting in cold regions. Lateral flow, preferential flow pathways, and distinctive wetting and drying water retention curves in porous media have proven critical to improving soil water flow models; the most sophisticated physically based snowmelt models only account for 1D matrix flow and employ a single drying water retention curve for both drying and wetting snowpacks. Thus, there is an immediate need to develop snowmelt models that represent lateral and preferential flows, as well as full capillary hysteresis to examine the potential to improve snowmelt hydrological modelling. In this dissertation, the primary objective is to improve understanding and prediction of water flow through snow by investigating the formation of preferential flow paths and the coupling of heat and mass fluxes within snow. Of particular interest is the prediction of capillary pressure at macroscale, as it is of importance for simulating preferential flow in porous media. A novel 2D numerical model is developed that enables an improved understanding of energy and water flows within deep heterogeneous snowpacks on flat and sloping terrains. The numerical model simulates vertical and lateral water flow through snow matrix and preferential flow paths, and accounts for hysteresis in capillary pressure, internal energy fluxes, melt at the surface, and internal refreezing. Implementing a water entry pressure for initially dry snow was necessary for the formation of preferential flow paths. By coupling the simulation of preferential flow with heat transfer, ice layer formation was realistically simulated when water infiltrated an initially cold snowpack. Heat convection was added to the model and coupled to the energy balance at the snow surface; the transfer of heat by topography-driven airflow affected the estimated snow surface temperature by transporting thermal energy from the warm snow-soil interface to the upper snowpack. Comparisons of the model meltwater flow predictions against snowmelt field data revealed limitations in the current theories of water flow through snow, such as the use of a capillary entry pressure in the snow water retention curve that is limited to high-density snow. This suggested further concepts that would improve the representation of capillary pressure in snow models. This improved model, which considers a dynamic capillary pressure, gave better results than models based on previous theories when simulating capillary pressure overshoot. The research demonstrates how heterogeneous flow through snow can be modelled and how this research model furthers understanding of snowmelt flow processes and potential improvements in snowmelt-derived streamflow prediction.

ACKNOWLEDGEMENTS

I would like first to acknowledge my supervisor, Dr. John Pomeroy, for giving me the opportunity to work on this interesting project, his support and his mentorship. Thank you to Joni Onclin and Phyllis Baynes for your logistical help. I am very grateful to my family for supporting me during the whole course of my studies while being far from home. A very special thank you to Nik Aksamit, Claire Aksamit, and Dan Karran for constant encouragement, support, and all those long discussions over coffee breaks. Thank you to my colleagues and friends at the Centre for Hydrology, Paul Whitfield, Seba Krogh, Lucia Scaff, Chris Marsh, Phil Harder, Hailey Robichaud for your encouragement, feedback, and support, and to the postdocs I had the chance to meet and interact with along the way, Keith Musselman, Jono Conway, and Nic Wayand. Special thanks to May Guan and Angus Duncan for their help with fieldwork and all those long fun hours in the field. Finally, thank you to my community in Canmore for our time together.

To my parents, for always supporting me.

TABLE OF CONTENTS

LIST OF TABLES

LIST OF FIGURES

LIST OF ABBREVIATIONS

PFP (Preferential Flow Paths)

ROS (Rain-On-Snow)

WRC (Water Retention Curve)

SMPP (Snowmelt Model with Preferential flow Paths)

LIST OF SYMBOLS

In the following, the subscript k denotes one of the three phases that compose the snowpack (a: air, w: water, i: ice)

The superscript p denotes either a wetting process or a drainage process (w and d, respectively)

θ_k: Volumetric content of the phase k [m^3 m^{-3}]

θ_{ws}: Volumetric content of the wetting phase at saturation [m^3 m^{-3}]

θ_{wr}: Irreducible water content [m^3 m^{-3}]

ρ_k : Density of the phase k [kg m^{-3}]

ρ_s: Density of snow [kg m^{-3}]

ρ_{ds}: Dry snow density [kg m^{-3}]

M_k: Mass of the phase k [kg]

V_k: Volume of the phase k [m^3]

ϕ: Porosity [m^3]

SWE: Snow Water Equivalent [m]

h: Snow depth [m]

z: Height [m]

β: slope angle [rad]

T: Snow internal temperature [K]

T_s: Snow surface temperature [K]

Q_n: Input energy flux at the snow surface [W m^{-2}]

Q_{inf}: Water infiltration flux [m s^{-1}]

V_n: Velocity of the melting surface [m s^{-1}]

L_f: Latent heat of fusion [J kg^{-1}]

L_v: Latent heat of vaporization [J kg^{-1}]

q: volumetric mass flux [m s^{-1}]

g: acceleration by gravity [9.81 m s^{-2}]

S_S: Mass source or sink term [s^{-1}]

K: Hydraulic conductivity [m s^{-1}]

k_{rw}: relative permeability of the wetting phase [-]

k_s: Snow permeability [m^2]

K_s: Saturated hydraulic conductivity [m s^{-1}]

P_{we}: Water entry capillary pressure [m]

P_c: Static capillary pressure [m]

$P_{c,d}$: Dynamic capillary pressure [m]

μ_w: Dynamic viscosity of water [Pa s]

r_{opt}: Optical grain radius [m]

r_c: Mean grain radius [m]

α^p: van Genuchten parameter [m]

n^p: van Genuchten parameter [-]

m^p: van Genuchten parameter [-]

S_w: Water saturation [-]

S_{wr}: Residual saturation [-]

κ_s: Thermal conductivity of snow [W m^{-1} K^{-1}]

κ_{eff}: Effective thermal conductivity [W m^{-1} K^{-1}]

κ_w: Thermal conductivity of water [W m^{-1} K^{-1}]

$C_{p,k}$: Specific heat capacity of the phase k [J kg^{-1} K^{-1}]

m_{max}: Maximum mass of liquid water per unit volume of snow that must freeze to raise the snow temperature to zero Celsius [kg m^{-3}]

m_f: Mass of liquid water per unit volume of snow that actually refreezes [kg m^{-3}]

γ: Scaling parameter [-]

f: Fraction of wet surface area over total area [m^2 m^{-2}]

τ: Relaxation coefficient [m s]

λ: Parameter [-]

A: Snow surface albedo

u_*: Friction velocity [m s^{-1}]

L_{in}/L_{out}: Incoming/outgoing longwave radiation [W m^{-2}]

K_{in}: Incoming shortwave radiation [W m^{-2}]

Q_{net}: Net radiation [W m^{-2}]

Q_{K}: Net shortwave radiation [W m^{-2}]

u: Wind speed [m s^{-1}]

Q_{H}: Sensible heat flux [W m^{-2}]

Q_{E}: Sensible heat flux [W m^{-2}]

Q_{cond}: Conductive heat flux [W m^{-2}]

ϵ: Snow emissivity [-]

σ: Stefan-Boltzmann constant [W m^{-2} K^{-4}]

U: Snow internal energy [J m^{-2}]

d_{o}: Displacement height [m]

$z_{0\mathrm{m}}/z_{0\mathrm{h}}/z_{0\mathrm{q}}$: Roughness length of momentum/heat transfer/ vapour transfer [m]

$\Psi_{\mathrm{m}}/\Psi_{\mathrm{h}}/\Psi_{\mathrm{q}}$: Atmospheric correction functions for momentum/ heat transfer/ vapour transfer

ΔT_{s}: Difference between maximum and minimum values of snow surface temperature [K]

L: Monin-Obukhov length [m]

P: Pressure of the air phase within the snowpack [Pa]

P_d: Pressure distribution at the snow surface [Pa]

Λ: Wavelength number of snow dunes [m]

CHAPTER 1

INTRODUCTION

1.1 Motivation and Relevance

Much of the global freshwater used for irrigation, power generation, and human consumption is derived from mountain catchments (*Viviroli et al.*, 2007, *Mankin et al.*, 2015). In these catchments, snow accumulates over the winter and produces runoff in spring and early summer, which is then available to downstream watersheds. (*Horton*, 1915) noted the need to gather information on the timing, magnitude, and quality of snowmelt for hydrological assessments. This information is crucial for water supply for irrigation use, hydroelectricity generation, and municipal consumption. These data also benefit snow ecological studies of the snowpack as the habitat of many living animals and plants (*Pomeroy and Brun*, 2001), and help researchers forecast floods, as fast snowmelt and rain-on-snow events can cause rapid and dramatic floods (e.g. *Sui and Koehler*, 2001), such as those in Alberta in June 2013 (*Pomeroy et al.*, 2016).

To predict the timing and magnitude of snowmelt runoff from deep snowpacks with accuracy, water flow percolation within snow must be understood and quantified (*Male and Gray*, 1975; *Wankiewicz*, 1979). Liquid water flow within a snowpack is influenced by internal properties of snow, and deeper, colder snowpacks have slower flow rates; this makes the process significant to mountain hydrology. Among these internal properties, ice layers and preferential flow paths (PFP) greatly impact the spatial and temporal distributions of snowmelt runoff (*Marsh and Woo*, 1984a; *Marsh*, 1991) A number of studies have focused on understanding ice layers and preferential flow formations and their impacts on meltwater routing. In addition, the hydraulic properties of snowpacks, such as the water retention curve, ice layer permeability, and grain growth rate with water saturation are still lacking verification against measurements in natural snowpacks; likewise, the development of PFP is still not well understood (*Marsh*, 1991). Many theories have described gravitational vertical flow percolation within a homogeneous, isothermal snowpack (*Colbeck*, 1972), water percolation through a subfreezing, layered snowpack with phase change (*Tseng et al.*, 1994), or the influence of capillary forces on water flow (*Jordan*, 1995); however, liquid water

flows not only vertically but also laterally within a snowpack (*Eiriksson et al.*, 2013), resulting in greater complications in estimating snowmelt runoff.

A new research numerical model that can simulate the formation of PFP has recently emerged (*Hirashima et al.*, 2014, 2017). This model is limited to water flow through snow and neglects heat flow through snow and important flow characteristics such as the hysteresis in the water retention curve. To date, no operational snow model is able to predict lateral flows, the formation of PFP and ice layers, and their effects on water flow through snow, resulting in inaccuracy in the prediction of catchment discharge. Models created using the Cold Region Hydrological Modelling platform (CRHM) (*Pomeroy et al.*, 2007) demonstrate this (*Pomeroy et al.*, 2016). The CHRM model of Marmot Creek Research Basin (surface area = 9.8 km^2), gives good overall results in estimating the peak discharge at moderate scales (Fang et al., 2013) but improvements are needed to accurately predict the timing of peak flow at smaller scales, such as the CRHM streamflow model for the alpine snowmelt dominated Upper Marmot Creek (surface area = 1.18 km^2), which estimated peak flow 17 days ahead of the measured peak streamflow in 2009 (Pomeroy et al., 2016). Though the causes of the early estimation of peak basin outflow are not known, the simplifications made in estimating internal snowmelt processes, such as ice layers and lateral flow, could be responsible for the inaccuracy. Accurately predicting the timing of peak streamflow is important for understanding ecohydrology and snow chemistry (e.g. *Quinton and Pomeroy*, 2006), and for forecasting floods from mountain creeks that can be destructive and have resulted in massive damage to communities, such as Canmore in 2013 (*Pomeroy et al.*, 2016). As the basin scale decreases, snow physics (e.g. water flow through snow) have greater impacts on streamflow prediction, and hydrological model applied at relatively small scales could greatly benefit from more physically-based and realistic representations of hydrological physical processes. In this regard, this research aims to improve the numerical prediction of water and heat flow through snow.

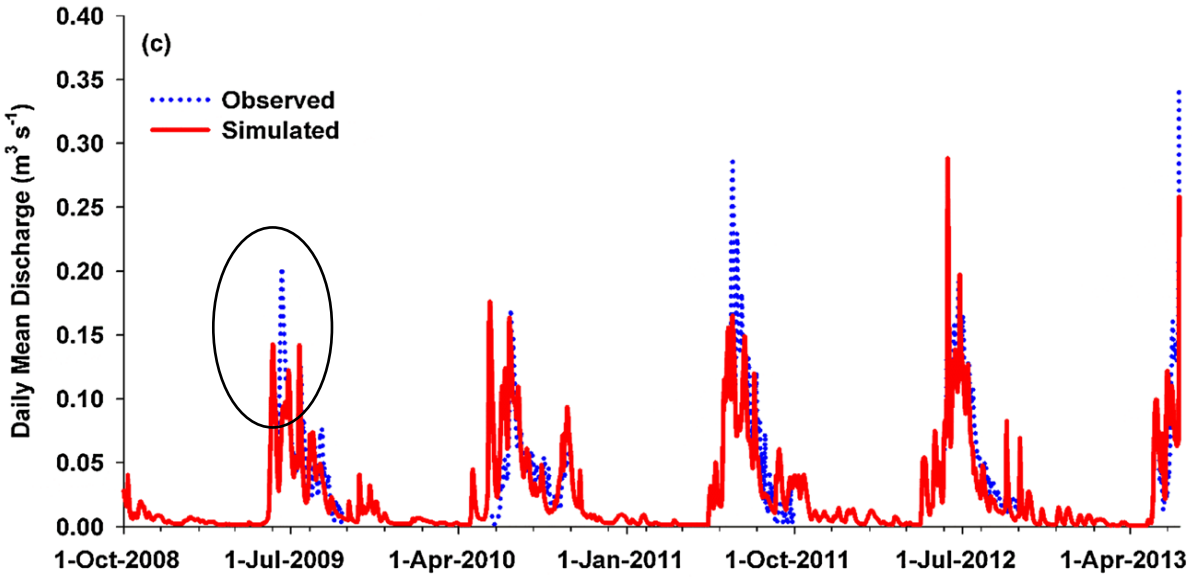

Figure 1.1 Daily discharge from Upper Marmot Creek. The circle shows an example where the estimated timing of the peak discharge, which is governed by snowmelt, does not correspond to the observation (*Pomeroy et al.*, 2016).

1.2 Background

This literature review describes the current knowledge on snowmelt processes and water flow through snow. Theories characterizing meltwater flow will be presented. However, few studies have been conducted on liquid water flow through a sloping snowpack, and current knowledge in this instance will be summarized. Finally, the most common physically based snow models will be presented and their limitations outlined.

1.2.1 Snow Properties

Snow is a porous medium composed of three phases: liquid water, ice and air, symbolized by the subscripts w, i and a, respectively. A snowpack is characterized by its mass (M_s), its volume (V_s), porosity (ϕ), density (ρ_s), height (h), its snow water equivalent (SWE), and the liquid water content snow is retaining (θ_w). These snow properties can be estimated using the following equations (*Dingman*, 2005):

$$V_s = V_i + V_w + V_a \tag{1.1}$$

$$M_s = M_i + M_w + M_a \tag{1.2}$$

$$\phi = \frac{V_a + V_w}{V_s} \tag{1.3}$$

$$V_i = (1 - \phi)V_s \tag{1.4}$$

$$\rho_s = \frac{\rho_i V_i + \rho_w V_w}{V_s} = (1 - \phi)\rho_i + \theta_w \rho_w \tag{1.5}$$

$$\theta_w = \frac{V_w}{V_s} \tag{1.6}$$

$$SWE = \frac{\rho_s}{\rho_w} h \tag{1.7}$$

The temperature of a snowpack is always less or equal to 0ºC. For snow to melt, its temperature must be equal to 0ºC, which is the equilibrium temperature at which liquid water and ice can coexist at atmospheric pressure.

Snow is deposited on the ground in layers of different snow types and different properties (density, grain size and shape, thickness, and liquid water content). The initial properties of these layers depend on the meteorological conditions during snow storms; a summary of type and shape of the precipitation particles is given in the International Classification for Seasonal Snow on the Ground (*Fierz et al.*, 2009). Layer properties are inhomogeneous within each layer and this impacts the flow of liquid water through snow has been demonstrated (*Hirashima et al.*, 2013). Grain size and shape evolve during the winter and spring seasons due to both dry and wet snow metamorphism (cf. review by *Colbeck*, 1982). Dry snow metamorphism occurs in dry and subfreezing snow and is caused by either strong temperature gradients within the snowpack (kinetic growth) that result in vapour gradients or by equilibrium growth due to differences in grain curvature. Wet snow metamorphism happens when snow grains are in contact with liquid water. Two wet snow metamorphism regimes have been differentiated: 1) the pendular regime (low water contents < ~7 %; *Denoth*, 1980) is characterized by liquid water at the contact point of the snow grains and the liquid phase is disconnected. In this regime, cohesive clusters of snow grains form. 2) In the funicular regime, the liquid phase is continuous within the pore space and snow metamorphism occurs rapidly. The snow clusters become less cohesive, resulting in weaker snow layers that can cause avalanching. In tis regime, snow grains are becoming rounder and bigger. *Brun* (1989) observed that grain growth in the funicular regime slows down when the liquid water content reaches ~10 %. Snowmelt and meltwater flow occurring before a snowpack becomes ripe will

directly be affected by the initial snow layering and crystal morphology that result from snow metamorphism and differences in initial precipitation particles.

1.2.2 Rain-On-Snow

Over the last century, rain-on-snow (ROS) events have been observed to occur more and more frequently in Canada, particularly during the spring and fall seasons (*Vincent and Mekis*, 2006; *Shook and Pomeroy*, 2012). ROS significantly impacts snowpack by accelerating its melt (*Marks et al.*, 1998), or decreasing its stability (*Conway and Raymond*, 1993). The acceleration of melt is caused by advected energy from rain to snow and an increase of latent heat towards the snowpack (*Marks et al.*, 1998), which results from high atmospheric humidity and warm air, which cause significant condensation on the snow surface. This increase in advected and latent energy input flux during ROS was also observed during the 2013 flood in Alberta (*Pomeroy et al.*, 2016). Figure 1.2 shows the shift in energy balance fluxes during the flood at Upper Marmot Creek, modelled using CRHM with the snowmelt model SNOBAL (*Marks and Dozier*, 1992).

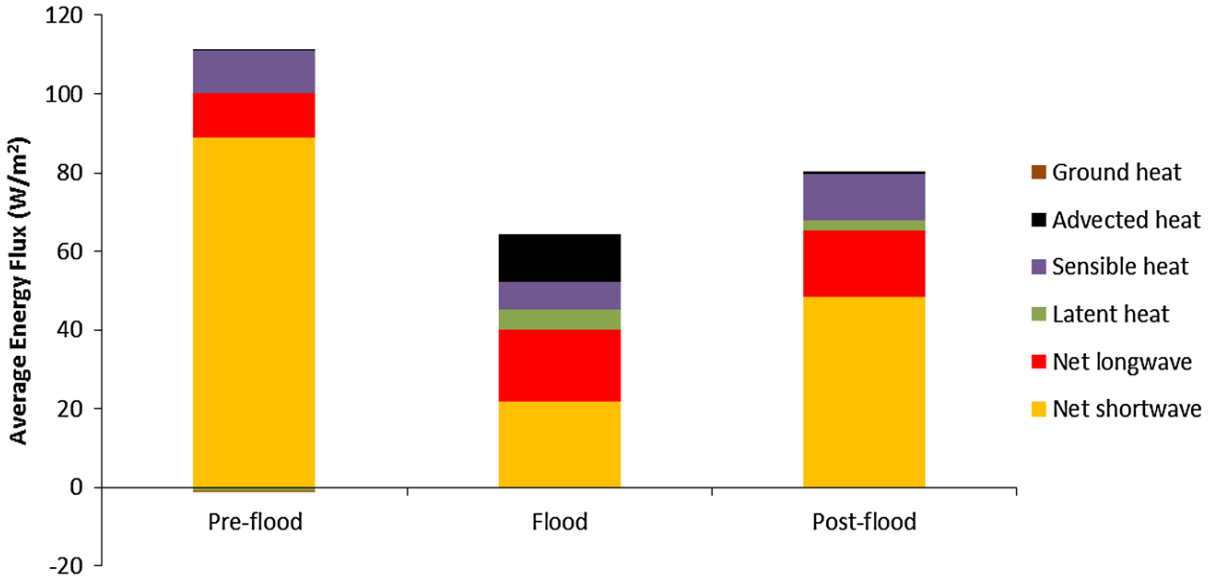

Figure 1.2 Pre-flood, flood, and post-flood estimated energy fluxes to the Fisera south-face snowpack, Marmot Creek Research Basin (*Pomeroy et al.*, 2016).

In addition to being a significant source of energy for snow and accelerating melt, ROS adds a large amount of liquid water to the snowpack that, if infiltrating a cold and dry snowpack, can be stored either by freezing or by capillary suction (*Wever et al.*, 2015). The amount of liquid water that is stored depends on snowpack depth, porosity, permeability internal structural features such

as ice layers or preferential flow paths, and thermodynamic state (*Singh et al.*, 1997). The release of latent heat upon freezing of rainwater is a massive source of energy for the snowpack, whose temperature significantly increases. Once the snowpack becomes isothermal at 0ºC and wet, any additional rainfall input will result in melt and runoff. This runoff then exceeds the rainfall rate due to the additional snowmelt. Runoff from shallow snowpacks reacts more quickly to rain, whereas deep snowpacks store more rainwater and delay runoff (*Wever et al.*, 2014a).

As water from rainfall can be a significant source of water for discharge (*Mazurkiewicz et al.*, 2008), snow models must simulate flux of liquid water, water retention within the snowpack, and heat exchanges between liquid water and ice in order to accurately estimate snowpack runoff.

1.2.3 Water Infiltration, Ice Layer and Preferential Flow Path Formations in Snow

Liquid water flow through snow has been actively investigated for more than four decades. This process drives the timing and spatial distribution of snowmelt runoff from deep snowpacks due to the water holding capacity and lag effects of snow (*Male and Gray*, 1975). In this section, theories of water movement within a snowpack, effects of snowpack properties on flow, and limitations of current theories and models are developed.

Colbeck (1972) developed the first macroscopic hydraulic theory of water percolation in isothermal, homogeneous snow. This model was initially implemented in snow models such as CROCUS (*Brun et al.*, 1989, 1992). This theory considers only vertical gravity drainage. The liquid water flow velocity is estimated from Darcy's Law. Refreezing and ponding of liquid water are not considered. To apply this simplified model of water flow through snow, permeability of the water phase must be known. This parameter is a function of snow internal properties – porosity, grain size, and density – and the water content present within the pores. Based on experimental data on water percolation through snow, *Colbeck and Davidson* (1973) estimated a better relationship for permeability of water in snow as a function of effective water saturation.

Irreducible water content is an important parameter for the simulation of liquid water flow; little is known about the dependency of this parameter on snow properties. From laboratory experiments on a homogeneous snowpack, *Colbeck* (1974) suggested a value higher than 3 % for this parameter, while *Katsushima et al.* (2013) and *Yamaguchi et al.* (2010) found values ranging from 18 % to 4 %. In the snow model CROCUS, this parameter is set up to 5 % of the total pore volume

(*Vionnet et al.*, 2012). As snow internal properties are constantly evolving, the irreducible water content changes, and assuming a constant value for the whole snowpack is physically and conceptually inaccurate. A relationship between this parameter and snow properties has yet to be found.

To estimate permeability of the water phase, snow intrinsic permeability (i.e. saturated hydraulic conductivity) must be known. *Albert and Shultz* (2002) showed that intrinsic permeability of snow is poorly related to snow density, suggesting that other parameters, such as snow grain size, should be considered. *Shimizu* (1970) suggested an empirical equation relating the saturated hydraulic conductivity to grain size and density, based on laboratory experiments with both air and kerosene permeameters for fine-grained compacted snow. More recently, *Calonne et al.* (2012) developed a new equation based on three-dimensional processed images of different snow samples, which is now more generally used in snow models instead of Shimizu's equation (*Shimizu*, 1970). The latter formulation of intrinsic permeability resulted in better routing simulations in the SNOWPACK model (*Wever et al.*, 2015).

Applying conservation of mass for two-phase flow (air and water) in a snowpack, assuming that gravitational flow dominates and using the method of characteristics, *Colbeck and Davidson* (1973) developed a simplified equation for the wetting front propagation for a constant water flux value. An analytical solution of the same problem was developed by *Albert and Krajeski* (1998) from the mass conservation equation developed by *Colbeck* (1972). This new solution was implemented in a numerical model, SNAP, which showed good prediction of the magnitude and timing of snowmelt for a small computational cost; however, this theory has not been applied in other snow models.

The first theories by *Colbeck* (1972) and *Colbeck and Davidson* (1973) to simulate flow propagation through isothermal, homogeneous snow have been improved to account for layers within the snow, considering the snowpack as an anisotropic media (*Colbeck*, 1975); impermeable layers (*Colbeck,* 1974a); and capillary effects at the leading edge of melt wave (*Colbeck*, 1974b). To model capillary forces at the melt wave front, (*Colbeck*, 1974b), an empirical relationship between capillary pressure and effective water saturation from artificial snow in a laboratory was

developed. However, this relationship proved to be unsuitable for natural snowpacks (*Colbeck,* 1976).

By assuming gravitational water flow in Colbeck's model (*Colbeck,* 1972), water pressure gradients were neglected. *Wankiewicz* (1979) measured water pressure at different locations inside a snowpack using tensiometers and showed that water pressure gradients should not be ignored in certain zones within the snowpack, especially at texture interfaces in ripe snowpacks. He also hypothesized that water pressure gradients might be significant in other places within the snowpack and stated that further research is required. From these results, *Wankiewicz* (1979) developed a conceptual model, FINA (Flow Impeding, Neutral or Accelerating), to account for flow acceleration and ponding of water over impermeable layers or at the interface of two layers of different grain sizes, depending on the gravity-flow pressures of each layer.The influence of capillary forces on water flow has been represented by implementing the Richards equation in snow models (*Jordan*, 1995; *Hirashima et al.*, 2010; *Wever et al.*, 2014b, 2015). This provided better results when estimating snowmelt runoff (*Wever et al.*, 2014b).

Colbeck's theory (*Colbeck*, 1972) assumed that the flow of water is laminar and therefore can be estimated from Darcy's Law. However, *Wankiewicz* (1979) stated that the possible occurrence of non-Darcian flow within a snowpack should not be ignored. Assuming that non-Darcian flow occurs for Reynolds numbers above a value of 1, for both saturated and unsaturated conditions, and that gravity flow applies, *Wankiewicz* (1979) found a critical value for the ground slope angle above which turbulent flow within snow might occur. He also observed that non-Darcian flows are likely to occur in steep coarse-grain saturated snow, such as saturated flow layers over impermeable layers in sloping snowpacks.

Although theories based on physical principles have been developed to estimate water flux within a snowpack, these theories were established only under specific assumptions. By ignoring snowpack internal features, such as flow fingers or ice layers, the temporal and spatial variabilities of snowpack meltwater flow are underestimated (e.g. *Jordan*, 1983; *Marsh and Woo*, 1985). These features have been observed to significantly affect propagation of the wetting front (*Marsh and Woo*, 1984a). *Marsh and Woo* (1984a) showed that it is improper to consider a uniform vertical wetting front advance within the snowpack because liquid water can pond over a low permeability

layer. This ponded liquid water may also refreeze and become an ice layer, releasing latent heat energy that warms up the surrounding cold snow. In addition to the ice layers, macropores or flow fingers greatly impact the wetting front movement (*Marsh and Woo*, 1984a; *Kattelmann*, 1985). *Colbeck* (1979) hypothesized that flow fingers develop when liquid water percolates into a dry, cold snowpack and they will remain zones of higher flow as the snowpack wets up, due to fast wet snow metamorphism. However, *Schneebeli* (1995) observed that the location of PFP in snow changed after each melt-freeze cycle. These flow fingers can form macropore networks or be isolated macropores above and below snow layers of different grain sizes in a snowpack (*Kattelmann*, 1985).

Ice layers tend to delay vertical percolation of water inside a snowpack, but they may accelerate snowmelt runoff due to overlying saturated flow (*Furbish*, 1988). These features have significant repercussions on the spatial variation of snowmelt discharge from the base of a snowpack (*Marsh and Woo*, 1985). Colbeck (1974b) modelled the high saturation layer that can form above an ice layer. He derived an equation to estimate the change of the saturated layer thickness and the lateral flow velocity using Darcy's Law. Ice layers are likely to degenerate due to latent heat flux released when liquid water freezes (for instance, during heavy rain), but this process is not well understood (*Colbeck*, 1991). In order to model water percolation or ponding over ice layers, their intrinsic permeability should be determined (*Hardy and Albert*, 1993). The water flow around an ice layer is a two-dimensional process requiring the use of a fully two- or three-dimensional model for accurate simulation (*Pfeffer et al.*, 1990). The model developed by *Pfeffer et al.* (1990) divides the snow into three different zones: a wet zone above the wetting front, a dynamic zone at the wetting front, and a dry zone below the wetting front. This model is analogous to the famous Green-Ampt model for infiltration into soil (*Green and Ampt*, 1911). The dynamic zone is characterized by the occurrence of both water flow and heat transfer. Liquid water is allowed to freeze within this zone, as the snow is in thermodynamic disequilibrium between the liquid and solid phases. *Pfeffer et al.* (1990) suggested incorporating the concept of a dynamic zone in an operational snow model to improve the prediction of wetting front advance.

As with ice layers, flow fingers are rarely included in a snow model. *Marsh and Woo* (1984b) developed an empirical snow model accounting for the effects of flow fingers on the wetting front advance. In this model, the spatial distribution and width of the flow fingers, as well as water flow

in them, were determined from field observations (*Marsh and Woo*, 1984a). However, at that time, the cause for the formation of preferential flow paths was still unknown (*Marsh*, 1991). Prior to their formation, saturated horizontal layers over impermeable ice layers or at the boundary of two stratigraphic snow layers of different grain sizes have been observed (*Marsh and Woo*, 1984a). In laboratory experiments during which dyed water was spread upon artificial snow samples, *Katsushima et al.* (2013) observed the formation of preferential flow paths. They also measured capillary overshoot at the boundary between wet to dry snow. *Hirashima et al.* (2014) developed a 3D numerical model to represent the observations of *Katsushima et al.* (2013). This model uses the Richards equation to estimate the flow of water through snow; it was found that combining a water entry pressure for dry snow with heterogeneities in grain size and density allowed the model to represent preferential flow. The flow velocity within these macropores is potentially turbulent; in this case, applying Darcy's Law to estimate flow velocity would be inadequate (*Marsh*, 1991; *Waldner et al.*, 2004).

Liquid water can be retained at the interfaces of fine to coarse snow layers due to high capillary pressure (*Jordan*, 1995; *Pfeffer and Humphrey*, 1996; *Waldner et al.*, 2004). Indeed, the suction is higher in fine-grained than in coarse-grained layers. The occurrence of lateral flows at the interface of fine over coarse snow layers in sloping snowpacks has been well documented (*Wankiewicz*, 1979; *Kattelmann and Dozier*, 1999; *Eiriksson et al.*, 2013). This process greatly impacts the redistribution of liquid water within snowpacks on hillslopes and the hydrological response to snowmelt and ROS events at catchment scales. The water retention curve, i.e. the relationship between capillary pressure and liquid water saturation must be known to reproduce capillary pressure barriers (*Katsushima et al.*, 2009). Laboratory studies have been conducted to develop a water retention curve for snow, depending on the snow grain size (e.g. *Yamaguchi et al.*, 2010, 2012). However, no known water retention curve is applicable to ice layers or preferential flow paths. The water retention curve developed by *Yamaguchi et al.* (2010), which depends only on snow grain size was implemented in SNOWPACK, with the Richards equation to improve the simulation of water flow (*Wever et al.*, 2014b). Although this study could simulate capillary barrier effects on flow, it did not consider preferential flow paths, snow density distribution and lateral flows, as the model is only one-dimensional. The model SNOWPACK has recently been updated to incorporate preferential flow (*Wever et al.*, 2016*; Würzer et al.*, 2017). A dual-porosity approach was applied, which assumed that the porous medium is divided into two domains: matrix flow and

preferential flow. The mass flow equation was computed in each domain, and a transfer function was applied to transfer mass from one domain to the other. The area of preferential flow domain was determined from an empirical function, which was developed from the laboratory data of *Katsushima et al.* (2013). This approach gave better results when estimating snowpack runoff over entire winter seasons. However, two calibration coefficients were necessary to use this approach, and further study is required to better determine these parameters.

1.2.4 Preferential Flow in Soil

Preferential flow in soil has been studied for decades. Preferential flow paths and macropores impact the rate of water infiltration into soils and storm-runoff generation (e.g. *Beven and Germann*, 1982; *McDonnell*, 1990). Early on, *Hill* (1952) reported the observation of gravity-driven unstable flow in soil. The study of gravity-driven unstable flow has since become a subject of great interest for many researchers. *Hill and Parlange* (1972) observed that flow fingers initiated when a wetting front becomes unstable after ponding of water at soil-textured interfaces. A necessary condition for unstable wetting front to occur is that the input flux must be less than the saturated hydraulic conductivity (*Hill and Parlange*, 1972; *Raats*, 1973). This is known as the Saffman-Taylor condition.

A preferential flow path can be separated into two sections: the "tip" at the leading edge and the "tail" upstream of the leading edge. In laboratory experiments, saturation overshoot in a preferential flow path was observed (e.g. *Glass et al.*, 1989; *Glass and Nicholl*, 1996; *DiCarlo*, 2004), i.e. the saturation at the tip of the preferential flow paths is higher than saturation within the tail. Along with saturation overshoot, capillary overshoot within preferential flow paths was also measured with tensiometers (*Selker et al.*, 1992). Standard soil infiltration models solving for Richards equation cannot capture saturation overshoot at the tip of flow fingers (*Egorov et al.,* 2003). Thus, extensions to the Richards equation have been theorized to represent this phenomenon (e.g. *Elliassi and Glass*, 2001; *Hassanizadeh and Gray,* 1993); *Hassanizadeh and Gray* (1993) suggested adding a dynamic term in the capillary pressure. Through a thermodynamic study at pore scale, *Hassanizadeh and Gray* (1993) demonstrated that this dynamic pressure term depended on the rate of water saturation and that the common equation relating capillary pressure to water saturation is only valid under equilibrium conditions. An overview of laboratory

experiments of dynamic effects in the capillary pressure-saturation curves can be found in *Hassanizadeh et al.* (2002).

Various numerical models were developed to test the theory of dynamic capillary pressure proposed by *Hassanizadeh and Gray* (1993). In 1D, these models were able to simulate capillary pressure or saturation overshoots at the tip of the wetting fronts (e.g. *DiCarlo,* 2005; *Sanders et al.,* 2008). In 2D or 3D, these non-equilibrium models could simulate the formation and propagation of preferential flow paths (e.g. *Nieber et al.,* 2003; *Sanders et al.,* 2008; *Chapwanya and Stockie,* 2010; *Zhang and Zegeling,* 2017). The dynamic pressure effects on flow varied with grain size, water influx, and initial water content within the soil (*Camps-Roach et al.,* 2010; *DiCarlo*, 2006). The cause of these dynamic effects on pressure is still under investigation, but some explanations have been suggested, such as a dynamic contact angle at the solid-liquid-gas interface, temporal changes in wettability and heterogeneities at microscale (*Diamantopoulos and Durner*, 2012).

Despite the vast knowledge on modelling preferential flow in soil, most snow models ignore this process, resulting in inaccuracy in estimating snowmelt runoff. The research model by *Hirashima et al.* (2014, 2017) can simulate formation of preferential flow paths in snow, but it applies a single-valued water entry pressure to estimate water pressure within air-dry snow pores. The use of a single-valued capillary entry pressure in soil models was shown to not accurately represent the transient nature of capillary pressure during wetting (*DiCarlo*, 2010). Therefore, additional work is required to improve representation of preferential flow paths in snow using current knowledge from soil physics.

1.2.5 Sloping Snowpacks

Liquid water flow within sloping snowpacks and its contribution to snowmelt hydrographs has been too long ignored (*Kattelmann*, 1987), despite the common occurrence of lateral flow in a sloping snowpack during ROS events (*Eiriksson et al.*, 2013). As basal ice layers can form at the interface between soil and snow (e.g. *Marsh and Woo*, 1984a), liquid water can be transported laterally before infiltrating the soil. The stratigraphic structure of snow can also divert vertical flows due to capillary barriers or inclined snow layers of low permeability. Lateral water flow is

not considered or is poorly handled in operational snow models. These snow models lack accuracy when estimating snowmelt runoff from sloping snowpacks in mountainous terrain.

1.2.6 Snow Energy Balance

Physically based snow models are widely applied without questioning the physics of how energy is exchanged between a snowpack and its surrounding environment. For instance, *Lehning et al.* (2002) simulate turbulent fluxes over an alpine snowpack using the flux gradient method, assuming neutral atmospheric conditions. This first-order closure approach is unsuitable in mountainous environments due to the non-homogeneous nature of the terrain and the existence of large eddies that bring additional sensible heat energy to the snowpack (*Helgason and Pomeroy*, 2012a).

Helgason and Pomeroy (2012b) studied closure of the energy balance over a homogeneous snowpack during midwinter in the Canadian Prairies. Although this study was conducted in ideal conditions, i.e. all fluxes at the upper and lower boundaries of a snowpack were measured, as well as the snow internal and surface temperatures, the energy balance could not be closed. This was caused by large longwave radiation loss at the surface of the snowpack, which was not balanced by other observed fluxes. This research suggested that sensible heat flux over the snowpack was under-measured by the eddy covariance system during stable and low wind speed conditions. This imbalance in the energy budget over snow is also found in snowmelt models, particularly under stable atmospheric conditions, during which the theories underestimate turbulent fluxes. Thus, a corrective numerical strategy adding a 'windless coefficient' is commonly used in numerical models to increase turbulent fluxes (*Brun et al.*, 1989; *Jordan et al.*, 1999; *Brown et al.*, 2006). This coefficient is usually calibrated to match simulated snow surface temperature to observations. Further work is required to better understand the origin of this energy imbalance and how models can be improved to better predict changes in snowpack internal energy.

1.2.7 Snow Models and Their Limitations

Despite years of research on snowmelt energetics and meltwater flow, current models do not include the full suite of known flow complexity, have fundamental problems with atmospheric exchanges, and have not been evaluated for application on hillslopes, where most mountain runoff occurs.

Numerical snow models have been developed with different complexities for distinct purposes. The earliest models were based on empirical considerations and neglected many physical processes. The well-known degree-day method was applied to estimate snow ablation and melt in early studies before a full understanding of the snowmelt process was achieved (e.g. *US Army Corps of Engineers*, 1987; *Martinec et al.*, 2008). In the 1970s, the energy balance approach was incorporated into models and the finite-different method utilized (*Brun et al.*, 2010). Models have been developed for hydrological purposes, snow avalanche prediction, to assess climate change impacts, and at different spatial scales of application, from point to catchment scale. Recently, one-dimensional snow models were incorporated into large-scale models, such as general circulation models or land surface models, for applications at larger scales and to improve estimations of surface temperature and surface albedo used as lower boundary conditions for the GCMs (e.g. *Vionnet et al.*, 2012).

In the 1990's, research at NOAA focused on representing the spatial distribution of snowpacks at basin scale by coupling remote sensing of snow and snowmelt modelling. *Cline et al.* (1998) developed a simple one-layer distributed snowmelt model that includes snow surface energy balance and coupled this model to remotely sensed snowcover duration to back-calculate the distribution of SWE at peak accumulation and the spatial distribution of snowmelt through the melt season. This model gave reasonable estimates of SWE distribution at basin scale when compared to field surveys. Coupling snow remote sensing and snow modelling is still currently used to estimate SWE distribution in mountain basins (e.g. *Painter et al., 2016*). In studies where snow remote sensing is coupled with snowmelt modelling, relatively simple snowmelt models are used to reduce computational overhead. These models do not represent snow internal processes, such as water flow through snow, or the influence of snow layers on water retention and flow. The employment of simple snow models was justified by *Cline and Caroll* (1999) who demonstrated that using a simple, spatially distributed snowmelt model that includes snow surface energy balance can still provide useful hydrological forecasting information in an operational environment if data assimilation from remote sensing is used to overcome model deficiencies. These results emphasized on the importance of accurately simulating SWE distribution and depletion on timing and magnitude of snowmelt. The conclusion of *Cline and Caroll* (1999) that a simple snow model that neglects snow internal processes is sufficient to provide good hydrological forecasting with data assimilation from observations could be a result of the isothermal nature of the Californian

snowpack and the high density of surface observation stations in the region where this study and the study of *Painter et al.* (2016) were conducted. *DeBeer and Pomeroy* (2017) also showed the importance of accounting for snowcover depletion when estimating snowmelt runoff in a mountain basin in the Canadian Rockies. However, *DeBeer and Pomeroy* (2017) concluded that snow ablation processes need to be better represented in hydrological models as they affect snow cover accumulation and depletion, particularly during freeze-thaw processes occurring during the accumulation period. This study was conducted where deep and complex layered snowpacks are found, with snowpack temperature below freezing when the first snowmelt event occurs. Therefore, improving the representation of snow internal processes in snow models is of primary importance in regions of cold, deep, and layered snowpacks, such as the Canadian Rockies. It is also important where data assimilation opportunities are limited by sparse mountain observation networks, such as most of the Western Cordillera in Canada.

To predict the formation of ice layers or PFP, multi-dimensional snow models that simulate lateral water flow, heat transfer, and snow metamorphism should be applied (*Pfeffer et al.*, 1990; *Marsh*, 1991). However, all physically based models that can predict snow internal features, such as SNOWPACK (*Bartelt and Lehning*, 2002; *Bartelt et al.*, 2002; *Lehning et al.*, 2002; *Wever et al.*, 2015, *Würzer et al.*, 2017), CROCUS (*Brun et al.*, 1989, 1992; *Vionnet et al.*, 2012, *D'amboise et al.*, 2017), or SNTHERM (*Jordan*, 1991) are only one-dimensional. Although these models estimate snow internal changes, few validations have been made against field data (*Gustafsson et al.*, 2004). Simpler snowmelt models, such as Snobal (*Marks and Dozier*, 1992) and EBSM (Gray and Landin, 1988), which neglect some snowpack physics processes in favour of model stability and fewer parameters, have been developed for hydrological purposes.

Table 1.1 summarizes the characteristics of different operational snow models and the main physical processes they simulate. All of them apply the energy balance approach to estimate the thermodynamic state of the snowpack and snow ablation, but most of them miss fundamental processes in the simulation of liquid water flow. In the most sophisticated snow models, the Richards equation was implemented only recently to improve simulations of liquid water flow (*Wever et al.*, 2014b, 2015; *D'Amboise et al.*, 2017). In SNOWPACK, preferential flow was included using a dual-domain approach. This approach improved snowpack outflow estimations over entire winter seasons (*Würzer et al.*, 2017); this approach, however, lacks physical

representation of flow processes during the formation of preferential flow paths, and it therefore requires calibration coefficients. This causes the model to over-estimate water ponding at capillary barriers and to delay the arrival of water at the bottom of the snow samples (*Hirashima et al.*, 2017). Implementing a conceptual representation of preferential flow in snow allowed simulation of some ice layers observed in the snowpack (*Wever et al.*, 2016). Of the models presented in Table 1.1, Snobal is the only one used for hydrological prediction. To improve simulation of water flow in Snobal, the model should include more snow layers while keeping its numerical efficiency. In addition, Snobal poorly estimates ground heat flux and the melt/refreeze processes inside the snowpack (*Adam Winstral*, USDA, personal communication).

Other snow models have been developed for research purposes and focused on only a few snow processes (e.g. *Illangasekare et al.*, 1990; *Tseng et al.*, 1994). *Daanen and Nieber* (2009) developed a two-dimensional model coupling liquid water flow and heat transfer within a snowpack. They found better results in estimating the front water penetration than other models using Stefan formulation, which uses a moving boundary condition for the heat transfer equation (*Tseng et al.*, 1994). Unfortunately, this model has not been validated against in-situ data.

1.3 Research Design

1.3.1 Purpose of the Research

Water flow through a snowpack has been investigated for many decades. Understanding this process will improve prediction of the magnitude and timing of snowmelt runoff from deep snowpacks. Although many theories are now available to estimate the position of the wetting front within a snowpack and to couple heat and mass energy fluxes, most of them are only suitable for homogeneous, flat snowpacks and neglect ice layers and PFP formations. These restrictive assumptions have considerable effects on the estimation of snowmelt runoff in natural environments.

Table 1.1 List of some snow models and their characteristics

Characteristics/ Physical processes	Snobal	SNTHERM	CROCUS	SNOWPACK
Application	Prediction of the melting and runoff from snowpacks.	"Understanding snow processes and forecasting runoff" (*Yang*, 2008)	"Understanding snow processes, operational avalanche forecasting in France" (*Yang*, 2008)	"Understanding snow processes, forecasting runoff and avalanche warning" (*Yang,* 2008)
Maximum number of layers	2	Depends on the number of snowfalls	Depends on the number of snowfalls	Depends on the number of snowfalls
Snow settlement	Yes	Yes	Yes	Yes
Melting and refreezing	Yes	Yes	Yes	Yes
Snow metamorphism	No	From temperature gradient and water content	From temperature gradient, water content, and wind drift	From temperature gradient and water content
Snow surface temperature	At a fixed surface layer	At a surface layer	At a surface layer	At a surface layer
Wind pumping	Not included	Not included	Not included	Included in the turbulent fluxes
Turbulent fluxes	Bulk transfer method. Stability as a function of the Monin-Obukhov length.	Bulk transfer method. Stability as a function of Richardson number.	Bulk transfer method. Stability as a function of Richardson number.	Bulk transfer method. Neutral conditions only.
Shortwave penetration	No	Extinguishes exponentially	Extinguishes exponentially	Extinguishes exponentially
Water flow	Bucket scheme model	Gravitational flow	Gravitational flow	Richards equation
Water retention	Yes	Yes	Yes	Yes
Capillary barrier	**No**	**No**	**No**	Yes
Preferential flow paths	**No**	**No**	**No**	Yes (dual-domain approach)
Lateral flow	**No**	**No**	**No**	**No**

Acknowledging the limitations of current theories, this research will focus on improving understanding and prediction of liquid water flow through layered snowpacks, on both flat and sloping grounds.

1.3.2 Research Objectives and Questions

This research will be divided into three objectives, which will answer several research questions:

1) What factors control the formation and development of preferential flow paths and ice layers in snow?

- How can water flow in various pathways within a snowpack be best described by thermodynamics and physical flow laws?
- Can a snow model be developed to incorporate the physical processes of preferential flow paths and ice layer formations?

2) To what degree do pressure relationships control water retention and flow in snow?

- How can the current water retention curves in snow be improved to include flow wetting process?
- What is the impact of capillary hysteresis on flow through snow and preferential flow paths?

3) Can convective heat flux within a snowpack enhance the snow energetics estimate?

- Where does convective heat flux originate in snow?
- Can simulation of heat convection improve model performance to predict snow surface temperature?

1.3.4 Research Significance

The main objective of this research is to improve understanding and prediction of snowmelt in deep mountainous snowpacks in cold regions. By improving understanding of internal snow mass and energy flux processes to underpin development of a model that can predict snowmelt runoff from a sloping snowpack, the ability to calculate the timing and magnitude of snowmelt contributing to streams in mountain catchments can be greatly improved. The small-scale snow

model will be a base from which a future hydrological model suitable at catchment scales may be developed.

1.4 Thesis Outline

Chapter 2 details the development of a novel 2D model that simulates the formation of PFP. Coupling of mass and energy flows and surface melt are accounted for. This model simulates the formation of preferential flow paths by combining water entry pressure with heterogeneities in snow density and grain size. Different applications of this model are presented for different snowpacks and slope angles.

In Chapter 3, the model presented in Chapter 2 is improved to better simulate mass flow through snow. Hysteresis in capillary pressure is incorporated and the model is validated against published data. By combining mass and heat fluxes, the formation of ice layers is demonstrated.

Chapter 4 presents melt and outflow data collected during a field campaign conducted in the winter of 2014-2015. The model presented in Chapter 4 is evaluated against the field data and the limitations of this model are highlighted. In this chapter, additional data obtained during dye experiments are presented and analysed to inform selection of the shape and fractal properties of preferential flow paths.

Chapter 5 introduces a new capillary pressure estimation for initially dry snow and an extended Richards equation model to simulate capillary overshoot, which has been shown to be the cause of PFP in soil. This model gave better results than the first model (Chapters 2 and 3) in simulating capillary pressure overshoot.

Chapter 6 investigates the impact of heat convection within a snowpack on the simulation of snow surface temperature. The convection was driven by airflow originating from pressure fluctuations at the snow surface.

Conclusions to the research are presented in Chapter 7, as well as the next steps that should be considered to apply and improve this research.

1.5 Candidate Contributions to Manuscripts

It is acknowledged that I am first author on all manuscripts in this thesis with my supervisor Dr. J. Pomeroy as second author. My contribution to each manuscript included model development, application of the model, analysis of the model results, conceptualization of field work experiments and analysis, and lead authoring the texts. John Pomeroy assisted with conceptualization of the research, provided useful feedback on the content .

1.6 References

Albert, M., and G. Krajeski (1998), A fast, physically based point snowmelt model for use in distributed applications, *Hydrol. Process.*, *12*, 1809–1824.

Albert, M. R., and E. F. Shultz (2002), Snow and firn properties and air – snow transport processes at Summit, Greenland, *Atmos. Environ.*, *36*, 2789–2797.

Bartelt, P., and M. Lehning (2002), A physical SNOWPACK model for the Swiss avalanche warning: Part I: numerical model, *Cold Reg. Sci. Technol.*, *35*, 123–145.

Bartelt, P., M. Lehning, and B. Brown (2002), A physical SNOWPACK model for the Swiss avalanche warning: Part II. Snow microstructure, *Cold Reg. Sci. Technol.*, *35*, 147–167.

Beven, K., and Germann, P. (1982). Macropores and water flow in soils. *Water Resources Research*, *18*(5), 1311–1325.

Brun, E. (1989), Investigation on wet-snow metamorphism in respect of liquid-water content, *Annals of Glaciology*, 13.

Brun, E., David, P., Sudul, M., and G. Brunot (1992), A numerical model to simulate snow-cover stratigraphy for operational avalanche forecasting, *Journal of Glaciology*, 38(128).

Brun, E., Martin, E., Simon, V., Gendre, C., and C. Coleou (1989), An Energy and Mass Model of Snow Cover Suitable for Operational Avalanche Forecasting, *J. Glaciol.*, 35, 333–342, https://doi.org/11017/S0022143000009254.

Brun, E., Z.-L. Yang, R. Essery, and J. Cohen (2010). Snow-cover parameterization and modeling in *Snow and Climate*, Edited by R. L. Armstrong and E. Martin, Cambridge University Press, 2010, 125-129.

Camps-Roach, G., D. M. O'Carroll, T. A. Newson, T. Sakaki, and T. H. Illangasekare (2010), Experimental investigation of dynamic effects in capillary pressure: Grain size dependency and upscaling, *Water Resour. Res.*, 46, W08544, doi:11029/2009WR008881.

Chapwanya, M., and J. M. Stockie (2010), Numerical simulations of gravity-driven fingering in unsaturated porous media using a nonequilibrium model, *Water Resour. Res*., 46, W09534, doi:11029/2009WR008583

Cline, D. W., R. C. Bales, and J. Dozier (1998), Estimating the spatial distribution of snow in mountain basins using remote sensing and energy balance modeling, *Water Resour. Res.*, 34(5), 1275–1285, doi: 10.1029/97WR03755

Cline, D., and T. Carrol (1999), Inference of snow cover beneath obscuring clouds using optical remote sensing and a distributed snow energy and mass balance model, *Journal of Geophysical Research*, 1041, 19631-19644, doi:10.1029/1999JD900249.

Colbeck, S. C. (1972), A theory of water percolation in snow, *Journal of Glaciology*, 11(63), 369-385.

Colbeck, S. C. (1974a), The capillary effects on water percolation in homogeneous snow, *J. Glaciol.*, *13*(67), 85–97.

Colbeck, S. C. (1974b), Water flow through snow overlying an impermeable boundary, *Water Resour. Res.*, *10*(1), 119–123.

Colbeck, S. C. (1975) A theory for water flow through a layered snowpack, *Water Resour. Res.*, *11*(2), 261–266.

Colbeck, S. C. (1976), An analysis of water flow in dry snow, *Water Resour. Res.*, *12*(3), 523–527.

Colbeck, S. C. (1979), Water flow through heterogeneous snow, *Cold Reg. Sci. Technol.*, *1*, 37–45.

Colbeck, S.C (1982), An overview of seasonal snow metamorphism, *Reviews of Geophysics and Space Physics*, 20(1), 45-61.

Colbeck, S. C. (1991), The layered character of snow covers, *Rev. Geophys.*, *29*, 81–96.

Colbeck, S., and G. Davidson, (1973), Water percolation through homogeneous snow, *Int. Symp. Role Snow Ice*, *4*, 242–257.

Conway, H., and C. Raymond (1993), Snow stability during rain, *J. Glaciol.*, *39*(133), 635–642.

Daanen, R. P., and J. L. Nieber (2009), Model for coupled liquid water flow and heat transport with phase change in a snowpack, *J. Cold Reg. Eng.*, *23*(2), 43–68, doi:11061/(ASCE)0887-381X(2009)23:2(43).

D'Amboise, C. J. L., Müller, K., Oxarango, L., Morin, S., and T. V. Schuler (2017), Implementation of a physically based water percolation routine in the Crocus/SURFEX (V7.3) snowpack model, *Geosci. Model Dev*., 10, 3547-3566, doi:15194/gmd-10-3547-2017.

Denoth, A. (1980), The pendular-funicular transition in snow, *J. Glaciol.*, 25(91), 93-97.

Diamantopoulos, E., and W. Durner (2012), Dynamic nonequilibrium of water flow in porous media: a review, *Vadone Zone Journal*, 11, doi:12136/vzj2011.0197.

DiCarlo, D. A. (2004), Experimental measurements of saturation overshoot on infiltration, *Water Resour. Res.*, 40, W04215, doi:11029/2003 WR00267

DiCarlo, D. A. (2005), Modeling observed saturation overshoot with continuum additions to standard unsaturated theory, *Adv. in Water Res.*, 28, 1021-1027, doi:11016/j.advwatres.2004.12.003.

DiCarlo, D. A. (2006), Quantitative network model predictions of saturation behind infiltration fronts and comparison to experiments, *Water Resour. Res.,* 42, WS07408, doi:11029/2005WR00475

Dingman, S. L. (2005), Physical Hydrology. Publisher: Prentice Hall, second edition.

Eiriksson, D., M. Whitson, C. H. Luce, H. P. Marshall, J. Bradford, S. G. Benner, T. Black, H. Hetrick, and J. P. Mcnamara (2013), An evaluation of the hydrologic relevance of lateral flow in snow at hillslope and catchment scales, *Hydrol. Process.*, *27*(January), 640–654, doi:11002/hyp.9666.

Eliassi, M., and R. J. Glass (2001), On the continuum-scale modeling of gravity-driven fingers in unsaturated porous media: The inadequacy of the Richards Equation with standard monotonic constitutive relations and hysteretic equations of state, *Water Resour. Res.*, 37(8), 2019–2035, doi:11029/2000WR900403.

Fang, X., Pomeroy, J. W., Ellis, C. R., MacDonald, M. K., DeBeer, C. M., and T. Brown (2013), Multi-variable evaluation of hydrological model predictions for a headwater basin in the Canadian Rocky Mountains, *Hydrol. Earth Syst. Sci.*, 17, 1635-1659, https://doi.org/10.5194/hess-17-1635-2013.

Fierz, C., Armstrong, R.L., Durand, Y., Etchevers, P., Greene, E., McClung, D.M., Nishimura, K., Satyawali, P.K. and S.A Sokratov (2009). The International Classification for Seasonal Snow on the Ground, *IHP-VII Technical Documents in Hydrology N°83*, IACS Contribution N°1, UNESCO-IHP, Paris.

Furbish, D. (1988), The influence of ice layers on the travel time of meltwater flow through a snowpack, *Arct. Alp. Res.*, *20*(3), 265–272.

Glass, R. J., and M. J. Nicholl (1996), Physics of gravity fingering of immiscible fluids within porous media: An overview of current understanding and selected complicating factors, *Geoderma*, 70, 133–163.

Glass, R. J., Parlange, J.-Y., and T. Steenhuis (1989), Mechanism for finger persistence in homogeneous unsaturated porous media: Theory and verification, Soil Sci., 148(1), 60-7

Green, W.H. and G. Ampt (1911), Studies of soil physics, part I – the flow of air and water through soils. *J. Ag. Sci.*, 4, 1-24.

Gustafsson, D., P. a. Waldner, and M. Stähli (2004), Factors governing the formation and persistence of layers in a subalpine snowpack, *Hydrol. Process.*, *18*, 1165–1183.

Hardy, J., and M. Albert (1993), The permeability of temperate snow. Preliminary links to microstructure, *50th East. Snow Conf., 61th West. Snow Conf.*, 149–156.

Hassanizadeh, S. M., Celia, M. A., and H. K. Dahle (2002), Dynamic effect in the capillary pressure-saturation relationship and its impact on unsaturated flow, *Vadose Zone Journal*, 1,38-57.

Hassanizadeh, S. M., and W. G. Gray (1993), Thermodynamic basis of capillary pressure in porous media, *Water Resour. Res.*, 29(10), 3389–3405, doi:11029/93WR01495.

Helgason, W. and J.W. Pomeroy (2012a), Characteristics of the near-surface boundary layer within a mountain valley during winter. *Journal of Applied Meteorology and Climatology,* 51, 583-597, doi:10.1175/JAMC-D-11-058.1.

Helgason, W. and J.W. Pomeroy (2012b), Problems closing the energy balance over a homogeneous snow cover during midwinter. *Journal of Hydrometeorology*, 13, 557–572, doi: 10.1175/JHM-D-11-0135.1

Hill, S. (1952), Channeling in packed columns, *Chem. Eng. Sci.*, 1, 247-253.

Hill, D.E. and J.-Y. Parlange (1972), Wetting front instability in layered soils, *Soils Science Society of America, Proceedings*, 36(5), 697-702, 1972.

Hirashima, H., Avanzi, F., and S. Yamaguchi (2017), Liquid water infiltration into a layered snowpack: evaluation of a 3-D water transport model with laboratory experiments, *Hydrol. Earth Syst. Sci.,* 21, 5503-5515, https://doi.org/15194/hess-21-5503-2017.

Hirashima, H., Yamaguchi, S., and T. Katsushima (2014), A multi-dimensional water transport model to reproduce preferential flow in the snowpack, *Cold Regions Science and Technology*, 108, 80-90, doi:11016/j.coldregions.2014.09.004.

Horton, R. (1915), The melting of snow, *Mon. Weather Rev.*, 599–605.

Illangasekare, T. H., R. J. Walter, M. F. Meier, and W. T. Pfeffer (1990), Modeling of meltwater infiltration in subfreezing snow, *Water Resour. Res.*, *26*(5), 1001–1012, doi:11029/WR026i005p01001.

Jordan, P. (1983), Meltwater movement in a deep snowpack 2. Simulation model, *Water Resour. Res.*, *19*(4), 979–985.

Jordan, R. (1991), A one-dimensional temperature model for a snow cover: Technical Documentation for SNTHERM.89.

Jordan, R. (1995), Effects of capillary discontinuities on water flow and water retention in layered snowcovers, *Defence Science Journal*, 45(2), 79–91.

Katsushima, T., T. Kumakura, and Y. Takeuchi (2009), A multiple snow layer model including a parameterization of vertical water channel process in snowpack, *Cold Reg. Sci. Technol.*, *59*(2-3), 143–151, doi:11016/j.coldregions.2009.09.002.

Katsushima, T., Yamaguchi, S., Kumakura, T., and A. Sato (2013), Experimental analysis of preferential flow in dry snowpack, *Cold Regions Science and Technology*, 85, 206-216, doi:11016/j.coldregions.2012.09.012, 2013.

Kattelmann, R. (1985), Macropores in snowpacks of Sierra Nevada, *Ann. Glaciol*, 272–273.

Kattelmann, R. (1987), Some measurements of water movement and storage in snow, *Symp. Davos*, (162), 245–254, 1987.

Kattelmann, R., and J. Dozier (1999), Observations of snowpack ripening in the Sierra Nevada, California, USA, *Journal of Glaciology,* 45, 409–416

Lehning, M., P. Bartelt, B. Brown, and C. Fierz (2002), A physical SNOWPACK model for the Swiss avalanche warning: Part III: Meteorological forcing, thin layer formation and evaluation, *Cold Reg. Sci.*, *35*, 169–184.

Male, D. H., and R. J. Granger (1981), Snow surface energy exchange, *Water Resour. Res.*, *17*(3), 609–627, doi:11029/WR017i003p00609.

Male, D.H., and D. M. Gray (1975), Problems in developing a physically based snowmelt model, *Canadian Journal of Civil Engineering*, 2(4), 474–488.

Mankin, J. S., Viviroli, D., Singh, D., Hoekstra, A. Y., and N. S. Diffenbaugh (2015), The potential for snow to supply human water demand in the present and future, *Env. Res. Let.*, 10(11), 114016.

Marks, D., and J. Dozier (1992), Climate and energy exchange at the snow surface in the alpine region of the Sierra Nevada: 2. Snow cover energy balance, *Water Resour. Res.*, *28*(11), 3043–3054.

Marks, D., J. Kimball, D. Tingey, and T. Link (1998), The sensitivity of snowmelt processes to climate conditions and forest cover during rain-on-snow: a case study of the 1996 Pacific Northwest flood, *Hydrol. Process.*, *12*, 1569–1587.

Marsh, P. (1991), Water flux in melting snow covers, Chapter 2 in: M.Y. Corapcioglu (Editor), *Advances in Porous Media*, Vol. 1, Elsevier, Amsterdam, 61–124.

Marsh, P. and Woo, M. (1984a), Wetting front advance and freezing of meltwater within a snow cover: 1. Observations in the Canadian Arctic, *Water Resources Research*, 20(12), 1853–1864, doi:11029/WR020i012p01853.

Marsh, P. and Woo, M. (1984b), Wetting front advance and freezing of meltwater within a snow cover: 2. A simulation model, *Water Resources Research*, 20(12), 1865–1874, doi:11029/WR020i012p01865.

Marsh, P. and Woo, M. (1985), Meltwater movement in natural heterogeneous snow covers, *Water Resources Research*, 21(11), 1710–1716, doi:11029/WR021i011p0171

Martinec, J., A. Rango, and R. Roberts (2008), Snowmelt runoff model (SRM) user's manual, *Agric. Exp. Stn. Spec. Rep. 10*

Mazurkiewicz, A. B., D. G. Callery, and J. J. McDonnell (2008), Assessing the controls of the snow energy balance and water available for runoff in a rain-on-snow environment, *J. Hydrol.*, *354*(1-4), 1–14, doi:11016/j.jhydrol.2007.12.027.

McDonnell, J. (1990). A rationale for old water discharge through macropores in a steep, humid catchment. *Water Resources Research*, 26(11), 2821–2832.

Nieber, J., Sheshukov, A. Egorov, and R. Dautov (2003), Non-equilibrium model for gravity-driven fingering in water repellent soils: formulation and 2D simulations, in *Soil Water Repellency: Occurrence, Consequences and Amelioration*, edited by C. J. Ritsema and L. W. Dekker, 245–257, Elsevier Sci., New York.

Painter, T., Berisford, D., Boardman, J., Bormann, K., Deems, J., Gehrke, F., Hedrick, A., Joyce, M. Laidlaw, R., Marks, D., Mattmann, C. Mcgurk, B., Ramirez, P., Richardson, M., Skiles, M., Seidel, F., and A. Winstral (2016), The Airborne Snow Observatory: Fusion of scanning lidar, imaging spectrometer, and physically-based modeling for mapping snow water equivalent and snow albedo, *Remote Sensing of Environment*, 184. 10.1016/j.rse.2016.06.018.

Pfeffer, W., and N. Humphrey (1996), Determination of timing and location of water movement and ice-layer formation by temperature measurements in sub-freezing snow*, Journal of Glaciology*, 42(141), 1996.

Pfeffer, W., T. Illangasekare, and M. Meier (1990), Analysis and modeling of melt-water refreezing in dry snow, *J. Glaciol.*, *36*(123), 238–246.

Pomeroy, J. W., and E. Brun (2001), Physical properties of snow, in *Snow Ecology: An Interdisciplinary Examination of Snow-Covered Ecosystems*, 45–126.

Pomeroy J.W., Fang X. and D. Marks (2016), The cold rain-on-snow event of June 2013 in the Canadian Rockies - characteristics and diagnosis, *Hydrological Processes*, doi: 11002/hyp.10905, 2016.

Pomeroy, J.W., D. Gray, T. Brown, N. Hedstrom, W. L. Quinton, R. J. Granger, and S. K. Carey (2007), The cold regions hydrological model: a platform for basing process representation and model structure on physical evidence, *Hydrol. Processes*, 2667, 2650–2667, doi:11002/hyp.

Quinton, W.L. and J.W Pomeroy J.W. (2006), Transformations of runoff chemistry in the Arctic tundra, Northwest Territories, Canada, *Hydrological Processes*: 20, 2901-2919.

Raats, P.A. (1973), Unstable wetting fronts in uniform and nonuniform soils. *Soil Science Society of America Journal*, 37(5): 681-685.

Sanders, G. C., O. J. Glidewell and J. Norbury (2008), Dynamic capillary pressure, hysteresis and gravity-driven fingering in porous media, *Journal of Physics: Conference Series*, 138, 12023, doi:11088/1742-6596/138/1/012023.

Schneebeli, M. (1995), Development and stability of preferential flow paths in a layered snowpack, *Biogeochemistry of Seasonally Snow-Covered Catchments* (Proceedings of a Boulder Symposium July 1995). IAHS Publ. no. 228.

Selker, J., Parlange, J.-Y., and T. Steenhuis (1992), Fingered flow in two dimensions: 2. Predicting finger moisture profile, *Water Resour. Res.,* 28, 2523-2528.

Shook, K., and J. Pomeroy (2012), Changes in the hydrological character of rainfall on the Canadian prairies, *Hydrol. Process.*, *26*, 1752–1766, doi:11002/hyp.9383.

Singh, P., G. Spitzbart, H. Hubl, and H. Weinmeister (1997), Hydrological response of snowpack under rain-on-snow events: a field study, *J. Hydrol.*, *202*, 1–20, 1997.

Sui, J., and G. Koehler (2001), Rain-on-snow induced flood events in southern Germany, *J. Hydrol.*, *252*, 205–220, doi:11016/S0022-1694(01)00460-7.

Tseng P., Illangesakare, T., and M. Meier (1994), Modeling of snow melting and uniform wetting front migration in a layered subfreezing snowpack, *Water Resources Research*, 30(8), 2363–2376, doi:11029/94WR00764.

U.S. Army Corp Of Engineers (1987). SSARR User's Manual (Army Corps of Engineers, North Pacific Division, Portland, Oregon).

Vincent, L. A., and E. Mekis (2006), Changes in Daily and Extreme Temperature and Precipitation Indices for Canada over the Twentieth Century, *Atmosphere-Ocean*, *44*, 177–193, doi:13137/ao.440205.

Vionnet, V., E. Brun, S. Morin, A. Boone, S. Faroux, P. Le Moigne, E. Martin, and J.-M. Willemet (2012), The detailed snowpack scheme Crocus and its implementation in SURFEX v7.2, *Geosci. Model Dev.*, *5*(3), 773–791, doi:15194/gmd-5-773-2012.

Viviroli, D., H. H. Dürr, B. Messerli, M. Meybeck, and R. Weingartner (2007), Mountains of the world, water towers for humanity: Typology, mapping, and global significance, *Water Resour. Res.*, *43*(7), 1–13, doi:11029/2006WR005653.

Wankiewicz, A. (1979), A review of water movement in snow, Proceeding Modelling Snowcover Runoff, *Cold Regions Research and Engineering Laboratory*, Hanover, New Hampshire, 222-252.

Wever, N., T. Jonas, C. Fierz, and M. Lehning (2014a), Model simulations of the modulating effect of the snow cover in a rain on snow event, *Hydrol. Earth Syst. Sci.*, *11*, 4971–5005, doi:15194/hessd-11-4971-2014.

Wever, N., C. Fierz, C. Mitterer, H. Hirashima, and M. Lehning (2014b), Solving Richards Equation for snow improves snowpack meltwater runoff estimations in detailed multi-layer snowpack model, *The Cryosphere*, *8*(1), 257–274, doi:15194/tc-8-257-2014.

Wever, N., Schmid, L., Heilig, A., Eisen, O., Fierz, C., and M. Lehning (2015), Verification of the multi-layer SNOWPACK model with different water transport schemes, *The Cryosphere*, 9, 2271-2293, doi:15194/tcd-9-2271-2015.

Wever, N., Wurzer, S., Firez, C., and M. Lehning (2016), Simulating ice layer formation under the presence of preferential flow in layered snowpacks, *The Cryosphere*, 10, 2731-2744, doi:15194/tc-10-2731-2016.

Würzer, S., Wever, N., Juras, R., Lehning, M., and T. Jonas (2017), Modelling liquid water transport in snow under rain-on-snow conditions – considering preferential flow, *Hydrol. Earth. Syst. Sci.*, 21, 1741-1756, doi:15194/hess-21-1741-2017.

Yamaguchi, S., Katsushima, T., Sato, A., and T. Kumakura (2010), Water retention curve of sow with different grain sizes, *Cold Regions Science and Technology*, 64(2), 87-93, doi:11016/j.coldregions.20105.008.

Yamaguchi, S., Watanabe, K., Katsushima, T., Sato, A., and T. Kumakura (2012), Dependence of the water retention curve of snow on snow characteristics, *Annals of Glaciology*, 53(61), 6–12, doi:13189/2012AoG61A001.

Zhang, H., and P. A. Zegeling (2017), A numerical study of two-phase flow models with dynamic capillary pressure and hysteresis, *Transp. Porous Media*, 116, 825-846, doi:11007/s11242-016-0802-z.

CHAPTER 2

A DUAL PATHWAY HETEROGENEOUS FLOW THROUGH SNOW MODEL[1]

Abstract

Accurate estimation of snowmelt flux is of primary importance for runoff prediction, which is used for water management and flood forecasting. Lateral flows and preferential flow pathways in porous media flow have proven critical for improving soil and groundwater flow models, but though many physically-based layered snowmelt models have been developed, only 1D matrix flow is accounted for in snow models. Therefore, there is a need for snowmelt models that include these processes to examine the potential to improve snowmelt discharge timing and contributing area in hydrological modelling. An initial a two-dimensional snow model is presented that simulates vertical and lateral water flows through the snow matrix and preferential flow paths, internal energy fluxes, melt, and refreezing. The dual pathway model utilizes an explicit finite volume method to solve for the energy and water flux equations over an orthogonal grid. Energy available at the snow surface, and soil slope angle are set as model inputs. The initial conditions include the number of snow layer, their properties (density and grain size), temperatures, and liquid water contents. This 2D multi-layered flow through snow model is an important tool to help understand snowmelt flow processes in complex and level terrains and how snowmelt-derived runoff forecasting might be improved.

[1] Leroux, N., and J.W. Pomeroy (2015), A dual pathway heterogeneous flow through snow model, in *Proceedings of the 72nd Eastern Snow Conference*, 3-14. Nicolas Leroux is the lead author and investigator of this manuscript. John Pomeroy provided assistance with conceptualization, editorial assistance and discussion of the results.

2.1 Introduction

To accurately predict the timing and magnitude of snowmelt runoff from deep snowpacks, water flow percolation within snow must be understood (*Male and Gray*, 1975; *Wankiewicz*, 1979). Liquid water flow within the snowpack is influenced by the internal properties of the snowpack. Deeper, colder snowpacks have slower outflow rates due to refreezing of percolating meltwater and a longer distance for meltwater to reach the bottom of the snowpack; this lag and attenuation in timing of meltwater delivery to the soil surface make the process important for runoff and streamflow generation in mountains. Amongst the snowpack's internal properties, ice layers and preferential flow paths (PFP) greatly impact the spatial and temporal distributions of snowmelt runoff (*Marsh and Woo*, 1984a; *Marsh*, 1991). Many simplifications and theories have arisen to describe gravitational vertical flow percolation within a homogeneous, isothermal snowpack (*Colbeck*, 1972), water percolation through a subfreezing, layered snowpack with phase change (*Illangasekare et al.*, 1990), or the influence of capillary forces on the water flow (*Jordan*, 1995).

Several numerical snowmelt models of differing levels of complexity have been developed in the past decades. *Tseng et al.* (1994) developed a complex two-dimensional snow model based on the theory of *Illangasekare et al.* (1990), but this model has not been validated against in-situ data and does not incorporate PFP. *Marsh and Woo* (1985) created a one-dimensional model that assumed mass flow through different flow pathways; however, this 1D model does not include lateral flows, the delay of water flow due to ice layers, and assumed that each flow path extends over the complete depth of the snowpack. No operational snow model in hydrological models or land surface schemes can predict lateral flows, the formations of PFP and ice layers, and their effects on water flow through snow and ground thermal regime; this results in inaccuracy in the prediction of catchment discharge and meltwater delivery to soil (*Pomeroy et al.,* 1998). In this paper, a novel two-dimensional snowmelt model solving for the mass and energy flows is presented. The model includes an implementation of the theory of *Hirashima et al.* (2014) to simulate the formation of PFP. The importance of the parameterization of the water entry pressure for dry snow and lateral heterogeneities in snow grain size and density are demonstrated.

2.2 Mathematical Model

2.2.1 Water Flow through Snow

The mass flow within a snowpack is estimated by solving for the two-dimensional Richards equation (Eq. 2.1).

$$\frac{\partial \theta_{\mathrm{w}}}{\partial t} + \nabla \boldsymbol{q} = S_{\mathrm{s}} \tag{2.1}$$

where $\boldsymbol{q}$ is the macroscopic flow velocity [m s^{-1}] (Eq. 2.2) and S_{s} is a mass sink term due to refreezing of liquid melt water in each layer [s^{-1}].

The macroscopic flow velocity in an unsaturated medium is commonly estimated from Darcy-Buckhingam's law under the condition that the flow is laminar (Reynolds Number < 1).

$$\boldsymbol{q} = -K(\theta_{\mathrm{w}})\, \nabla(P_{\mathrm{c}}(\theta_{\mathrm{w}}) + z) \tag{2.2}$$

where $K(\theta_{\mathrm{w}})$ is the unsaturated hydraulic conductivity [m s^{-1}] and $P_{\mathrm{c}}(\theta_{\mathrm{w}})$ is the capillary pressure [m]. For unsaturated porous media, both are functions of the water content.

In snow science, studies have been conducted to establish relationships between snow hydraulic properties and water content. *Calonne et al.* (2012) developed a relationship between saturated hydraulic conductivity (K_{s}), dry snow density, and optical grain size, which is the equivalent radius of sphere of equivalent volume-to-surface area-ratio of a true snow grain population (*Grenfell and Warren*, 1999), through three-dimensional numerical computations (Eq. 2.3). Knowing the saturated hydraulic conductivity, the unsaturated hydraulic conductivity can be estimated (e.g. *Colbeck and Davidson*, 1973).

$$K_{\mathrm{s}} = 3\frac{\rho_{\mathrm{w}} g}{\mu_{\mathrm{w}}} {r_{\mathrm{opt}}}^2 \exp\left(-0.013\rho_{\mathrm{ds}}\right) \tag{2.3}$$

with g the acceleration by gravity [m s^{-2}], μ_{w} is the dynamic viscosity of water [Pa s], r_{opt} is the optical grain radius [m] and ρ_{ds} is the dry snow density [kg m^{-3}].

2.2.1.1 Snow water retention curves

The Water Retention Curve (WRC) is the relationship between capillary pressure and liquid water content. Analogous to flow through unsaturated soil, the snow WRC (Fig. 2.1) has hysteretic behaviour (*Adachi et al*., 2012). *Yamaguchi et al.* (2012) developed a WRC for snow based on the van Genuchten model (Eq. 2.4). Through laboratory experiments, they found empirical equations to link the parameters α^d and n^d (cf. Eq. 2.4) with dry snow density and optical grain size Eq. 2.5. However, this WRC was developed only for drying snow, i.e. the snow was initially saturated with water and liquid water was drained from it.

$$S_{\mathrm{w}} = \left(1 - |\alpha^d P_{\mathrm{c}}|^{n^d}\right)^{-m^d} \tag{2.4}$$

where S_{w} is the effective saturation ($S_{\mathrm{w}} = (\theta_{\mathrm{w}} - \theta_{\mathrm{wr}})/(\phi - \theta_{\mathrm{wr}})$, with ϕ the snow porosity and θ_{wr} the irreducible water content), and α^d, n^d, and m^d are parameters (Eq. 2.5 and 2.6), with m^d chosen as $m^d = 1 - 1/n^d$.

$$\alpha^d = 4.4\mathrm{e}^6 \left(2\frac{\rho_{\mathrm{ds}}}{r_{\mathrm{c}}}\right)^{-0.98} \tag{2.5}$$

$$n^d = 1 + 2.7\mathrm{e}^{-3} \left(2\frac{\rho_{\mathrm{ds}}}{r_{\mathrm{c}}}\right)^{0.61} \tag{2.6}$$

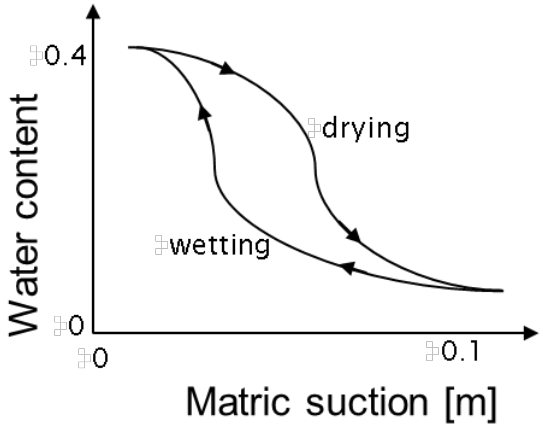

Figure 2.1 Conceptual representation of the hysteretic behaviour between matric suction and liquid water content in the snow water retention curve.

However, in the case of wetting snow, i.e. snow that is initially dry and into which liquid water infiltrates, the model of *Yamaguchi et al.* (2012) is not applicable. Therefore, in the 2D model presented here, a new value of water entry pressure is taken from the study by *Katsushima et al.* (2013) when the initial water content is below the irreducible water content level (dry snow), which is the liquid water content retained within the pore space by capillary forces. The snow WRC developed by *Yamaguchi et al.* (2012) is used to estimate the capillary pressure when the water content is above the irreducible water content (wet snow).

2.2.2.2 Implementation of water entry pressure for wetting snow in a snow model

The impact of implementing a new water entry pressure for dry snow is presented through an example analyzing flow through two different snow layers. The upper layer (layer 1, a wet dense snow layer) has a dry density of 350 kg m^{-3} and an optical grain diameter of 0.3 mm. The lower layer (layer 2, a dry ice layer) has a density of 450 kg m^{-3} and an optical grain diameter of 0.7 mm (Fig. 2.2).

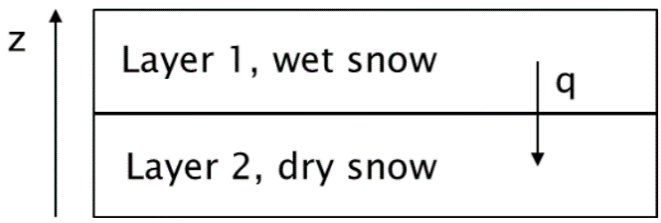

Figure 2.2 Representation of the two snow layers

The flux q between layer 1 and layer 2 was analyzed for two different cases:

- Variable water entry pressure: the model by *Yamaguchi et al.* (2012) is used for the upper wet snow layer and the water entry pressure equation from *Katsushima et al.* (2013) is used for the lower dry snow layer.
- Wet water entry pressure: the model by *Yamaguchi et al.* (2012) is used for both dry and wet snow layers.

The flux q from layer 1 to layer 2 can be estimated using the Darcy-Buckingham's law (Eq. 2.4) and liquid water flows from layer 1 to layer 2 only when q is positive.

Figure 2.3 shows the change of q/K_s with liquid water content in layer 1 for the two different cases considered. It can be observed that introducing a new water entry pressure for dry snow allows much more liquid water to accumulate in layer 1 before initiating downward flow (q>0) and that this has the potential to simulate the ponding of liquid water at snow layer interfaces that is observed in nature.

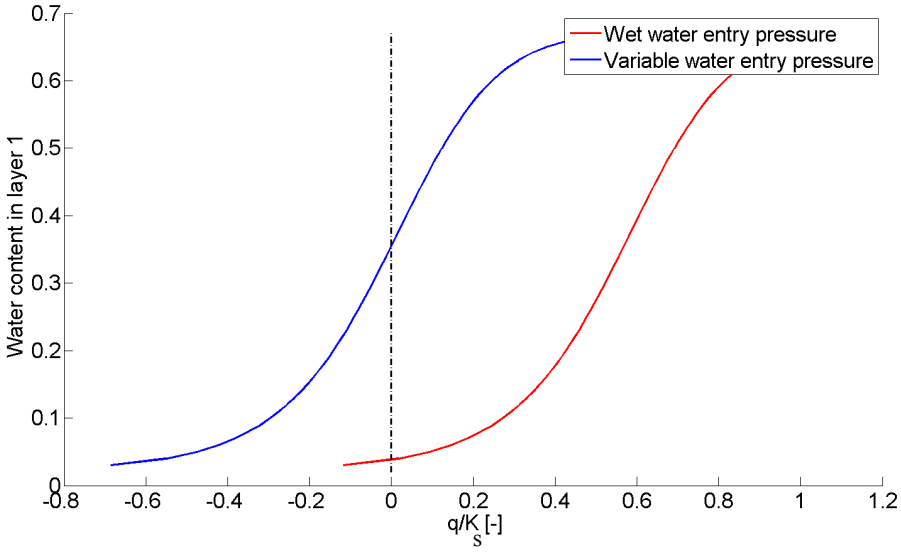

Figure 2.3 Change of liquid water in layer 1 with q/K_s.

2.2.1.3 Implementation of snow heterogeneities

In their theoretical study on the triggering of PFP formation, *Hirashima et al.* (2014) suggested PFP are due to spatial heterogeneities in snow grain size. The impact of fluctuating the snow grain size around the mean layer value on the water flow is therefore discussed here. Using the previous modelling example (Fig. 2.2), three cases are considered: i) the grain size in layer 2 is unchanged, ii) it is decreased by 1% and iii) it is increased by 1%. Figure 2.4 shows the water content in layer 1 as function of the flux q/K_s for the three different grain sizes in layer 2. It can be observed that water flow from layer 1 to layer 2 occurs first when there is a smaller grain size in layer 2: for this case the downward flux (q) becomes positive at lower water contents in layer 1.

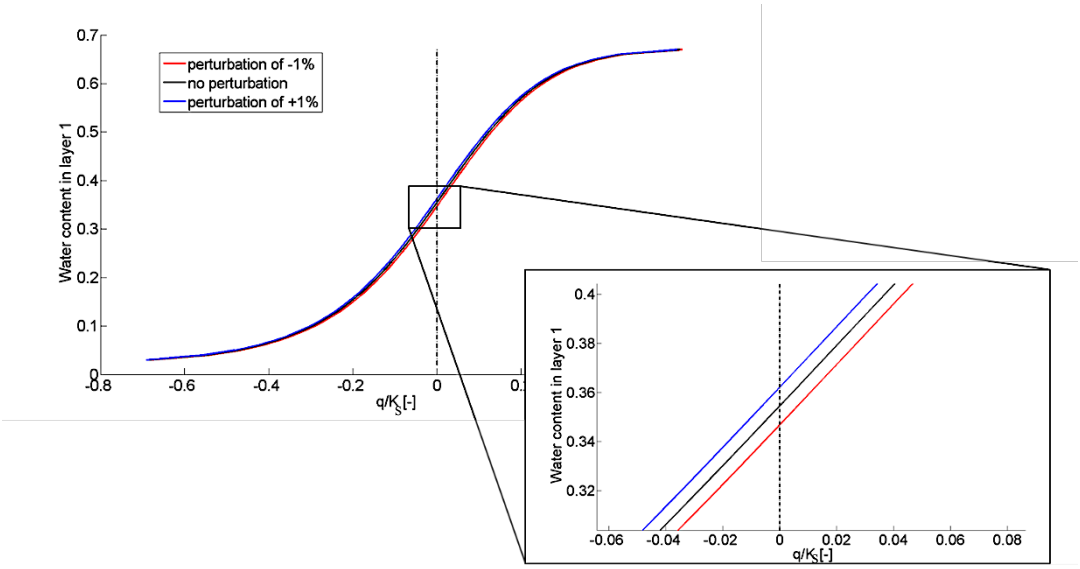

Figure 2.4 Change in the ratio q/K_s for different three grain sizes in layer 2

2.2.2 Snowpack Ablation and Melt

A melting snow surface is a moving boundary at which heat transfer and phase change occur simultaneously. To estimate heat transfer and phase change at this moving boundary, the Stefan condition is solved (Eq. 2.7) (e.g. *Tseng et al.*, 1994).

$$Q_n = -\kappa_s \frac{\partial T}{\partial z}(z = h) \quad \text{if} \quad T_s < 0°C \tag{2.7a}$$

$$Q_n = L_f \rho_s V_n \quad \text{if} \quad T_s = 0°C \tag{2.7b}$$

and Q_n is the heat flux at the surface [W m^{-2}], κ_s is the thermal conductivity [W (K m)$^{-1}$], $\partial T/\partial z$ the vertical temperature gradient at the surface [K m^{-1}], L_f the latent heat of fusion of ice [J kg^{-1}], ρ_s the snow density [kg m^{-3}], V_n the velocity of the melting snow surface [m s^{-1}], and T_s is the snow surface temperature [K].

The infiltration rate (Q_{inf} in [m s^{-1}], Eq. 2.8) is estimated from the vertical velocity of the melting snow surface (V_n):

$$Q_{inf} = V_n\left(\frac{\rho_s}{\rho_w} + \theta_w\right) \tag{2.8}$$

where ρ_w the density of water [kg m^{-3}] and θ_w is the volumetric liquid water content within the melting volume. The infiltration rate, estimated from the energy available at the surface of the snowpack, is then used as a boundary condition for the water flow equations.

2.2.3 Refreezing of Liquid Water

In a wet subfreezing snowpack, heat and momentum transfers occur between the flowing liquid water and the solid phase. *Illangasekare et al.* (1990) developed a theory describing refreezing of meltwater in a subfreezing snowpack. They expressed the maximum mass of liquid water per unit volume of snow (m_{max}) that must freeze to raise the snow temperature to zero, i.e. to raise the snow cold content to zero as,

$$L_f m_{max} = -\rho_s C_{p,i} T \tag{2.9}$$

where T is the snow temperature [K] and $C_{p,i}$ is the specific heat capacity of ice [J (kg K)$^{-1}$].

However, the real mass of liquid water per unit volume of snow that refreezes during a numerical time step (m_f) is always less than or equal to m_{max}, as m_f is limited by the liquid water content available in the snow layer. The new snow layer temperature at the end of a numerical time step Δt can then be estimated from:

$$T^{t+\Delta t} = \frac{\rho_s^t C_{p,i} T^t + m_f L_f}{\rho_s^{t+\Delta t} C_{p,i}} \tag{2.10}$$

At the end of the same time step, snow porosity (ϕ), effective water saturation (S_w), and snow density (ρ_s) are also updated:

$$\phi^{t+\Delta t} = \phi^t + \frac{m_f}{\rho_i} \tag{2.11}$$

$$S_w^{t+\Delta t} = \frac{\theta_w{}^t - \frac{m_f}{\rho_w}}{\phi^{t+\Delta t}} \tag{2.12}$$

$$\rho_s^{t+\Delta t} = \rho_s + m_f \tag{2.13}$$

2.2.4 Heat Transfers in Snow

To simulate heat transfers in the snowpack, the two-dimensional heat conduction equation is solved following *Albert and McGilvary* (1992):

$$\left(\rho C_{\mathrm{p}}\right)_s \frac{\partial T}{\partial t} = \frac{\partial}{\partial x_k}\left(\kappa_{\mathrm{s}} \frac{\partial T}{\partial x_k}\right) \text{ with } k\text{=1,2 representing the two spatial directions} \quad (2.14)$$

such that $\left(\rho C_{\mathrm{p}}\right)_s = \left(\rho_{\mathrm{a}}\theta_{\mathrm{a}}C_{\mathrm{p,a}}\right) + \left(\rho_{\mathrm{w}}\theta_{\mathrm{w}}C_{\mathrm{p,w}}\right) + \left(\rho_{\mathrm{i}}\theta_{\mathrm{i}}C_{\mathrm{p,i}}\right)$.

Calonne et al. (2011) conducted three-dimensional numerical computations of snow conductivity through the air and ice phases. They developed an empirical relationship between the thermal conductivity and the dry snow density:

$$\kappa_{\mathrm{s}} = 2.5\mathrm{x}10^{-6}\,\rho_{\mathrm{ds}}^2 - 1.23\mathrm{x}10^{-4}\rho_{\mathrm{ds}} + 0.024 \quad (2.15)$$

2.3 Numerical Model Design

A two-dimensional numerical snow model was developed to solve for the heat and mass fluxes within a two-dimensional, layered, subfreezing snowpack. To solve for the partial differential equations, an explicit finite volume scheme was used over an orthogonal structured mesh (Fig. 2.5). This method considers each numerical cell as a control volume, in which the conservation equations are solved. This approach is commonly applied in computational fluid dynamics models, as it is inherently conservative.

2.3.1 Boundary and Initial Conditions

Neumann boundary conditions were applied at the upper and left-hand boundaries for the mass and heat equations. At the upper boundary, a constant heat flux (Q_{n}in Eq. 2.1) was applied as boundary condition for the heat equation. This flux was then used to estimate the infiltration rate utilized as upper boundary condition for the mass flow equation. The left-hand boundary condition was a no-flow boundary, whereas the lower and right-hand boundary conditions were set as free boundary conditions, i.e. water was allowed to drain through these two boundaries by gravity flow.

The snowpack and its properties were initialized before running the model. These data include the snowpack slope angle (β in Fig. 2.5), the snowpack layering system, and the mean layer properties

– mean porosities, water contents, mean optical grain sizes, and temperatures. The density and optical grain size in each numerical cell was varied randomly around the mean snow layer density and optical grain size. The density and optical grain size of each cell fluctuated by less than 1% of the mean density and optical grain size values of each layer. For initially dry snow, a new water entry pressure was used to estimate the snow capillary pressure.

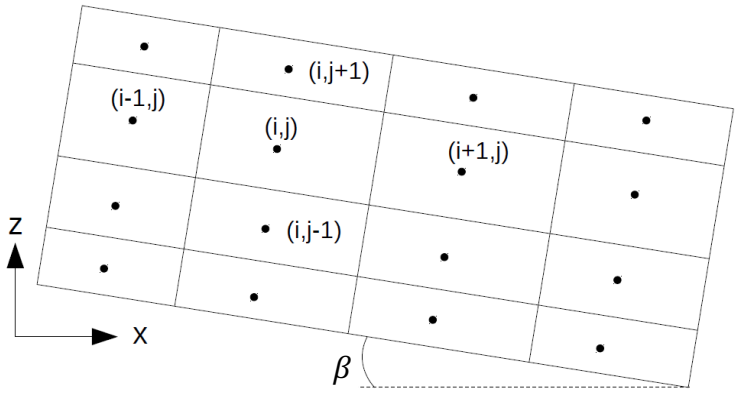

Figure 2.5 Mesh used to represent a layered sloping snowpack

2.3.2 Model Assumptions

Water flow within a layered, subfreezing snowpack is a complex physical process, and this complexity increases when it is coupled with heat transfer. Therefore, due to the lack of complete understanding of the physics of these processes, it is necessary to make assumptions while developing a numerical snow model. The assumptions made in this model also indicate current knowledge and how this limits snow melt modelling of water flow through snow. These assumptions are:

1 The change of grain size due to temperature gradient and presence of liquid water was not simulated. This assumption might impact the velocity of the flowing liquid water.
2 The irreducible water content is assumed constant for the whole snowpack.
3 Thermal convection, condensation, and sublimation within the snowpack are not simulated.
4 Heat conduction dominates the heat transfers.
5 Freezing point depression effects on snow grains is neglected.
6 The lateral heterogeneities in snow grain size and density are randomly distributed over space.
7 The water entry pressure for dry snow is function only of snow grain size.

8 Temperature, density, and water content are computed at the centre point of each cell and are assumed homogeneous within the cell.

2.4 Model Applications

A first model simulation of water and heat flow through a subfreezing, layered snowpack is demonstrated. The snowpack was divided into four horizontal snow layers (Table 2.2, Fig. 2.6). The third layer (from the bottom of the snowpack) is an ice layer with a higher density than the other layers. Under natural conditions, flowing liquid water accumulates over this layer and preferential flow paths were observed to form below a saturated horizontal layer (*Marsh and Woo*, 1984a).

Table 2.1 summarizes the parameters and inputs used in the model as initial and boundary conditions. The values used for the mean optical grain sizes in Table 2.2 were computed from the average specific surface areas measured by *Montpetit et al.* (2012) for different types of snow. Layer grain size and density randomly fluctuated in each numerical cell around the snow layer mean properties (Table 2.1) by less than 1 %. The fluctuating density within each snow layer can be seen in Fig. 2.6.

The simulation was run until the snowpack completely melted. Figures 2.7 and 2.8 show the water content distribution within the snow layers after 2h45min and 4h10min of melt, respectively. It can be observed that liquid water accumulated above the ice layer (Fig. 2.7). Then, preferential flows occurred where the grain size in the ice layer was smaller due to the grain size fluctuation implemented (Fig. 2.8) (cf. Section 2.2.2.3).

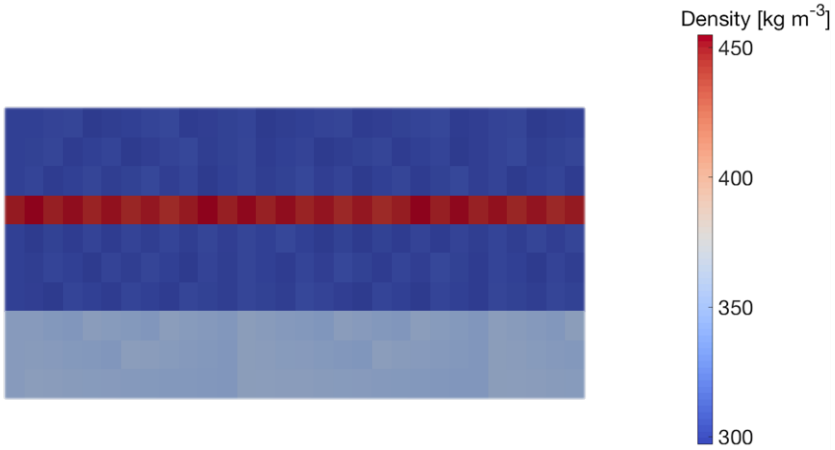

Figure 2.6 Initial dry density of each snow layer

Table 2.1 Inputs used for the simulation

Horizontal length of snowpack	2 m
Snow depth	1 m
Number of horizontal cells	30
Number of vertical cells	10
Ground slope angle	0^{o}
Temperature at the interface snow-soil	0^{o}C
Energy at the surface	500 W m^{-2}
Irreducible water content	0.02

Table 2.2 Snow matrix properties

	Type of snow	Thickness [m]	Temperature [^{o}C]	Mean density [kg m^{-3}]	Mean optical grain diameter [mm]
Layer 1 (bottom)	Compact snow	0.3	-2	350	0.5
Layer 2	Dense rounded snow	0.3	-2	300	0.3
Layer 3	Ice layer	0.1	-2	450	0.7
Layer 4	Dense rounded snow	0.3	-2	300	0.3

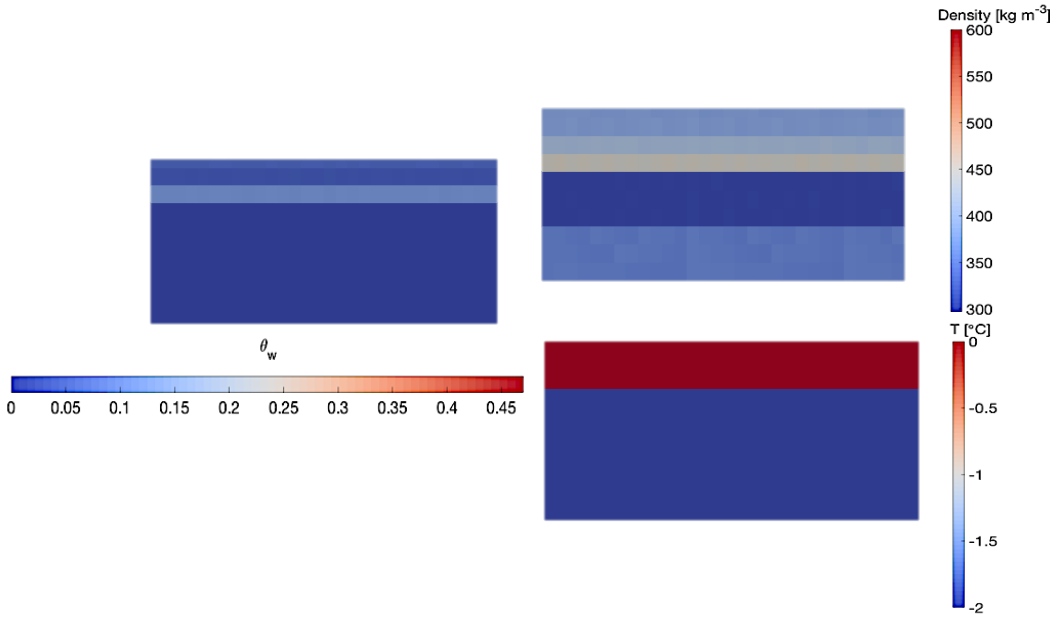

Figure 2.7 Water content, density and temperature distributions in the snowpack after 2h45min of melt.

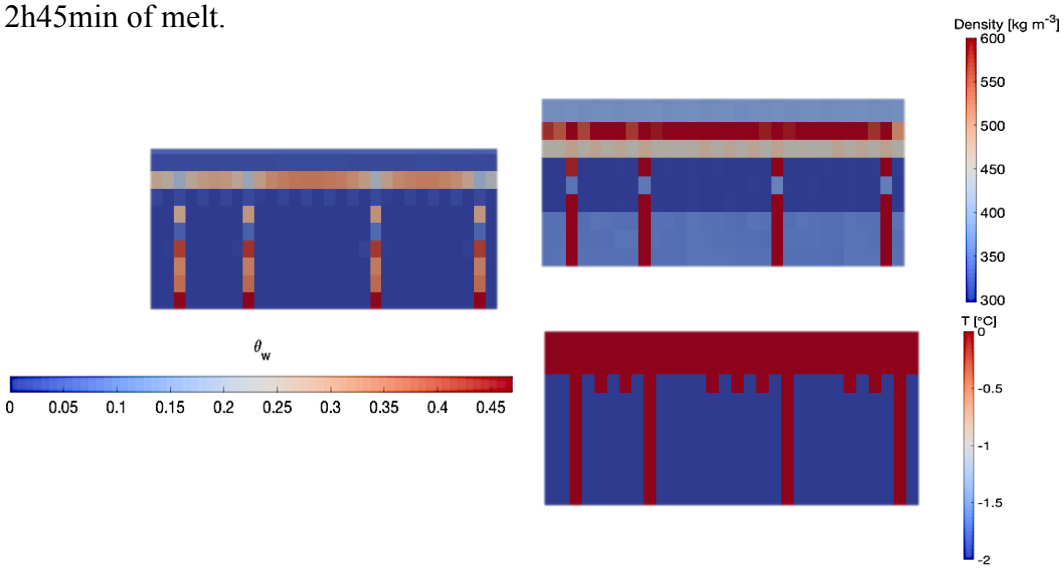

Figure 2.8 Water content, density and temperature distributions in the snowpack after 4h10min of melt.

A second model application of water flow through a sloping snowpack is demonstrated (Fig. 2.9 and 2.10). The same initial conditions are applied as before, but the snowpack is now tilted by 5°. Figures 2.9 and 2.10 show the water content distribution within the sloping snowpack after 1h45min and 1h50min of melt, respectively. It is observed that PFP formed at the downhill section of the snowpack (Fig. 2.9) due to a higher water content in this area from lateral flows above the ice layer. After the formation of PFP, liquid water flowed laterally (Fig. 2.10).

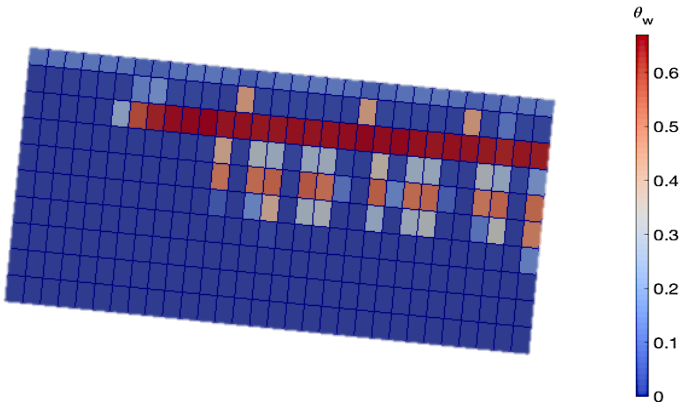

Figure 2.9 Water content distribution within a sloping snowpack after 1h45min of melt.

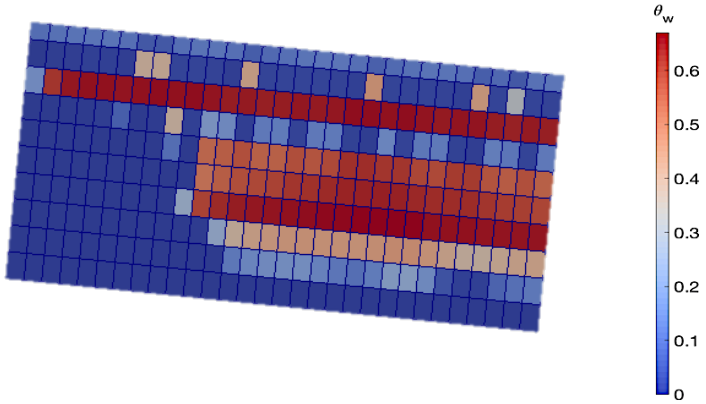

Figure 2.10 Water content distribution within a sloping snowpack after 1h50min of melt.

2.5 Conclusions

A first attempt to model mass and energy flows through a initially dry, layered, sloping snowpack with PFP formation has been demonstrated. Two parameters have been introduced and explored for their role in triggering the formation of preferential flows – a water entry pressure for dry snow and a fluctuation in snow grain size and density to simulate lateral heterogeneities in their properties. In the model applications presented here, the spatial distributions of the fluctuations were random. Therefore, further work should be carried on to establish relationships between these parameters and snow matrix properties from field observations.

This two-dimensional snow model needs to be validated against in-situ or laboratory data. A field study is being designed to validate each physical process simulated by the model. The development

of this numerical model raises questions on water flow through snow and numerical snow modelling:

- Does the irreducible water content depend on snow properties?
- How should the hydraulic conductivity and thermal conductivity be numerically computed at the interface of two numerical nodes?
- How should grain size fluctuations be represented?
- How should the water entry pressure for dry snow be related to snow density?
- Does all the available liquid water that can refreeze (m_{max}) do so during a numerical time step (*Illangasekare et al*., 1990)?
- Is the flow through preferential flow paths laminar? Does Darcy's law always apply?
- Can the equation used for the thermal conductivity in a dry snowpack (Eq. 2.12) be used when liquid water content is present within the snowpack?
- Does liquid water refreeze at 0°C or is there a freezing point depression that depends on snow properties and surface tension between ice and liquid water?

Key Points for the Next Chapter

- How does this model perform when compared to laboratory data?
- How can the water retention curve, currently limited to a drainage curve, be improved?
- By coupling heat transfer and preferential flow, can ice layers be simulated for the first time in a snowmodel?

2.6 References

Adachi S., Yamaguchi S., Ozeki T., and K. Kose (2012), Hysteresis in the water retention curve of snow measured used an MRI system, *ISSW Proceedings 2012*, *Anchorage, Alaska,* 918-922.

Albert M. and W. McGilvary (1992), Thermal effects due to air flow and vapor transport in dry snow. *Journal of Glaciology*, 38(129), 273–281.

Calonne N., Geindreau C., Flin F., Morin S., Lesaffre B., Rolland Du Roscoat S., and P. Charrier (2012), 3-D image-based numerical computations of snow permeability: links to specific surface area, density, and microstructural anisotropy. *The Cryosphere*, 6, 939–951.

Colbeck S. (1972), A theory of water percolation in snow. *Journal of glaciology*, 11(63), 369–385.

Colbeck S. and G. Davidson (1973), Water percolation through homogeneous snow. *Proceedings, the Role of Snow and Ice in Hydrology*, 4, 242–257.

Male D. H., and D. Gray (1975), Problems in developing a Physically Based Snowmelt Model. *Canadian Journal of Civil Engineering*, 2(4), 474–488.

Hirashima H., Yamaguchi S., and T. Katsushima (2014) A multi-dimensional water transport model to reproduce preferential flow in the snowpack, *Cold Regions Science and Technology*, 108, 80-90

Grenfell, T.C. and S.G. Warren (1999), Representation of a nonspherical ice particle by a collection of independent spheres for scattering and absorption of radiation, *J. Geophys. Res.*, 104, 31697–31708.

Illangasekare T. H., Walter R. J., Meier M. F., and W. T. Pfeffer (1990), Modeling of meltwater infiltration in subfreezing snow. *Water Resources Research*, 26(5), 1001–1012.

Jordan R. (1995), Effects of capillary discontinuities on water flow and water retention in layered snowcovers. *Defence Science Journal*, 45(2), 79–91.

Katsushima T., Yamaguchi S., Kumakura T., and A. Sato (2013), Experimental analysis of preferential flow in dry snowpack, *Cold. Reg. Sci. Technol.*, 85, 206-216.

Marsh P. (1991), Water flux in melting snow covers. Chapter 2 in: M.Y. Corapcioglu (Editor). *Advances in porous media*, Vol. 1, Elsevier, Amsterdam, 61–124.

Marsh P. and M. Woo (1984), Wetting front advance and freezing of meltwater within a snow cover: 1. Observations in the Canadian Arctic. *Water Resources Research*, 20(12), 1853–1864.

Marsh P. and M. Woo (1985), Meltwater movement in natural heterogeneous snow covers. *Water Resources Research*, 21(11), 1710–1716.

Montpetit B., Royer A., Langlois A., Cliche P., Roy A., Champollion N., Picard G., Domine F., and R. Obbard (2012), New shortwave infrared albedo measurements for snow specific surface area retrieval, *Journal of Hydrology*, 58 (211), 941-952.

Pomeroy J.W., Gray D.M., Shook K.R., Toth B., Essery R.L.H., Pietroniro A., and N. R. Hedstrom (1998), An evaluation of snow accumulation and ablation processes for land surface modelling, *Hydrological Processes*, 12, 2339-2367.

Tseng P., Illangesakare T., and M. Meier (1994), Modeling of snow melting and uniform wetting front migration in a layered subfreezing snowpack. *Water Resources Research*, 30(8), 2363–2376.

Yamaguchi S., Watanabe K., Katsushima T., Sato A., and T. Kumakura (2012) Dependence of the water retention curve of snow on snow characteristics. *Annals of Glaciology*, 53(61), 6–12.

CHAPTER 3

MODELLING CAPILLARY HYSTERESIS EFFECTS ON PREFERENTIAL FLOW THROUGH MELTING AND COLD LAYERED SNOWPACKS[2]

Abstract

Accurate estimation of the amount and timing of water flux through melting snowpacks is important for runoff prediction in cold regions. Most existing snowmelt models only account for one-dimensional matrix flow and neglect to simulate the formation of preferential flow paths. Consideration of lateral and preferential flows has proven critical to improve the performance of soil and groundwater porous media flow models. A two-dimensional physically-based snowpack model that simulates snowmelt, refreezing of meltwater, heat and water flows, and preferential flow paths is presented. The model assumes thermal equilibrium between solid and liquid phases and uses recent snow physics advances to estimate snowpack hydraulic and thermal properties. For the first time, capillary hysteresis is accounted in a snowmelt model. A finite volume method is applied to solve for the 2D coupled heat and mass transfer equations. The model with capillary hysteresis provided better simulations of water suction at the wet to dry snow interface in a wetting snow sample than did a model that only accounted for the boundary drying curve. Capillary hysteresis also improved simulations of preferential flow path dynamics and the snowpack discharge hydrograph. Simulating preferential flow in a subfreezing snowpack allowed the model to generate ice layers, and increased the vertical exchange of energy, thus modelling a faster warming of the snowpack than would be possible without preferential flow. The model is thus capable of simulating many attributes of layered natural melting snowpacks. These features not only qualitatively improve water flow simulations, but give insights on the physics impacting

[2] Leroux, N. R. and J. W. Pomeroy (2017), Modelling capillary hysteresis effects on preferential flow through melting and cold layered snowpacks, *Adv. in Water Res.*, 107, 250-264, https://doi.org/11016/j.advwatres.2017.06.024. Nicolas Leroux is the lead author and investigator of this manuscript. John Pomeroy provided assistance with conceptualization, editorial assistance and discussion of the results.

snowmelt flow processes for both level and sloping terrain, such as the effect of a more realistic water retention curve on the shape and spatial distribution of preferential flow paths and the coupling between preferential flow and heat transfer in subfreezing snowpacks responsible for ice layer formation. This research also illuminates how uncertainty in snowmelt-derived runoff calculations might be reduced through the inclusion of more realistic preferential flow through snowpacks.

3.1 Introduction

To accurately predict the timing and magnitude of snowmelt water release from deep cold snowpacks, water percolation within snow must be understood (*Male and Gray*, 1975; *Wankiewicz*, 1979). Percolation is greatly influenced by snowpack internal properties, such as grain sizes that evolve rapidly during melt due to the presence of liquid water (e.g. *Brun*, 1989). Due to internal refreezing, deeper, colder snowpacks have delayed flow rates (e.g. *DeBeer and Pomeroy*, 2010). Refreezing may result in the formation of ice layers within cold snowpacks, which impede the vertical flow of water (e.g. *Pfeffer and Humphrey*, 1996). Flow of water through snowpacks is a complex physical process that can be considered as two parts – matrix flow and preferential flow (*Marsh and Woo*, 1984a; *Marsh*, 1991; *Waldner et al.*, 2004). Preferential flowpaths (PFP) advance the flow of liquid water through the snowpack, ahead of the matrix wetting front, advancing the celerity of flow (e.g. *Marsh and Woo*, 1984a). These flow and internal phase change processes cause a lag and attenuation in timing of meltwater delivery to the soil surface, which is important for modelling runoff and streamflow generation.

Matrix flow through snowpacks has been described as vertical flow percolation by gravity within a homogeneous, isothermal snowpack (*Colbeck*, 1972; *Colbeck and Davidson*, 1973). Refreezing of matrix flow percolating into a two-dimensional subfreezing, layered snowpack has been investigated by *Illangasekare et al.* (1990), *Pfeffer et al.* (1990), and *Daanen and Nieber* (2009). The influence of capillary forces on water flow has been represented by implementing Richards equation in snow models (*Jordan*, 1995; *Hirashima et al.*, 2010; *Wever et al.*, 2014b, 2015).

Numerical snowmelt models with varying complexity have been created in the past decades. The conceptual model Flow Impeding Neutral or Accelerating (FINA) (*Wankiewicz*, 1979) theorized

on the acceleration or impedence of matrix water flow at the interface of two snow layers depending on the gravity flow pressure of each layer; but no field data were available to test and validate the conceptual model. *Marsh and Woo* (1984b, 1985) created for the first time a one-dimensional model that accounted for the mass flow through PFP, assumed to extend over the complete depth of the snowpack; this theory did not include lateral flows or the delay of water flow due to ice layers within the snow. *Tseng et al.* (1994a) developed a complex two-dimensional snow model implementing snowpack ablation following the theory of *Illangasekare et al.* (1990) to predict matrix flow through subfreezing snow; however, the model was unable to simulate the formation of PFP. No existing hydrological snow models (e.g. SNTHERM, *Jordan*, 1991; or Snobal, *Marks et al.*, 1999) or land surface schemes (e.g. CLASS, *Verseghy*, 1991) include simulation of lateral flows, the formation of PFP and ice layers, or their effects on water movement through snowpacks. This results in inaccuracy in snowpack water and energetics as well as errors in the prediction of catchment discharge and meltwater delivery to soil (*Pomeroy et al.*, 1998). Preferential flow and ice layer formation were recently included in the 1D snow model SNOWPACK (*Wever et al.*, 2016; *Würzer et al.*, 2017) using a dual domain approach to divide the flow between matrix flow and preferential flow, similar to the approach used in soil models (e.g. *Beven and Germann*, 1981). Two coefficients, which had to be estimated, were added to SNOWPACK: the water content threshold to move water from preferential flow to matrix flow and the number of preferential flow paths per square meter. Simulating preferential flow improved the timing of meltwater delivery to the underlying soil early in the melt season and during rain-on-snow events and was essential to the formation of ice layers; however, their model could only represent 20% of the ice layers observed in natural snowpacks.

The formation of PFP in soil has been studied for decades. *Hill and Parlange* (1972) demonstrated that PFP form at unstable wetting fronts after ponding of liquid water at the interface of fine to coarse structured layers. *Hillel and Baker* (1988) later emphasized the importance of water-entry suction on the ponding of percolating liquid water at the wet to dry soil interface; they defined water-entry suction as “the maximum suction that will allow water to enter an initially dry porous matrix” characterized by the smallest pores in a layer. Ponded liquid water will penetrate the dry sublayer at randomly distributed locations caused by spatial heterogeneities in suction at the wetting front, creating an unstable wetting front evolving into PFP. In snow, *Wankiewicz* (1978) and *Waldner et al.* (2004) confirmed water ponding by capillary barriers. *Katsushima et al.* (2013)

found that a water-entry suction in snow exists and can be estimated with an equation comparable to the one for soil. *Colbeck* (1979) noticed spatial persistence of PFP in snow after forming due to wet snow metamorphism, i.e. the change of grain size with water content. Under high water contents (funicular regime), the snow grains become more rounded and less cohesive, while they are more bonded in clusters under low water contents (pendular regime). On the other hand, *Schneebeli* (1995) observed that the location of PFP in snow changed after each melt-freeze cycle.

Soil models were developed to represent PFP formation in initially air-dry and hydrophobic sandy soils by applying initially unstable wetting fronts (*Nieber*, 1996; *Ritsema et al.*, 1998). In snow, *Hirashima et al.* (2014a, b, c) developed a multi-dimensional infiltration model to reproduce preferential flows in a snowpack by combining the works of Hillel and Baker (1988) and *Katsushima et al.* (2013). *Hirashima et al.* (2014a, b, c) introduced a water-entry capillary pressure for dry snow and heterogeneities in snow grain size and snow density to allow the formation of PFP. That snow model included the latest improvements made to compute snow hydraulic properties, such as the formulation of snow permeability from *Calonne et al.* (2012) and the empirical model of *Yamaguchi et al.* (2012), which approximates the water retention curve (WRC) - the relationship between liquid water content and capillary pressure - in draining snow. The applicability of the model by *Hirashima et al.* (2014a) was limited to isothermal snow samples, neglecting melting at the surface and refreezing of liquid water. *Davis et al.* (2009) demonstrated that capillary hysteresis was most pronounced in hydrophilic soils than in hydrophobic soils. The existence of a thin liquid layer around ice grains (*Dash et al.*, 1995, 2006) makes snow a hydrophilic porous medium as it reduces the contact angle between the liquid water and the ice crystal; therefore, capillary hysteresis can be expected to have a significant impact on water flow through snow. Hence, the WRC of *Yamaguchi et al.* (2012) is valid only for draining snow. *Adachi et al.* (2012) measured WRC for both draining and wetting snow samples. Laboratory or field experiments determining an equation for WRC for wetting snow have yet to be conducted.

In this paper, a new snowmelt model, Snowmelt Model with Preferential flow Paths (SMPP) that captures the effect of capillary hysteresis is presented. The ability of SMPP to simulate and quantify PFP during the melt of a dry, subfreezing, layered snowpack is demonstrated. A sensitivity analysis on the model inputs and parameters is also presented to identify the most important model variables that influence simulated flow through snow.

3.2 SMPP Mathematical Framework

SMPP is a 2D numerical model that simulates mass and heat fluxes within both sloping and level snowpacks. Melt at the surface and infiltration of liquid water are both computed, as well as refreezing of liquid water when the internal snow temperature is below freezing. This section details the mathematics behind the snow processes included in SMPP.

3.2.1 Snow Ablation and Melt

A melting snow surface can be approximated as a moving boundary at which heat transfer and phase change occur simultaneously. To estimate the heat transfer and phase change at this boundary, the Stefan condition is solved (Eq. 3.1) (e.g. *Tseng et al.*, 1994a). When the snow surface temperature (T_s in [°C]) is below freezing, the heat flux at the surface (Q_n in [W m^{-2}]) is used to warm the snow directly below the surface, otherwise, the heat flux is applied to melt the snow.

$$Q_n = -\kappa_s \frac{\partial T}{\partial z}(z = h) \qquad \text{if} \quad T_s < 0°C \tag{3.1a}$$

$$Q_n = Q_{inf}\, L_f\, \rho_w \qquad \text{if} \quad T_s = 0°C \tag{3.1b}$$

where κ_s is the thermal conductivity [W (K m)$^{-1}$], $\partial T/\partial z$ is the vertical temperature gradient at the surface [K m^{-1}], L_f is the latent heat of fusion of ice [J kg^{-1}], Q_{inf} is the melt rate (infiltration rate) at the snow surface [m s^{-1}] and ρ_w the density of water [kg m^{-3}].

3.2.2 Water Flow

The mass flow between each snow layer is estimated by solving the non-steady state two-dimensional mass conservation equation:

$$\frac{\partial \theta_w}{\partial t} + \nabla . \boldsymbol{q}(\theta_w) = -S_S \tag{3.2}$$

where θ_w is the volumetric liquid water content [m^3 m^{-3}], $\boldsymbol{q}$ is the liquid water flux [m s^{-1}] in the two spatial dimensions (Eq. 3.3) and S_S is a mass sink term coupling the mass conservation equation with the heat equation (Eq. 3.13) through refreezing of liquid melt water [s^{-1}] (Eq. 3.16).

The liquid water flux is approximated from Darcy-Buckingham's law (*Bear*, 1972) assuming a laminar flow:

$$\boldsymbol{q}(\theta_{\mathrm{w}}) = -K(\theta_{\mathrm{w}})\,\nabla(P_{\mathrm{c}}(\theta_{\mathrm{w}}) + z\,cos(\beta)) \tag{3.3}$$

where $K(\theta_{\mathrm{w}})$ is the unsaturated hydraulic conductivity [m s^{-1}], $P_{\mathrm{c}}(\theta_{\mathrm{w}})$ is the pressure head [m], z is the slope normal coordinate [m] (positive upward), and β is the slope angle. For unsaturated porous media (e.g. melting snow), both K and P_{c} are functions of water content and need to be solved for.

Snow hydraulic properties can be estimated from water content. Most recently, *Calonne et al.* (2012) developed a relationship between snow permeability, dry snow density, and optical grain size (right hand side of Eq. 3.4 below) by solving the Stokes flow equation for three-dimensional tomographic images of snow samples. Knowing the snow permeability, the saturated hydraulic conductivities can be estimated by

$$K_{\mathrm{s}} = \frac{\rho_{\mathrm{w}} g}{\mu_{\mathrm{w}}}\,[3\,r_{\mathrm{opt}}^2 \exp\,(-0.013\,\rho_{\mathrm{ds}})] \tag{3.4}$$

where K_{s} is the saturated snow hydraulic conductivity [m s^{-1}], g is the gravitational acceleration [m s^{-2}], μ_{w} is the dynamic viscosity of water [Pa s], r_{opt} is the optical grain radius [m] (equivalent sphere radius), which can be related to mean grain size, sphericity and dendricity (*Vionnet et al.*, 2012), and ρ_{ds} is the dry snow density [kg m^{-3}].

The unsaturated hydraulic conductivity ($K(\theta_{\mathrm{w}})$ in [m s^{-1}]) is then estimated from the saturated hydraulic conductivity using the van Genuchten-Mualem model (*Mualem*, 1976; *van Genuchten*, 1980):

$$K(\theta_{\mathrm{w}}) = K_{\mathrm{s}}\,S_{\mathrm{w}}^{0.5}\left(1 - \left(1 - S_{\mathrm{w}}^{\frac{1}{m}}\right)^{m}\right)^{2} \tag{3.5}$$

where S_{w} is the effective saturation and m is a parameter.

The pressure head ($P_{\mathrm{c}}(\theta_{\mathrm{w}})$) is linked to the liquid water content through the WRC. The van Genuchten equation (*van Genuchten*, 1980) is applied to estimate this relationship:

$$S_{\mathrm{w}} = (1 + |\alpha\,P_{\mathrm{c}}|^{n})^{-m} \tag{3.6}$$

with $S_{\mathrm{w}} = (\theta_{\mathrm{w}} - \theta_{\mathrm{wr}})/(\phi - \theta_{\mathrm{wr}})$ and $\phi = \theta_{\mathrm{a}} + \theta_{\mathrm{w}}$

where θ_{wr} is the irreducible water content [m^3 m^{-3}], ϕ is the snow porosity [m^3 m^{-3}], θ_{a} is the volumetric air content [m^3 m^{-3}], and α [m^{-1}], n [-], and m [-] are parameters, with m chosen as $m = 1 - 1/n$. α is related to the inverse of the air entry pressure head and n is a measure of the pore-size distribution.

3.2.3 Hysteresis Process

Analogous to flow through unsaturated soil, the snow WRC has hysteresis, i.e. the water pressure for a given saturation differs between the wetting and drying processes (*Wankiewicz*, 1979; *Adachi et al.*, 2012) that each follow unique boundary wetting and drying curves, referred hereafter by the superscripts w and d, respectively. *Yamaguchi et al.* (2012) formulated a boundary drying curve for snow based on the van Genuchten equation (Eq. 3.6). Through laboratory experiments, they established empirical equations to link the parameters α^{d} and n^{d} to dry snow density and grain size:

$$\alpha^{d} = 4.4\mathrm{e}^{6}\left(\frac{\rho_{\mathrm{ds}}}{2\,r_{\mathrm{c}}}\right)^{-0.98} \tag{3.7}$$

$$n^{d} = 1 + 2.7\mathrm{e}^{-3}\left(\frac{\rho_{\mathrm{ds}}}{2\,r_{\mathrm{c}}}\right)^{0.61} \tag{3.8}$$

where r_{c} is the mean grain radius [m].

This parameterization was found to provide better results than the previous formulations of *Yamaguchi et al.* (2010) and *Daanen and Nieber* (2009), both depending solely on snow grain size (*Wever et al.*, 2014, 2015).

An equation for a wetting boundary curve in snow has yet to be developed. A wetting boundary curve was implemented in SMPP by scaling the known boundary drying curve using the following constraints, which are commonly applied in soil physics (*Kool and Parker*, 1987):

$$n^{w} = n^{d}, \tag{3.9}$$

$$\theta_{\mathrm{ws}}^{w} = \theta_{\mathrm{ws}}^{d}, \tag{3.10}$$

$$\alpha^w = \gamma\, \alpha^d, \tag{3.11}$$

$$\theta_{\mathrm{wr}}^w = \theta_{\mathrm{wr}}^d\ . \tag{3.12}$$

where θ_{ws}^w and θ_{ws}^d are the liquid water contents at saturation for the boundary wetting and drying curves, respectively, and γ is a coefficient commonly taken as 2.

Likos et al. (2013) found values of γ ranging from 1 to 5.66 depending on soil cohesiveness, with a mean value of 2.2. As this ratio increases, the boundary wetting curve separates further (Ψ becomes lower) from the boundary drying curve. As a value for γ in snow is unknown, a sensitivity analysis on this parameter is shown in Section 3.6.

Nieber (1996) described a main wetting curve starting from dry conditions for hydrophilic soils. This curve was nearly level with P_{c} equal to water entry pressure. Such a curve has yet to be shown to exist in snow, which can also be considered a hydrophilic porous medium. *Katsushima et al.* (2013) did, however, measure a water entry pressure in snow. To represent the water retention functions of *Nieber* (1996), in SMPP, a value of water entry pressure (P_{we} in [m], Eq. 3.13 below) was used when a grid cell was initially dry ($\theta_{\mathrm{w}} \leq \theta_{\mathrm{wr}}$) following the expression from *Katsushima et al.* (2013), which depends solely on grain size.

$$P_{\mathrm{we}} = 0.0437 \left(\frac{1}{r_{\mathrm{c}}\, 2\mathrm{e}^3}\right) + 0.01074 \tag{3.13}$$

Instead of jumping to a boundary curve when $\theta_{\mathrm{w}} > \theta_{\mathrm{wr}}$ (as in *Hirashima et al.*, 2014a), which creates an unrealistic increase of pressure and potentially causes model instabilities, a snow grid cell initially at the water entry pressure stays at this pressure until S_{e} is greater or equal to the saturation estimated on the wetting boundary curve at $P_{\mathrm{c}} = P_{\mathrm{we}}$. It then moves to the wetting boundary curve.

Solving for the above equations can create a numerical error in that a water flux from dry ($\theta_{\mathrm{w}} \leq \theta_{\mathrm{wr}}$) to wet snow can be computed when the water entry pressure of the dry cell (Eq. 3.13) is lower than the pressure in the wet cell (Eq. 3.6). To prevent this, a condition is put on the Darcy-Buckingham's flux, allowing for the flow of water to occur from a wet to a dry layer only when

Eq. 3.3 is positive, i.e. liquid water content accumulates until the pressure in the wetting cell satisfies the condition:

$$P_{\mathrm{c}} < P_{\mathrm{we}} + \Delta z \cos(\beta)\, \delta \tag{3.14}$$

where δ is equal to 0 or 1 in the lateral and vertical directions, respectively.

In contrast to *Hirashima et al.* (2014a) where only a drying boundary curve was applied to calculate the pressure head of both wetting and drying snow, implementing a wetting boundary curve results in lower liquid water content at the wet to dry snow interface, lower hydraulic conductivities, and lower mass flux until the pressure condition (Eq. 3.14) is satisfied. Moreover, when increasing γ, this condition is satisfied for even lower water contents as the suction of the boundary wetting curve decreases.

Scanning curves are implemented using the model proposed by *Huang et al.* (2005). This model was chosen as it forces the closure of the scanning loops, thus preventing artificial pumping errors (*Werner and Lockington*, 2006). To close the loops, the scanning curves are forced to pass through reversal points. Wetting and drying scanning curves ($\theta^{w}(\Psi, p)$ and $\theta^{d}(\Psi, p)$, respectively) are computed from:

$$\frac{\theta^{j}(\Psi, p) - \theta^{j}_{\mathrm{wr}}(p)}{\theta^{j}_{\mathrm{ws}}(p) - \theta^{j}_{\mathrm{wr}}(p)} = \left(1 - \left|\alpha^{j} P_{\mathrm{c}}\right|^{n}\right)^{-m} \tag{3.15}$$

where the superscript j denotes either a wetting or drying scanning curve (w or d, respectively) and p is the order of the scanning curve. Beyond second- or third-order scanning curves, hysteretic effects become small (*Parker and Lenhard*, 1987). To balance between model accuracy and efficiency, computed values of p greater than 90 were kept equal to 90 in SMPP, i.e. no additional scanning curve was computed after the scanning curve of order 90. $\theta^{j}_{\mathrm{wr}}(p)$ and $\theta^{j}_{\mathrm{w,s}}(p)$ can be determined by substituting ($\theta^{j}(P_{\mathrm{c}}, p)$, P_{c}) in Eq. 3.15 by the two reversal points ($\theta^{\Delta}_{\mathrm{dw}}$, P^{Δ}_{dw}) and ($\theta^{\Delta}_{\mathrm{wd}}$, P^{Δ}_{wd}) through which the scanning curve passes (Eq. 3.16 and 3.17). The former is the reversal point when the process switches from drying to wetting and the latter is the reversal point when the process changes from wetting to drying.

$$\frac{\theta_{\mathrm{dw}}^{\Delta} - \theta_{\mathrm{wr}}^{j}(p)}{\theta_{\mathrm{ws}}^{j}(p) - \theta_{\mathrm{wr}}^{j}(p)} = \left(1 - \left|\alpha^{j} P_{\mathrm{dw}}^{\Delta}\right|^{n}\right)^{-m} \tag{3.16}$$

$$\frac{\theta_{\mathrm{wd}}^{\Delta} - \theta_{\mathrm{wr}}^{j}(p)}{\theta_{\mathrm{ws}}^{j}(p) - \theta_{\mathrm{wr}}^{j}(p)} = \left(1 - \left|\alpha^{j} P_{\mathrm{wd}}^{\Delta}\right|^{n}\right)^{-m} \tag{3.17}$$

Figure 3.1 presents an example of the hysteresis model for a snow density of 400 kg m^{-3}, a grain diameter of 1 mm, and γ equal to 2. The wetting and drying processes shown in Fig 3.1, as well as the reversal points (black dots in Fig. 3.1) were actively chosen to illustrate an example of the hysteresis process implemented in the model. The water entry pressure curve (constant line at $P_{\mathrm{c}} = P_{\mathrm{we}}$, represented by the dots) met the boundary wetting curve (blue line). Suction then decreased on the boundary wetting curve until drying occurred and scanning curves were computed (dashed lines). The reversal points of the scanning drying curve 1 are $(\theta_1, P_{\mathrm{c},1})$ and $(\theta_{\mathrm{wr}}, P_{\mathrm{c,r}})$, the scanning wetting curve passes through $(\theta_2, P_{\mathrm{c},2})$ and $(\theta_3, P_{\mathrm{c},3})$ and the scanning drying curve 2 initiates from $(\theta_3, P_{\mathrm{c},3})$ and ends at $(\theta_2, P_{\mathrm{c},2})$.

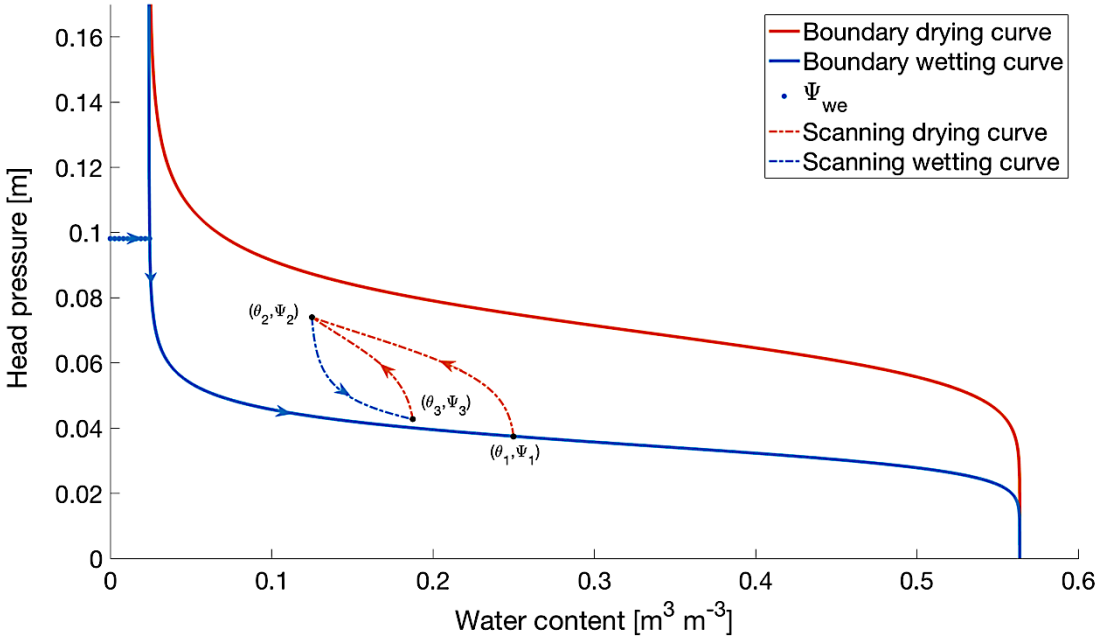

Figure 3.1 Example of the hysteresis model used in SMPP for a snow density of 400 kg m^{-3}, a grain diameter of 1 mm, and $\alpha^{w} = 2\,\alpha^{d}$.

3.2.4 Heat Transfer

In SMPP, to simulate heat transfer in a snowpack, the non-steady state two-dimensional heat conduction equation is solved following *Albert and McGilvary* (1992) with the addition of a source term:

$$\left(\rho C_{\mathrm{p}}\right)_{\mathrm{s}} \frac{\partial T}{\partial t} = \nabla.\left(\kappa_{\mathrm{s}} \nabla T\right) + L_{\mathrm{f}} \rho_{\mathrm{w}} S_{\mathrm{S}} \tag{3.18}$$

such that $\left(\rho C_{\mathrm{p}}\right)_{\mathrm{s}} = \left(\rho_{\mathrm{a}} \theta_{\mathrm{a}} C_{\mathrm{p,a}}\right) + \left(\rho_{\mathrm{w}} \theta_{\mathrm{w}} C_{\mathrm{p,w}}\right) + \left(\rho_{\mathrm{i}} \theta_{\mathrm{i}} C_{\mathrm{p,i}}\right)$

and $\kappa_{\mathrm{s}} = \kappa_{\mathrm{eff}}(1 - \theta_{\mathrm{w}}) + \kappa_{\mathrm{w}} \theta_{\mathrm{w}}$

where T is the temperature of a snow layer [K], ρ is the density [kg m^{-3}], C_{p} is the specific heat capacity [J (kg K)$^{-1}$], and θ_k is the fractional volumetric content of the phase.k The subscripts a, w, and i represent each component of the snowpack: air, water, and ice, respectively.

The term $L_{\mathrm{f}} \rho_{\mathrm{w}} S_{\mathrm{S}}$ is a source term representing latent heat release during refreezing of liquid water. The effective thermal conductivity (κ_{eff}) was calculated following *Calonne et al.* (2011), who conducted three-dimensional numerical computations of snow thermal conductivity through the air and ice phases. They developed an empirical relationship between thermal conductivity and dry snow density (Eq. 3.19). The term $\theta_{\mathrm{w}}\, \kappa_{\mathrm{w}}$ accounts for the effect of liquid water within the pores on the heat transfer.

$$\kappa_{\mathrm{eff}} = 2.5\mathrm{e}^{-6}\, \rho_{\mathrm{ds}}^{2} - 1.23\mathrm{e}^{-4} \rho_{\mathrm{ds}} + 0.024. \tag{3.19}$$

2.2.5 Refreezing of Liquid Water

During infiltration of liquid water in an initially subfreezing snowpack, heat transfer occurs between the liquid and solid phases during phase change. *Illangasekare et al.* (1990) developed a theory to describe the refreezing of meltwater in a cold snowpack. They expressed the maximum mass of liquid water per unit volume of snow (m_{max}) that must freeze to raise the snow temperature to zero as,

$$L_{\mathrm{f}} m_{\max} = -(\rho C_{\mathrm{p}})_{\mathrm{s}}\, T \tag{3.20}$$

The actual mass of liquid water per unit volume of snow that refreezes during a numerical time step (m_{f}) is always less than or equal to $m_{\max}$. It is limited by the available liquid water content in the snow layer. The variable S_{S} in Eq. 3.2 and Eq. 3.18 is related to m_{f} by:

$$S_{\mathrm{S}} = \frac{m_{\mathrm{f}}}{\rho_{\mathrm{w}} \Delta t} \tag{3.21}$$

where Δt is a numerical time step [s].

The change of liquid water content and snow layer temperature at the end of a numerical time step ($t + \Delta t$) caused by refreezing are solved through the Eq. 3.2 and Eq. 3.18, respectively, using the value of S_{S} from Eq. 3.21. At the end of the same time step, snow porosity (ϕ), air content (θ_{a}), and bulk density of snow (ρ_{s}) are updated as:

$$\phi^{t+\Delta t} = \phi^{t} - \frac{m_{\mathrm{f}}}{\rho_{\mathrm{i}}} \tag{3.22}$$

$$\theta_{\mathrm{a}}^{t+\Delta t} = \phi^{t+\Delta t} - \theta_{\mathrm{w}}^{t+\Delta t} \tag{3.23}$$

$$\rho_{\mathrm{s}}^{t+\Delta t} = (1 - \phi^{t+\Delta t})\rho_{\mathrm{i}} + \theta_{\mathrm{w}}^{t+\Delta t}\, \rho_{\mathrm{w}} + \theta_{\mathrm{a}}^{t+\Delta t}\, \rho_{\mathrm{a}} \tag{3.24}$$

3.3 Numerical Model Implementation

To solve the partial differential equations (Eq. 3.2 and 3.18) in SMPP, an explicit finite volume scheme was applied using a quadrilateral structured mesh. The mesh was first scaled to that of the key snowpack structures, e.g. the vertical grid size was at most 1 cm when ice layers were simulated as this corresponds to their typical thickness (*Watts et al.*, 2016) and the horizontal grid size was at most 1 cm wide when PFP were simulated, as they have been reported with diameters of between 0.5 and 2 cm (*Waldner et al.*, 2004). The mesh was then refined from iterative initial simulations to determine the optimum grid size that allowed numerical convergence of the partial differential equations. The optimum grid size was chosen so that the tolerance of the computational error between the total outflow (outflow when the snowpack has completely melted) and the initial snow water equivalent of the snowpack was less than 1 %. This numerical method considered each numerical cell as a control volume, in which the conservation equations were solved. Such an

approach is commonly applied in computational fluid dynamics (CFD) models as it is inherently conservative. To assure model stability, an adaptive time step with a maximum value of 1 s was computed so that the Courant-Friedrichs-Lewy conditions for the two-dimensional heat conduction equation and Richards equation were both met (*Haverkamp et al.*, 1977; *El-Kadi and Ling*, 1993). The time step decreased with increasing snow density, water content and temperature gradient. To prevent very small time steps, resulting in simulations taking weeks to finish, a lower bound of 10^{-4} s was chosen for the variable time step. In a few cases, however, using a lower bound for the time step resulted in estimated water contents greater than saturation at the interface of wet to dry snow; when this occurred, liquid water content exceeding saturation was restricted to saturation and the excess was added to the lower numerical cell. Each individual simulation run for this study took less than 72 h on an Intel Core I7-3610QM CPU.

To confirm mass conservation when mass flow was coupled with both freezing and thawing phase changes, the ratio of the sum of the mass fluxes at the boundaries of the domain and the sum of the water and ice content changes was calculated as

$$MC^{t_0} = \frac{\sum_{i,j}\left(\theta_{\mathrm{w}}^{t_0} + \frac{m_{\mathrm{f}}^{t_0}}{\rho_{\mathrm{w}}}\right)_{i,j} Vol_{i,j}^{t_0}}{\sum_{t=0}^{t_0}\left(\sum_{x\in\delta\Omega} \text{Mass Flux}\,(x,t) * \Delta t\right)} \tag{3.25}$$

where MC^{t_0} is a coefficient that is equal to 1 if mass conservation is respected at time t_0, $\Sigma_{i,j}$ is the sum over all the numerical cells that compose the snowpack, $Vol_{i,j}$ is the volume of the numerical cell (i,j) [m^3], Δt is the numerical time step [s], and the denominator represents the sum over time of the net mass fluxes [m^3 s^{-1}] at the boundary of the domain ($\delta\Omega$).

3.3.1 Boundary and Initial Conditions

Neumann boundary conditions were applied at the upper, right and left-hand boundaries for the mass and heat equations. A constant heat flux (Q_{n} in Eq. 3.1a and 3.1b) was applied as an upper boundary condition for the heat equation. This flux was then used to estimate the snowmelt rate utilized as the upper boundary condition for the mass flow equation (Q_{inf} in Eq. 3.1b). A rain influx can also be chosen as an upper boundary condition for the mass flow equation, permitting rain-on-snow simulations. Different boundary conditions can be set at the lateral boundaries: both as no-flow boundaries or periodic conditions. A constant heat flux or constant temperature is chosen at

the lower boundary. At the bottom, a free drainage boundary condition is specified for the water flow equation. The initial conditions used in the model included the snowpack slope angle, layering system and mean layer properties - porosity, water content, grain size, and temperature.

3.3.2 Model Assumptions

Water and energy flows within a layered, subfreezing snowpack are complex physical processes. The current lack of understanding of the physics of these processes necessitated assumptions while developing SMPP.

1. There is thermal equilibrium between the solid and liquid phases.
2. Freezing point depression effects on the snow grains from pore pressures are small and can be neglected.
3. The water entry pressure for dry snow can be characterized solely as a function of snow grain size.
4. The irreducible water content does not vary substantially and can be assumed constant for the whole snowpack.
5. The flow of water through the matrix and PFP is laminar.

In the present version of the model, some approximations were also made for simplification.

6. The change of grain size due to water vapour gradients (kinematic and equilibrium growth metamorphisms) or the presence of liquid water during the water flow event (wet snow metamorphism) was not considered.
7. Thermal convection, condensation, and sublimation within the snowpack are small during the melt event and need not be considered.
8. Temperature, density, and water content can be computed at the centre point of each numerical cell and assumed homogeneous within the cell.
9. The hydraulic and thermal conductivities at the interface of two numerical cells can be estimated using the arithmetic average of the values.

The uncertainties associated with these approximations will be addressed in a future version of the model.

3.3.3 PDE Solver Verification

To validate the solvers for the two partial differential equations (Eq. 3.2 and 3.18) in SMPP, their solutions were compared to those of two existing models that have been widely applied and validated in separate studies (Hydrus: *Šimunek et al.*, 2012; OpenFoam with *laplacianFoam*: *Logie et al.*, 2015).

Simulations of one-dimensional water flow through unsaturated porous media using Richards equation with SMPP were compared to that from the soil model Hydrus-1D (*Šimunek et al.*, 2008). The flow through a 1 m deep unsaturated sand column was simulated with both SMPP and Hydrus-1D. To maintain simplicity, a single WRC was considered for both wetting and draining processes and the soil hydraulic parameters were chosen from the soil catalogue offered with the model Hydrus. Water content was initialized at 0.05 m^{-3} m^{-3} in the whole system, a constant mass flux of 100 mm d^{-1} was imposed at the upper boundary, free drainage boundary condition was chosen for the lower boundary condition, and the lateral boundaries were set as no-flow. The simulations were run until steady-state conditions were achieved. Figure 3.2a compares the outputs from SMPP against the outputs from Hydrus 1D at three different times. The water flow simulation of SMPP agreed with the 1D simulation from Hydrus, suggesting that SMPP will be adequate for water flow simulations through snow using Richards equation. The difference is on the order expected from the different numerical methods used to discretize the equations in Hydrus 1D and SMPP.

The 1D heat conduction simulation was validated against the CFD model OpenFOAM, using the solver *laplacianFoam* with an explicit finite volume scheme. Heat conduction was calculated for a homogeneous snowpack of density 350 kg m^{-3} with a grain size of 1 mm. Constant temperatures set to -15^{o}C and 0^{o}C were specified at the upper and lower boundaries, respectively, and the snowpack temperature was uniform at -10^{o}C. Figure 3.2b shows the temperature distribution simulated by SMPP against the results from OpenFOAM at three different times. The heat transport simulated by SMPP is nearly identical to the CFD model, suggesting SMPP will be adequate for heat flow simulations.

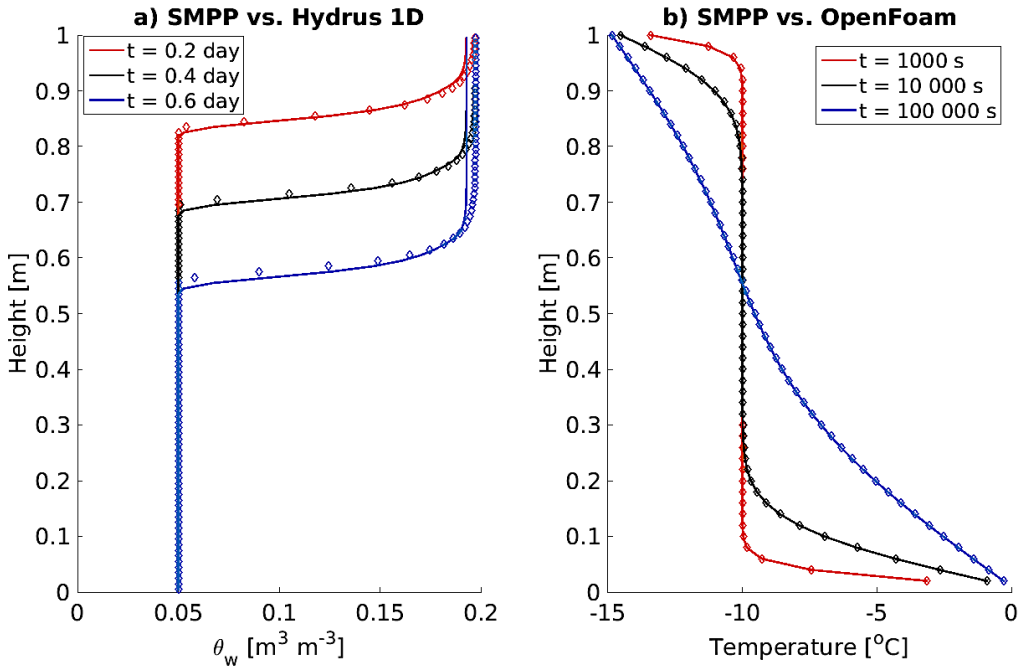

Figure 3.2 a) Comparison of water content distributions at three different times simulated by SMPP (represented with the dots) and by the soil model Hydrus 1D (represented with the lines). **b**) Comparison of temperature distributions at three different times estimated by SMPP (represented with the dots) and by the CFD model "OpenFOAM" (represented by the lines).

3.4 Water Flow Simulation in a Layered Snowpack

3.4.1 Flat and Sloping Melting Snowpacks

The melt of a fine over coarse layered isothermal snowpack (FC snow) was simulated. Table 3.1 summarizes the model parameters and snow properties used in all the numerical simulations. These snow properties were taken from experiment 1 of *Waldner et al.* (2004). For each snow layer, average grain size and density were perturbed cell by cell by Gaussian random fluctuations of 10 % and 1.5 %, respectively. The fluctuations were generated using the Box-Muller method (*Box and Muller*, 1958). This fluctuation in grain size was initially chosen to allow for relatively short simulation times, as increasing the grain size resulted in an increase of simulation time; the effect of this parameter on model flow outputs is presented in Section 3.6. The density fluctuation is about the same as the measured density variation (between 1.48 and 1.66 %) by *Waldner et al.* (2004). A heat flux of 150 W m^{-2} was applied at the snow surface as in the experiment of *Waldner et al.* (2004), a free drainage boundary condition was chosen at the bottom, and no-flow conditions at the lateral boundaries. A constant temperature of 0^{o}C was considered at the bottom boundary.

Table 3.1 Initial conditions, inputs and parameters used for the simulations in Sections 3.4, 3.6, and 3.7.

Parameters	Initial setting
Heat flux [W m^{-2}]*	150
Lateral length [m]*	0.35
Depth [m]*	0.25
Upper layer dry density [kg m^{-3}]* (fine)	540
Upper layer grain size [mm]* (fine)	1.5
Upper layer thickness [m]* (coarse)	0.10
Lower layer dry density [kg m^{-3}]* (coarse)	480
Lower layer grain size [mm]*	2.5
Lower layer thickness [m]*	0.15
Initial snow internal temperature [^{o}C]	0
Initial snow surface temperature [^{o}C]	0
Irreducible water content [m^3 m^{-3}]	0.024
Slope angle [^{o}]	0
Fluctuation in grain size	20 %
Fluctuation in density	1.5 %
Number of horizontal cells	70
Number of vertical cells	25
γ	2
Temperature at soil-snow interface [^{o}C]	0

* Taken from *Waldner et al.* (2004)

Figure 3.3a shows the simulated liquid water content distribution within a level snowpack after 3 h of melt. Liquid water, generated from the ~10 mm of melt at the snow surface, accumulated at the layer interface due to higher capillary pressure in the upper layer and then percolated the lower

layer when and where vertical pressure head gradients became positive. Distinct PFP formed below the high saturation layer, whereas the flow was similar to matrix flow in the upper part of the snow sample. Figure 3.3b shows the melt of the same snowpack on a 10^{o} slope. Periodic lateral boundary conditions were assumed in this case. More liquid water accumulated at the layer interface as the vertical gravitational term in the Darcy-Buckingham equation (Eq. 3.3) is lower than that of a level snowpack; lateral flows occurred downhill within the snowpack, impacting the shape of the PFP.

Figures 3.3c and 3.3d show the melt of a coarse over fine layered snowpack (CF snow) for both flat and sloping (10^{o}) terrains, respectively. Each layer had the same snow structure properties as their respective layers in the previous simulation (presented in Fig. 3.3a). In contrast to the simulation shown in Fig. 3.3a, no accumulation of meltwater was observed at the interface of the two layers (Fig. 3.3c). Instead, liquid water directly percolated into the lower layer. Thick PFP formed in the upper layer and thinned as they propagated down the snow sample. The sloped CF snow (Fig. 3.3d) presented tilted PFP caused by lateral flow. These results are qualitatively similar to the conceptual model of Wankiewicz (1978).

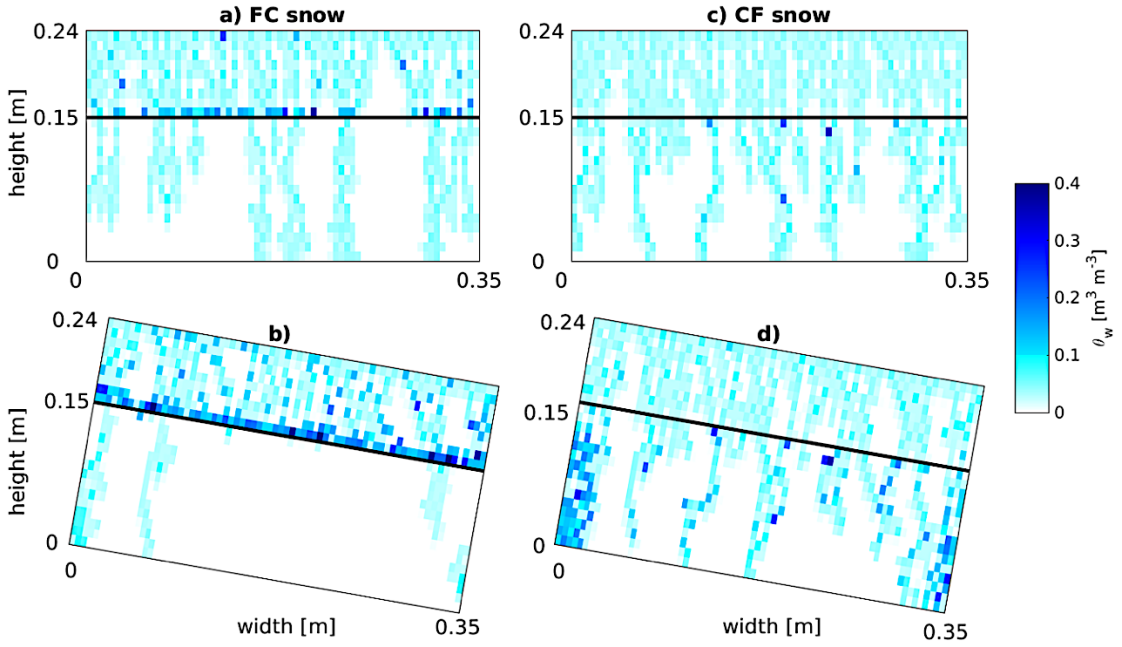

Figure 3.3 Modelled water content distributions after 3 h of melt using data from Waldner et al. (2004) on **a**), **b**) fine over coarse and **c**), **d**) coarse over fine snowpacks on **a**), **c**) level and b), d) sloping (10^o) sites. The horizontal black line represents the interface between the two textural layers.

3.4.2 Quantification of θ_w at Capillary Barriers and PFP Patterns

Simulated water flows through isothermal two-layer snow samples were compared to laboratory observations. Three snow samples were considered: fine over coarse snow (FC), fine over medium snow (FM) and medium over coarse snow (MC). The snow samples were initially dry at 0^{o}C prior to running the experiment. The input data for these simulations – snow density, grain size, and input flux - were presented in *Avanzi et al*. (2016). In their study, dyed liquid water at 0^{o}C was sprinkled over the surface of each snow sample. Vertical liquid water content distribution was measured at 2 cm resolution, as well as the fraction of wet area over total area (f) at the same resolution. Each snow sample was 20 cm high (composed of two snow layers of 10 cm each) and 5 cm wide, numerically discretized with a grid of 10x25 cells. A mass input flux of ~11 mm h^{-1} (c.f. FC1, FM1, and MC1 in *Avanzi et al.*, 2016) was applied at the upper boundary, free-drainage was specified at the lower boundary, and no-flow occurred at the lateral boundaries. As in the simulations presented in Section 3.4.1, γ was set to 2 as commonly assumed in soil studies and θ_{wr} was set to 0.024 m^3 m^{-3} (taken from Yamaguchi et al., 2010). Input mass flux was not applied

over the whole upper surface; instead, it was applied to a small fraction of the surface to match the *f* values observed at the surface of the snow samples by *Avanzi et al.* (2016). The optical grain size and density in each numerical cell were varied around the mean layer properties measured during the experiment. This was a necessary condition to simulate the formation of preferential flow. However, the coefficients of variation of the grain size in each snow sample were not measured during the laboratory experiment. Therefore, three different simulations were run with different grain size coefficients of variation of 5 %, 10 %, and 20 %. The simulation results for each grain size fluctuation were compared to the observations to determine which coefficient of variations provided the best fit. During the experiment, the coefficients of variation of the snow density of each snow layer were observed to be 3 % and 6 % in the lower and upper snow layers, respectively (*Avanzi et al.*, 2016). These measured coefficients of variation of snow density were applied in the model to fluctuate the snow density within each numerical cell around the mean layer values.

A coefficient of variation of 10 % for the grain size gave best results of simulated liquid water and *f* distributions at the simulated arrival time of water at the snow base (time at which the observations were collected); thus, observed and simulated water distributions within the three snow samples for a grain size fluctuation of 10 % are presented in Fig. 3.4 (upper graphs). For FC and FM snow samples, the simulated arrival times of water at the snow base were underestimated by 24 % and 30 %, respectively, while it was over-estimated by 25 % for the MC snow sample. In all snow samples, observed liquid water distribution was well approximated by the model. Ponding of liquid water was both observed and simulated at the interface of the stratigraphic layers. More liquid water content accumulated at the interface of FC snow than in the other snow samples, due to a higher suction gradient at this layer interface. In MC, the model under-predicted θ_w at the interface, while θ_w was over-predicted in FC.

Simulated f values in the snow samples were compared to observations for a grain size fluctuation of 10% (Fig. 3.4, lower graphs). Simulated values follow the trend of the observation; *f* increased (PFP thickened) above the interface and decreased below it (PFP thinned). Fully wet layers were observed and simulated at the layer interfaces ($f = 1$) in FC and FM. In MC, *f* was over-estimated in the whole snow sample.

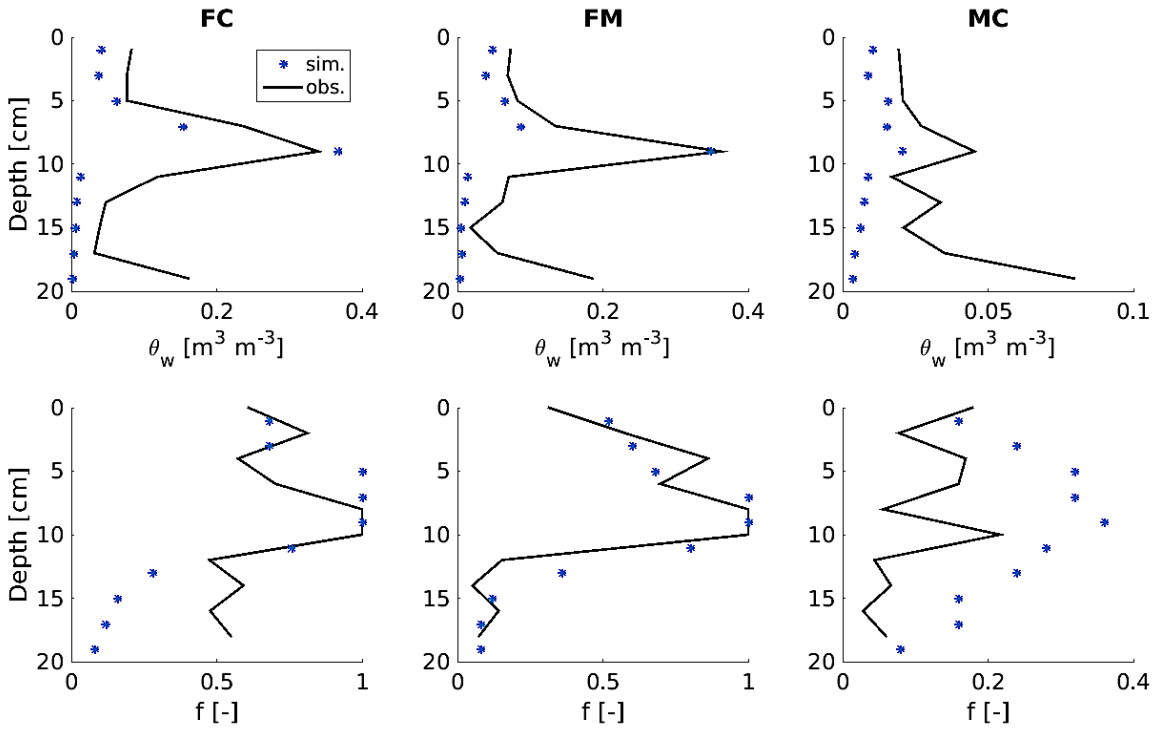

Figure 3.4 Simulated and observed liquid water content and fraction of wet surface area (upper and lower graphs, respectively). The three snow samples representing fine over coarse (FC), fine over medium (FM) and medium over coarse (MC) layers from *Avanzi et al.* (2016) were used with an input flux of ~ 11 mm/h. The black lines (*obs.*) represent the observed experimental values and dots (*sim.*) are the simulation results.

3.5 Comparison between Observed and Simulated Capillary Pressures

The impact of γ (Eq. 3.8) on the capillary pressure within a wetting snowpack was studied by simulating the capillary pressure measurements of *Katsushima et al.* (2013). Water flow through Katsushima's three snow samples with different physical properties (SLL, SL and SM, c.f. *Katsushima et al. 2013* for details) were modelled, applying a constant water flux of ~20 mm h^{-1} at the surface. The snow samples (5x27 cm) were initially dry except for the upper 2 cm in which the water content was initialized at θ_{wr}, chosen equal to 0.024 m^3 m^{-3} as in *Hirashima et al.* (2014a). The snow samples were discretized with a grid of 15x27 cells and the lateral and bottom boundaries were set to impermeable walls and free-flow, respectively. A fluctuation with a standard deviation of 20 % was applied to the average grain size of each snow sample (*Katsushima et al.*, 2013). *Hirashima et al.* (2014a) found best results for this value and showed that fluctuations

in snow density had negligible effect on their model results. Thus, in all simulations presented in this section, density was not varied cell by cell.

Figure 3.5 shows three different model outputs at the wet to dry snow interface (2 cm below the surface) for the three snow samples SLL, SL, and SM (columns in Fig. 3.5, from left to right, respectively). The three model outputs studied are the minimum suction, the time of minimum suction, and the capillary pressure at steady state (rows in Fig. 3.5, from top to bottom, respectively). In each graph, the outputs (dots in Fig. 3.5, corresponding to mean simulated values) are compared to measured values from *Katsushima et al.* (2013) (black lines) for varying values of $\gamma \in [1.5, 2.5]$. The minimum pressure observed by *Katsushima et al.* (2013) corresponds to the threshold of capillary pressure at which water started percolating dry snow. As γ increased, simulated suctions in wetting cells decreased, resulting in lower simulated values of minimum pressure and time of minimum pressure (upper and middle rows in Fig. 3.5). An optimum value of γ for which simulated pressure at the interface matched observed pressure for the three snow samples cannot be found; however, a value of 2.5 for the snow sample SLL and SL and a value of 1.9 for SM provided a best match for the pressure at steady state. Pressure at steady state is always under-estimated for the SL sample and over-predicted for SLL and SM snow samples. On average, values of γ greater than 2.0 better approximated the minimum pressure at the interface for all snow samples. Figure 3.6 illustrates the difference between simulated and observed average capillary pressures at the wet to dry snow interface through time for γ equal to 2.5 for the samples SLL and SL and equal to 1.9 for the sample SM.

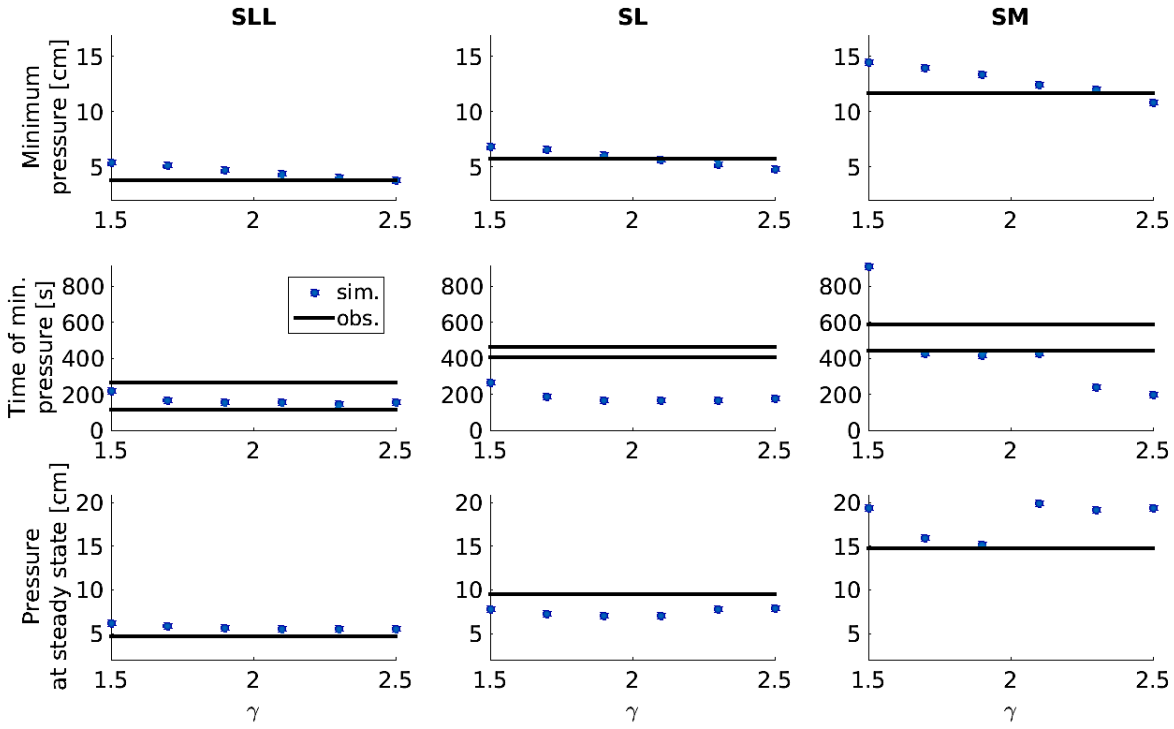

Figure 3.5 Sensitivity analysis of the γ on minimum pressure, time at which minimum pressure is reached and the pressure at steady state. The three snow samples representing coarse (SLL), medium (SL) and fine (SM) grains from *Katsushima et al.* (2013) were used with an input flux of ~20 mm/h. The black lines (*obs.*) represent the observed experimental values (2 black lines are plotted for the time of minimum pressure to represent the lower and upper bounds). The dots (*sim.*) represent the mean simulated values at the wet to dry snow interface.

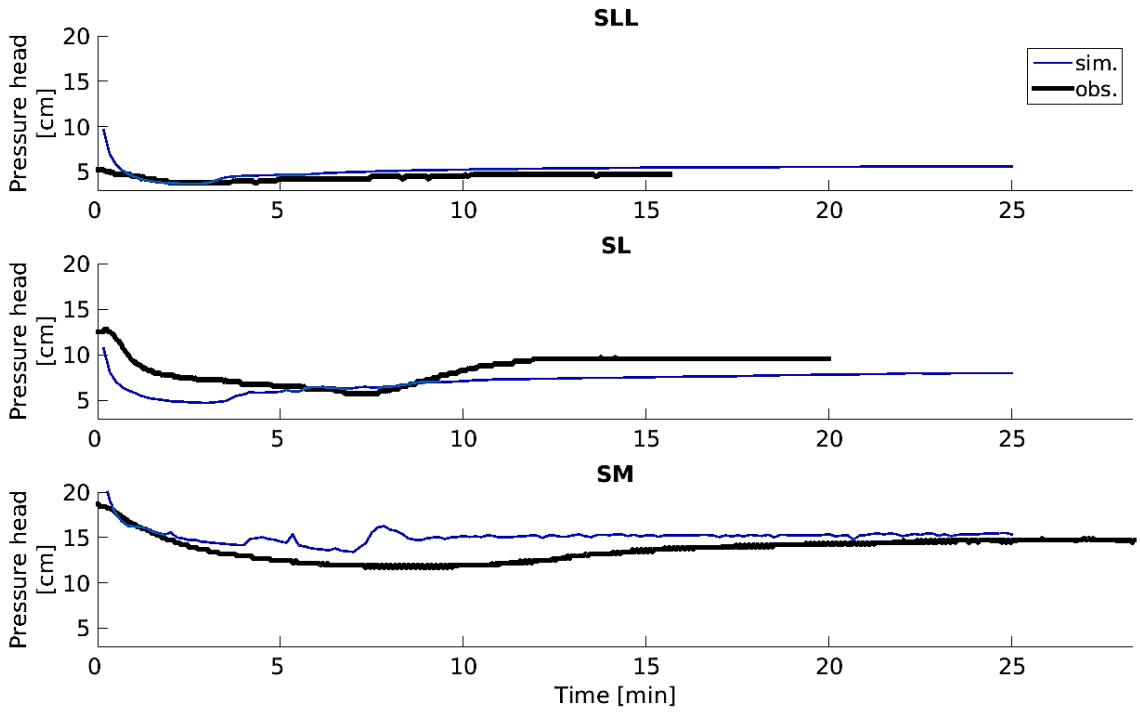

Figure 3.6 Capillary pressure at the wet to dry snow interface in the snow samples SLL (a), SL (b) and SM (c), with a water flux of 20 mm h^{-1} at the surface and a single γ value of 2.5 (SLL and SL) and 1.9 (SM). The black line (*obs.*) represents the pressure measured by *Katsushima et al.* (2013) and the blue lines (*sim.*) are the simulated pressures at the interface.

3.6 Uncertainty Analysis on Model Variables and Inputs.

The FC snowpack of *Waldner et al.* (2004) was used as a reference case for the sensitivity analysis with perturbed density and grain size as in Section 3.4.1. The parameters and model inputs used in the reference case are summarized in Table 3.1. Irreducible water content, fluctuations in grain size and density, γ, and the three different models to estimate the van Genuchten's parameters for the boundary drying curve (α^d and n^d) are available in the snow literature (*Daanen and Nieber,* 2009; *Yamaguchi et al.,* 2010, 2012) were individually varied. Differing values of θ_{wr} have been found in snow, ranging from 0.018 to 0.04 m^3 m^{-3} (*Katsushima et al.*, 2013; *Yamaguchi et al.*, 2010). In the sensitivity analysis, this parameter was varied between 0.01 and 0.04 m^3 m^{-3} with a constant step of 0.005. The fluctuations applied to grain size and density were varied between 0 and 20 % as in *Hirashima et al.* (2014a), with a constant step of 2 %. Finally, γ was varied between 1.5 and 2.5 with a constant step of 0.2. Their impacts on total outflow and wet surface area per total area (*f*) in the lower layer (below the layer interface) after 3 h of melt, the maximum liquid

water content in the snowpack during melt and the time at which liquid water first reached the base of the snowpack were observed.

Figure 3.7 shows the results of the sensitivity analysis. Higher values of θ_{wr} increased the time at which meltwater reached the base of the snowpack as more liquid water was held by capillary forces within the pores. Therefore, lower outflows were observed for greater values. As θ_{wr} increased, the wet surface area in the lower layer greatly decreased (Fig. 3.7) and PFP became wetter (not shown).

Changes in the fluctuation applied to snow density had a lesser effect than varying the fluctuation in grain size. Higher fluctuations in grain size induced larger capillary pressure heterogeneities between two adjacent numerical cells, resulting in more liquid water content accumulating in the snowpack. f values in the lower layer increased with the fluctuation from 0 to 6% and then decreased from 6 to 20 %. Figure 3.8 shows the distribution of liquid water after three hours of melt within the FC snow for increasing grain size fluctuations, the total wet surface area in the lower layer was the sum of the surface area of each PFP and thus depended on their dimensions. At a zero grain size fluctuation, only matrix flow was simulated. As this fluctuation increased, PFP became slightly wetter but fewer PFP formed. This is caused by shorter sections (in lateral length) of the high saturation layers present at the layer interface due to a shift in the flow regime in the upper layer from matrix flow to thinner and wetter PFP. This change in the lateral length of the wet sections at the layer interface drove the number of PFP forming in the lower layer. More water content accumulated at the interface with increasing grain size fluctuations, causing a delay in water percolating the lower layer and shorter PFP. This combined effect of shorter and fewer PFP gave the results shown in Fig. 3.7.

This is the first study of snowpack water flow that has applied a boundary wetting curve, which was scaled from the boundary drying curve through γ. As shown in Fig. 3.7, this parameter impacted all model outputs. A larger value resulted in lower suction computed during the wetting process. Therefore, the condition for which liquid water flows from wet to dry cells (downward vertical water pressure becomes positive) was satisfied at lower water contents in the wetting cell; the maximum liquid water content in the snowpack thus decreased with increasing values of γ during the melt period. As this parameter increased, f values in the lower layer also increased.

As seen in Fig. 3.7, the three different models used to estimate the van Genuchten's parameters for the boundary drying curve gave substantially different results. The model of *Daanen and Nieber* (2009) did not allow for PFP formation. The suction estimated with Daanen and Nieber's model is lower than the two models of *Yamaguchi et al.* (2010, 2012). Therefore, little liquid water ponded at the interface of wet to dry cells before percolating into the dry layer, resulting in a quasi-uniform wetting front and thus, matrix flow. Even though the model outputs from *Yamaguchi et al.* (2010) were different from those of *Yamaguchi et al.* (2012) (reference case), the former still allowed for PFP formation. The older model resulted in more liquid water content accumulating in the snowpack, resulting in higher computed hydraulic conductivities and therefore, a higher outflow after 3 h of melt.

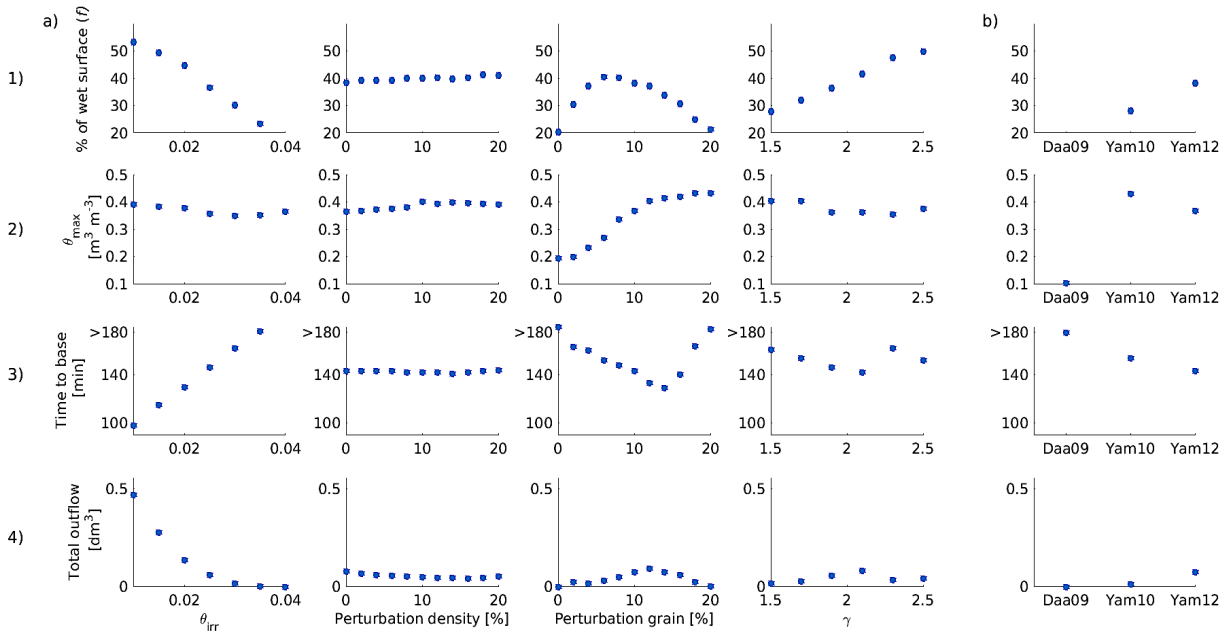

Figure 3.7 a) Sensitivity analysis of different model variables on total outflow after 3 h of melt (4), the time at which meltwater reaches the base of the snowpack (3), the maximum liquid water content simulated within the melt period (2) and the percentage of wet surface area in the lower layer at 3 h of melt (1). **b**) Comparisons of 1, 2, 3, and 4 with the models of *Daanen and Nieber* (2009) (Daa09), *Yamaguchi et al.* (2010) (Yam10) and *Yamaguchi et al.* (2012) (Yam12) to estimate the parameters of the boundary drying curve (α^d, n^d).

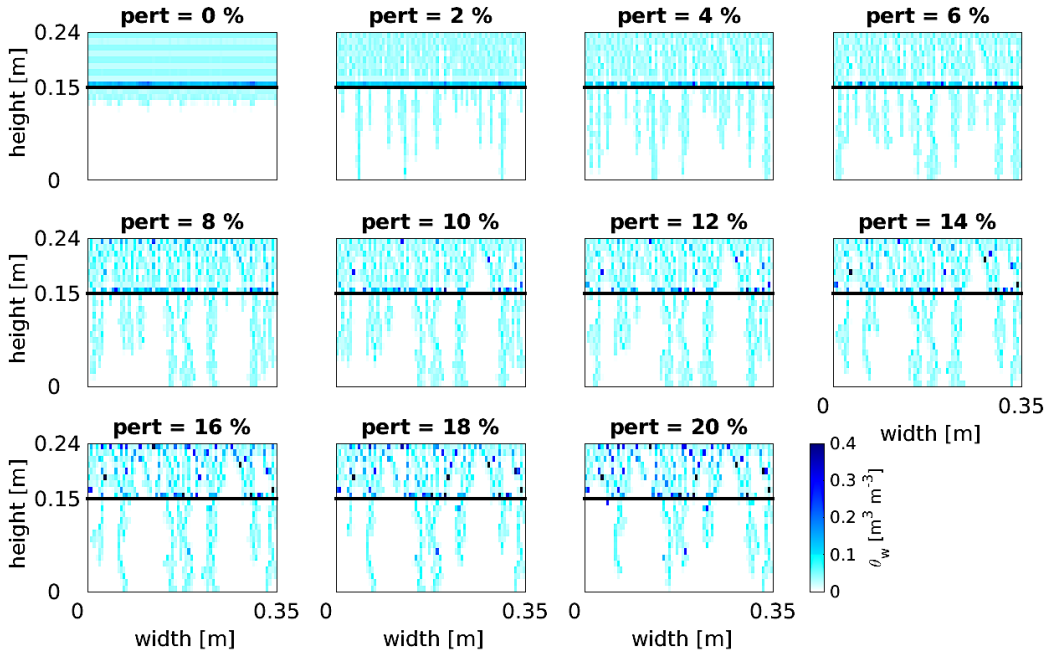

Figure 3.8 Water distribution after 3 h of melt within the FC snow sample for increasing fluctuations in grain size.

3.7 Ice Layer Formation in Subfreezing Snow

The FC snowpack of *Waldner et al.* (2004) was also used to demonstrate the ability of the model to simulate ice layer formation in subfreezing snow. As in Section 3.4.1, a constant heat flux of 150 W m^{-2} was applied at the snow surface to generate melt for ~2.5 hrs, then the flux was set to zero and the model was allowed to run for another ~6 hrs. In contrast to Section 3.4.1, the snow temperature was initially below freezing: the upper layer temperature was set to -3^{o}C and the lower temperature to -5^{o}C. A zero heat flux was specified at the lower and lateral boundaries.

Figure 3.9 shows the water content, dry density and temperature distributions within the FC snowpack (upper to lower rows, respectively) at four different times (left to right columns). At the end of the melting period (~2.5 hrs), the snowpack melted by ~10 mm and the meltwater generated at the surface accumulated at the layer interface. The snow temperature in the upper wet layer rose to 0^{o}C, while areas of dry, cold snow remained at the layer interface. The lower layer stayed below freezing. After the melting period, liquid water in the upper layer kept percolating downward for a short period due to gravity. The snowpack slowly became isothermal and the snow surrounding the layer interface gained latent heat due to refreezing of liquid water at the interface, resulting in

an increase of temperature in the lower layer. The more liquid water that refroze, the higher the increase in dry density. After refreezing of the high water content layer above the interface, a large increase in dry density, from 650 to 850 kg m^{-3}, occurred as ice formed in the snowpack. The evolution of the liquid water content, dry density and temperature through time within the snowpack are shown in the video present in the Supplementary material.

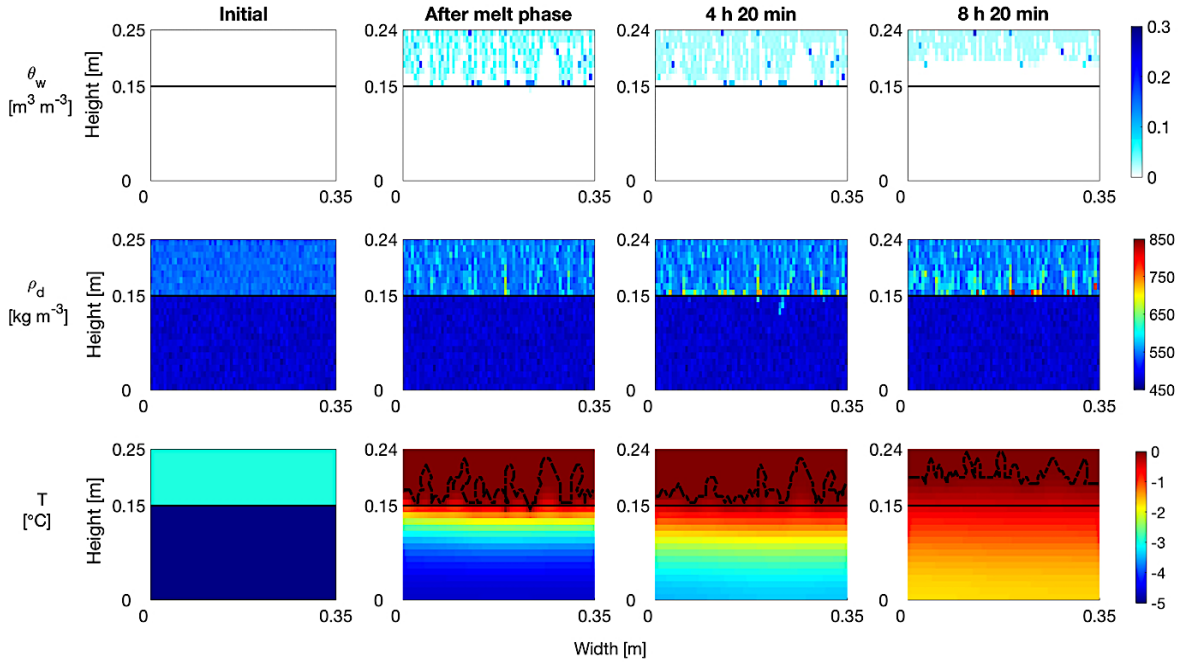

Figure 3.9 Water content, dry density and temperature distributions within the FC snowpack at 4 different times. At the beginning of the simulation (Initial), after the melt phase, and at two different times after melt was stopped (4 h 20 min and 8 h 20 min). The black dashline in the lower plots represents the isoline at 0°C.

3.8 Discussion

The SMPP model is qualitatively able to reproduce flow patterns that are observed in the field and laboratories (Fig. 3.3). The distribution of liquid water content and the distribution of the fraction of wet area over total area observed in snow samples during laboratory experiments were quantitatively reproduced (Fig. 3.4, lower graphs). *Waldner et al.* (2004) and *Avanzi et al.* (2016), amongst others, observed that the interface from fine to coarse snow layers acts as a capillary barrier, due to higher suction in the fine layer. This behavior was reproduced by SMPP (Fig. 3.3 and 3.4). Applying Richards equation to represent the ponding of liquid water at the interface of snow layers was essential, as previously noted (*Jordan*, 1995; *Hirashima et al.*, 2010). The size of

the simulated wet layers in the FC snow is comparable to the dimensions observed by *Waldner et al.* (2004) with widths varying between 1 and 5 cm. Simulated liquid water content at the high saturation layer were comparable to observations in three different snow samples (Fig. 3.4).

PFP were simulated by implementing a water entry pressure and heterogeneities in snow properties, as in *Hirashima et al.* (2014a). In accordance with *Hirashima et al.* (2014a), the implementation of a water entry pressure for dry snow was necessary for the formation of PFP. Distinct PFP originated at the layer interface in the two cases considered in Section 3.4.1, i.e. in FC and CF snow samples; thus, the snow properties above and below the interface were not a factor in the formation of PFP. *Marsh and Woo* (1984a) also observed PFP forming at either flow accelerating interface (e.g. CF snow) or flow impeding interface (e.g. FC snow). Similarly, the thicknesses of simulated PFP in Fig. 3.3, ranging from 0.5 to 3 cm are identical to those observed in the laboratory (*Waldner et al.*, 2004) and in the field (*Marsh and Woo*, 1984a). Greater values of γ resulted in wetter, thicker and more connected PFP (Fig. 3.10), due to more lateral movement as the condition at which liquid water flowed from wet to dry snow occurred at lower water contents. The shape and number of PFP forming below an impeding interface was driven by the properties of the ponding layer, i.e. its liquid water content and lateral length. For further validation, the connectivity and shape of the simulated PFP can be compared to pictures of dye experiments in natural snowpacks, such as those collected by *Williams et al.* (2010). The fraction of wet surface area to total area (*f*) was compared to observed values in three snow samples (FC, FM, and MC, c.f. Fig. 3.4). Discrepancies were observed. First, it is important to state that this two-dimensional model is compared to three-dimensional data. These discrepancies may also originate from slight differences in the inputs used in the model and the laboratory experiments. During the laboratory experiments, a thin cotton ring was positioned at the upper boundary to spread the tracer over the surface (*Avanzi et al.*, 2016); however, dyed water percolated into the snow sample surfaces at preferential areas and was not uniform over the whole surface (*Avanzi et al., 2016*, Figure 1, upper row). This could have been caused by the formation of a thin capillary barrier between the cotton ring and the snow surface. In the model, the input flux was only applied at a few cells to try to match the observed *f* values at the snow surface by *Avanzi et al.* (2016). From the sensitivity analysis, wet surface area (i.e. PFP width and length) is greatly influenced by θ_{wr}, the fluctuation in grain size, and γ. Different results of *f* could therefore have been obtained for different combinations of parameters used in Sec. 3.4.2.

The sensitivity analysis showed that the model was more sensitive to fluctuations in grain size than fluctuations in dry density. This behavior is similar to model results from *Hirashima et al*. (2014a) who also noted that the wet surface area increased with the fluctuation in grain size, due to more lateral flow and therefore, wider PFP. The high sensitivity to grain size fluctuation is most likely because the water entry pressure of dry snow depends solely on this parameter. Further work should be carried to establish probability density functions or relationships for the spatial distribution of these parameters from field observations. After the formation of PFP lateral flows occurred at the high water content layer towards the PFP due to lateral pressure gradients, as previously modelled in soil by *Jury et al.* (2003).

Despite the disparity of values for θ_{wr} in the literature, few studies have quantified the impact of this parameter on water flow through snow (e.g. *Marsh and Woo*, 1984b; *Tseng et al.*, 1994b). This parameter had a significant impact on model results; increasing values of θ_{wr} resulted in slower flows as shown by increasing times at which liquid water reached the base of the snowpack (Fig. 3.7). This agrees with model results from *Marsh and Woo* (1984b). Increasing values of θ_{wr} also caused the formation of thinner and wetter PFP (not shown). No physical relationship exists to relate θ_{wr} to snow properties and further field or laboratory experiments should be conducted to establish this.

Hirashima et al. (2014a) applied the boundary drying curve of *Yamaguchi et al.* (2012) to represent the suction in wetting snow samples and modelled a jump of pressure between the water entry pressure value to the boundary drying curve when θ_{w} became greater than θ_{wr}. The simulation results by *Hirashima et al.* (2014a) for the SM and SL snow samples with an input flux of 20 mm h^{-1} poorly reproduced the observed values of minimum pressure. In *Hirashima et al.* (2014a), for the SLL snow sample, both simulated values of minimum pressure and pressure at steady state greatly differed from the observations. On the other hand, in SMPP, values of minimum pressure and pressure at steady were better represented in the three snow samples. This highlights the importance of including full capillary hysteresis on the suction within a wetting snowpack.

The formation of ice layers was successfully modelled. Three distinct zones were observed as in *Marsh and Woo* (1984a): wet, mixed wet-dry and dry zones. The wet zone above the matrix wetting front was at the freezing point temperature. The dry zone was located below the finger

wetting front and stayed below freezing. PFP were essential for liquid water to reach cold layers in the snowpack (*Humphrey et al.*, 2012) and to the creation of distinct wet and dry zones, composed of zones at 0°C and below 0°C. As hypothesized by *Marsh and Woo* (1984a) and *Marsh* (1991), ice layers formed at the wet-dry interface where the surrounding snow cold content was sufficient to refreeze the ponding water (*Pfeffer and Humphrey*, 1996; *Humphrey et al.* 2012). The refreezing resulted in an increase in temperature of the surrounding snow. The average density of the ice layers was ~725 kg m^{-3} (ranging from 650 to 850 kg m^{-3}). Comparing to observations by *Marsh and Woo* (1984a) and *Watts et al.* (2016), the former observed ice layers with densities ranging from 630 to 950 kg m^{-3} with a mean of 800 kg m^{-3} and thicknesses ranging from 1 to 40 mm; the latter measured ice layer densities, varying between 814 and 980 kg m^{-3}, with a mean value of 909 kg m^{-3}. The ice layer densities simulated by SMPP are therefore within the range of values observed in the field. The vertical resolution of the simulated ice layers depends on the vertical resolution chosen for the mesh. For different resolutions than the one used in Section 3.7, ice layers would still be expected to form, but their densities would differ as the amount of ponding liquid water would be different. For instance, for a lower vertical resolution than the one applied in Sec. 3.7, more liquid water content would accumulate at the two-layer interface to satisfy Eq. 3.10; after refreezing, the dry densities of the ice layers in the finer simulation would be higher than the modelled ice layer densities in Section 3.7.

The model required some approximations that still need to be tested, amongst which the impact of snow metamorphism is potentially important. Including wet and dry snow metamorphism would result in an increase of grain size within and around the PFP, which could make the simulation of the PFP more dynamic than shown here. For wet snow, it was also assumed that the freezing point of liquid water was 0°C. Studies in soil showed that pore pressure and salt content can lower the freezing temperature of liquid water in the pores (e.g. *Spaans and Baker*, 1996) and this is an important parameter in studies of frozen soils. *Daanen and Nieber* (2009) demonstrated that the freezing temperature of the liquid phase in snow can be lower than 0°C. Accounting for the freezing point depression in snow models would lower the rate of refreezing of liquid water.

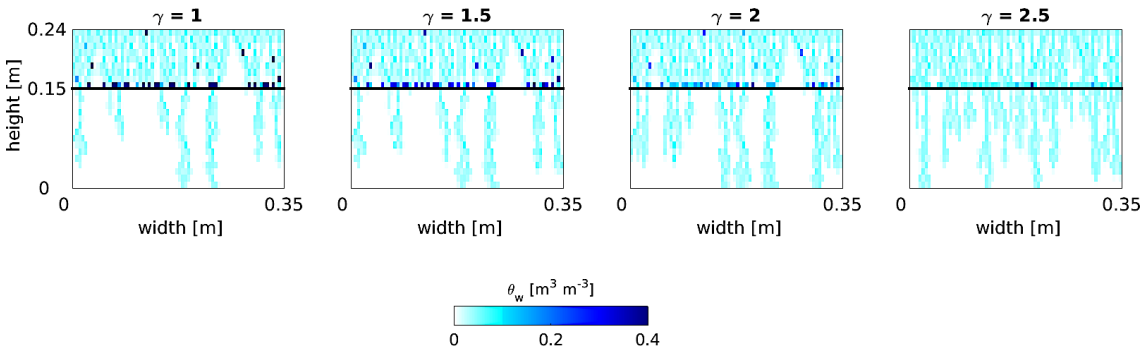

Figure 3.10 Modelled water content distribution within the FC snowpack after 3 h of melt for four different values of γ: 1 (no hysteresis), 1.5, 2 and 2.5.

3.9 Conclusions

A 2D snowmelt model that can simulate the formation of PFP from unstable wetting fronts generated by heterogeneities in snow properties was presented. For the first time, capillary hysteresis was included in a snowpack water flow model. To develop an equation for the water entry suction, *Katsushima et al.* (2013) used four artificial snow samples with densities greater than 387 kg m^{-3} and input water rates greater than 22 mm hr^{-1}, and so there is great uncertainty in the application of this equation for lower densities and lower input fluxes. PFP formed at different layer interfaces (FC and CF snow), showing that PFP formation does not depend on the snow properties on either side of the interface. In the case where liquid water ponded at a FC layer interface, PFP patterns depended on the characteristics (lateral length and water content) of the layer of ponded water. During meltwater percolation into a subfreezing snowpack, liquid water ponding at the interface of two snow layers or at the base of the snowpack prior to the arrival of the matrix wetting front refroze, forming ice layers.

Wetting fronts became unstable from lateral fluctuations in snow properties; however, such fluctuations cannot be directly implemented in one-dimensional snow models. Even though *Wever et al.* (2016) divided flow through snow between matrix flow and preferential flow in the 1D model SNOWPACK using a dual domain approach, their approach needed two calibration coefficients to simplify the representation of physical processes. A more physical approach, such as the one presented here, can enhance the understanding of the physical processes that drive the formation of PFP, and then could be used to parameterize 1D snow models. For instance, this model could

help better estimate the exchange of meltwater between the matrix and preferential flow domains in the dual domain model of *Wever et al.* (2016).

Accounting for the full capillary hysteresis improved the simulation of capillary suction at the wet to dry snow interface for wetting snow when compared to results from *Hirashima et al.* (2014a), in which only a drying boundary curve was used. A sensitivity analysis showed that capillary hysteresis also influenced preferential flow formation, snowpack runoff, and water retention. The scanning curves were estimated from the boundary wetting and drying curves, which were scaled from each other based on the ratio of the van Genuchten parameter α of each curve (*Kool and Parker*, 1987). An optimum value for this ratio could not be determined here, but values greater than 2.0 gave best results. It is expected that this parameter depends on snowpack physical properties and further studies, such as the one conducted by *Adachi et al.* (2012), are needed. Experimental determination of hysteresis effects in snow is challenging, as the ice matrix (in contrast to soil matrix) undergoes metamorphism in the presence of liquid water. This makes the separation of the difference in water retention in wetting and drying mode from temporal effects by snow metamorphism complicated. Other models to compute scanning curves and the wetting boundary curve exist (e.g. *Mualem*, 1974, 1984) and could be implemented to further examine the results shown in this study.

In hydrological models or land surface schemes that divide the snowpack into 1 or 2 snow layers, it is assumed that a snowpack must be isothermal and wetted before discharge from the snowpack occurs. This assumption is erroneous as meltwater flows through PFP, bypassing dry zones of the snowpack. A snowpack does not have to be isothermal for melt to start, only the near-surface layer must reach 0^{o}C. Then, meltwater will penetrate deeper snowpack layers and gradually warm the snowpack to the freezing point as suggested by *Pomeroy et al*. (1998).

Although the model components presented here are based on verified theories, they have never been coupled in a numerical framework before. Further fieldwork is required to validate this model against detailed in-situ data; however, the model supports a qualitative field description of how PFP are formed (e.g. *Marsh and Woo*, 1984a). The development of this numerical model suggests the following questions on water flow through snow and numerical snow modelling to be considered in future:

- How do snowpack physical properties control the irreducible water content?
- How can grain size and density spatial fluctuations be better represented?
- Can the water entry pressure for dry snow be related to snow density?
- Is the thermodynamics equilibrium assumption suitable or can liquid water flow through subfreezing snow layers without completely refreezing (Illangasekare et al., 1990)?
- Is the flow through preferential flow paths always laminar? Does Darcy's law always apply?
- Does liquid water refreeze at 0^{o}C in snowpacks or is there a freezing point depression that depends on snow properties, chemistry, and surface tension between ice and liquid water?
- Is convection between the wetting phase and the ice important for heat transfer within the melting snowpack?

Key Points for the Next Chapter

- How can a field study be prepared to validate this model against melt data from natural snowpacks?
- How does this model perform against natural snowmelt data?
- What are the limitations of this model?
- Only heat conduction is assumed here. What are the effects of considering heat convection on the snow internal temperature distribution?

3.10 References

Adachi, S., Yamaguchi, S., Ozeki, T., and K. Kose (2012), Hysteresis in the water retention curve of snow measured used an MRI system, *ISSW Proceedings 2012*, Anchorage, Alaska, 918-922.

Albert, M. and W. McGilvary (1992), Thermal effects due to air flow and vapor transport in dry snow, *Journal of Glaciology*, 38(129), 273–281.

Avanzi, F., Hirashima, H., Yamaguchi, S., Katsushima, T. and C. De Michele (2016), Observations of capillary barriers and preferential flow in layered snow during cold laboratory experiments*, The Cryosphere*, 10, 2013-2026, doi: 15194/tc-10-2013-2016.

Bear, J. (1972), Dynamics of fluids in porous media, New York: Elsevier.

Beven, K., and P. Germann (1981), Water flow in soil macropores. II: A combined flow model, *Journal of Soil Sci.*, 32, 15-29, doi: 11111/j.1365-2389.1981.tb01682.x.

Box, G., and M. Muller (1958), A note on the generation of random normal deviates, *Ann. Math. Stat*., 29(2), 610-611, doi:11214/aoms/1177706645.

Brun, E. (1989), Investigation on wet-snow metamorphism in respect of liquid-water content, *Annals of Glaciology*, 13.

Calonne, N., Flin, F., Morin, S., Lesaffre, B., Rolland du Roscoat, S., and C. Geindreau (2011), Numerical and experimental investigations of the effective thermal conductivity of snow, *Geophys. Res. Lett.*, 38, L23501, doi:11029/2011GL049234.

Calonne, N., Geindreau, C., Flin, F., Morin, S., Lesaffre, B., Rolland Du Roscoat, S., and P. Charrier (2012), 3-D image-based numerical computations of snow permeability: links to specific surface area, density, and microstructural anisotropy, *The Cryosphere*, 6, 939–951, doi: 15194/tc-6-939-2012.

Colbeck, S. (1972), A theory of water percolation in snow, *Journal of Glaciology*, 11(63), 369-385.

Colbeck, S. (1979), Water flow through heterogeneous snow, *Cold Regions Science technology*, 1, 37-45, doi:11016/0165-232X(79)90017-X.

Colbeck, S. and G. Davidson (1973), Water percolation through homogeneous snow, Proceedings, *the Role of Snow and Ice in Hydrology*, 4, 242–257.

Daanen, R. P., and J. L. Nieber (2009), Model for coupled liquid water flow and heat transport with phase change in a snowpack, *Journal of Cold Regions Engineering*, 23(2), 43–68, doi:11061/(ASCE)0887-381X(2009)23:2(43).

Dash, J.G., Fu, H., and J. S. Wettlaufer (1995), The premelting of ice and its environmental consequences, *Reports on Progress in Physics*, 58, 115-167.

Dash, J.G., Rempel, A. W., and J. S. Wettlaufer (2012), The physics of permelted ice and its geophysical consequences, *Reviews of Modern Physics*, 78 (3), 695-741, doi:11103/RevModPhys.78.695.

Davis, D., Horton, R., Heitman, J., and T. Ren (2009), Wettability and hysteresis effects on water sorption in relatively dry soil, *Soil Sci. Soc. of American Journal*, 73(6), doi:12136/sssaj2009.00028N.

DeBeer, C., and J. Pomeroy (2010), Simulation of the snowmelt runoff contribution area in a small alpine basin, *Hydrol. Earth Syst. Sci.*, 14, 1205-1219, doi: 15194/hess-14-1205-201

El-Kadi, A.I., and G. Ling (1993), The Courant and Peclet Criteria for numerical solution of the Richards equation, *Water Resources Research*, 29(10), 2485-2494, doi:11029/93WR00929.

Male, D.H. and D. M. Gray (1975), Problems in developing a physically based snowmelt model, *Canadian Journal of Civil Engineering*, 2(4), 474–488.

Haverkamp, R., Vauclin, M., Tourna, J., Wierenga, P.J. and G. Vauchaud (1977), A comparison of numerical simulation models for one-dimensional infiltration, *Soil Science Society America Journal*, 41, 285-294, doi:12136/sssaj1977.03615995004100020024x .

Hill, D.E. and J.-Y. Parlange (1972), Wetting front instability in layered soils, *Soils Science Society of America*, Proceedings, 36(5), 697-702.

Hillel, D. and R. Baker (1988), A descriptive theory of fingering during infiltration into layered soils, *Soil Science*, 146. 51-53.

Hirashima, H., Yamaguchi, S., and T. Katsushima (2014a), A multi-dimensional water transport model to reproduce preferential flow in the snowpack, *Cold Regions Science and Technology*, 108, 80-90, doi:11016/j.coldregions.2014.09.004.

Hirashima, H., Yamaguchi, S., and Y. Ishii (2014b), Simulation of liquid water infiltration into layered snowpacks using multi-dimensional water transport model, *ISSW Proceedings*, 48-54.

Hirashima, H., Yamaguchi, S., and Y. Ishii (2014c), Application of a multi-dimensional water transport model to reproduce the temporal change of runoff amount, *ISSW Proceedings*, 541-546.

Hirashima, H., Yamaguchi, S., Sato, A. and M. Lehning (2010), Numerical modeling of liquid water movement through layered snow based on new measurements of the water retention curve, *Cold Regions Science and Technology*, 64(2), 94-103, doi:11016/j.coldregions.20109.003.

Huang, H.C., Tan, Y.C. Liu, C.W., and C. H. Chen (2005), A novel hysteresis model in unsaturated soil, *Hydrological Processes*, 19, 1653-1665, doi: 11002/hyp.5594.

Humphrey, N. F., Harper, J. T., and W. T. Pfeffer (2012), Thermal tracking of meltwater retention in Greenland's accumulation area, *J. Geophys. Res.*, 117, F01010, doi:11029/2011JF002083.

Illangasekare, T. H., Walter, R. J., Meier, M. F., and W. T. Pfeffer (1990), Modeling of meltwater infiltration in subfreezing snow, Water Resources Research, 26(5), 1001–1012, doi:11029/WR026i005p01001.

Jordan, R. (1991), A one-dimensional temperature model for a snow cover: Technical documentation SNTHERM.89, *Tech. Rep. Spec. Rep. 657*, U.S. Army Cold Regions Research Engineering Lab., Hanover, NH.

Jordan, R. (1995), Effects of capillary discontinuities on water flow and water retention in layered snowcovers, *Defence Science Journal*, 45(2), 79–91.

Jury, W., Wang, Z., and A. Tuli (2003), A conceptual model of unstable flow in unsaturated soil during redistribution, *Vadose Zone Journal*, 2, 61–67, doi:12113/2.1.61.

Katsushima, T., Yamaguchi, S., Kumakura, T., and A. Sato (2013), Experimental analysis of preferential flow in dry snowpack, *Cold Regions Science and Technology*, 85, 206-216, doi:11016/j.coldregions.2012.09.012.

Kool, J. B. and J. C. Parker (1987), Development and evaluation of closed-form expressions for hysteretic soil hydraulic properties, *Water Resources Research,* 23(1), 105-114, doi: 11029/WR023i001p001

Logie, W., Aselineau, A.-A., Pye, J. and J. Coventry (2015), Temperature and heat flux distributions in sodium receiver tubes, *Asia-Pacific Solar Research Conference*.

Likos, W., Lu, N. and J. Godt (2013), Hysteresis and uncertainty in soil-water retention curve parameters, *J. Geotech. Geoenviron. Eng.*, 140(4), doi:11061/(ASCE)GT.1943-5606.0001071.

Marks, D., Domingo, J., Susong, D., Link, T., and D. Garen (1999), A spatially distributed energy balance snowmelt model for application in mountain basins, *Hydrological Processes*, 13, 1935-1959, doi:11002/(SICI)1099-1085(199909)13:12/13<1935::AID-HYP868>3.CO;2-C.

Marsh, P. (1991), Water flux in melting snow covers, Chapter 2 in: M.Y. Corapcioglu (Editor), *Advances in Porous Media*, Vol. 1, Elsevier, Amsterdam, 61–124.

Marsh, P. and M. Woo (1984a), Wetting front advance and freezing of meltwater within a snow cover: 1. Observations in the Canadian Arctic, *Water Resources Research*, 20(12), 1853–1864, doi:11029/WR020i012p01853.

Marsh, P. and M. Woo (1984b), Wetting front advance and freezing of meltwater within a snow cover: 2. A simulation model, *Water Resources Research*, 20(12), 1865–1874, doi:11029/WR020i012p01865.

Marsh, P. and M. Woo (1985), Meltwater movement in natural heterogeneous snow covers, *Water Resources Research*, 21(11), 1710–1716, doi:11029/WR021i011p0171

Mualem, Y. (1974), A conceptual model of hysteresis, *Water Resources Research*, 10(3), 514-520, doi: 11029/WR010i003p00514.

Mualem, Y. (1976), A new model for predicting the hydraulic conductivity of unsaturated porous media, *Water Resources Research*, 12(3), 513-522, doi:11029/WR012i003p00513.

Mualem, Y. (1984), Prediction of the soil boundary wetting curve, *Soil Science*, 137(6), DOI: 11097/00010694-198406000-00001.

Nieber, J. (1996), Modeling finger development and persistence initially dry porous media, *Geoderma*, 70(2-4), 207-229, doi:11016/0016-7061(95)00086-

Parker, J., and R. Lenhard (1987), A model for hysteresis constitutive relations governing multiphase flow 1. Saturation-pressure relations, *Water Resources Research*, 23(12), 2187-2196, doi:11029/WR023i012p02187.

Pomeroy, J., Gray, D., Shook, K., Toth, B., Essery, R., Pietroniro, A., and N. Hedstrom (1998), An evaluation of snow accumulation and ablation processes for land surface modelling, *Hydrological Processes*, 12, 2339-2367, doi:11002/(SICI)1099-1085(199812)12:15<2339::AID-HYP800>3.CO;2-L.

Pfeffer, W., and N. Humphrey (1996), Determination of timing and location of water movement and ice-layer formation by temperature measurements in sub-freezing snow, *Journal of Glaciology*, 42, 292-304, doi:11017/S0022143000004159.

Pfeffer, W., Illangasekare, T., and M. Meier (1990), Analysis and modeling of melt-water refreezing in dry snow, *Journal of Glaciology*, 36(123), 238–246.

Ritsema, C., Dekker, L., Nieber J., and T. Steenhuis (1998), Modeling and field evidence of finger formation and finger recurrence in a water repellent sandy soil, *Water Resources Research*, 34(4), 555-567, doi:11029/97WR02407.

Schneebeli, M. (1995), Development and stability of preferential flow paths in a layered snowpack, *Biogeochemistry of Seasonally Snow-Covered Catchments* (Proceedings of a Boulder Symposium July 1995), IAHS Publ. no. 228.

Šimunek, J., van Genuchten, M., and M. Šejna (2012), Hydrus: model use, calibration and validation, *American Soc. of Agri. and Biol. Eng.*, 55(4), 1261-1274.

Šimunek, J., Sejna, M., Saito, H., Sakai, M., and M. van Genuchten (2008), The Hydrus-1D software Package for simulating the movement of water, heat, and multiple solutes in variably saturated media, Version 4.17, HYDRUS Software Series 3, Department of Environmental Sciences, University of California Riverside, Riverside, California, USA, pp. 315.

Spaans, E., and J. Baker (1996), The soil freezing characteristics: its measurement and similarity to the soil moisture characteristic, *Soil Sci. Soc. Am. J.*, 60, 13-19, doi: 12136/sssaj1996.03615995006000010005x.

Tseng P., Illangesakare, T., and M. Meier (1994a), Modeling of snow melting and uniform wetting front migration in a layered subfreezing snowpack, *Water Resources Research*, 30(8), 2363–2376, doi:11029/94WR00764.

Tseng, P., Illangasekare, T., and M. Meier (1994b), A 2-D finite element method for water infiltration in a subfreezing snowpack with a moving surface boundary during melt, *Advances in Water Resources*, 17(4), 205-219, doi:11016/0309-1708(94)90001-9.

van Genuchten, M. T. (1980), A closed-form equation for prediction the hydraulic conductivity of unsaturated soils, *Soil Sci. Soc. Am. J.*, 44, 892-898.

Verseghy, D. (1991), Class – A Canadian land surface scheme for GCMs. I. Soil model, *International Journal of Climatology*, 11, 111-133, doi: 11002/joc.3370110202.

Vionnet, V., Brun, E., Morin, S., Boone, A., Faroux, S., Le Moigne, P., Martin, E., and J.-M. Willemet (2012), The detailed snowpack scheme Crocus and its implementation in SURFEX v7.2, *Geosci. Model Dev.*, 5, 773-794.

Waldner, P., Schneebeli, M., Schultze-Zimmermann, U., and H. Flühler (2004), Effect of snow structure on water flow and solute transport, *Hydrological Processes*, 18 (7), 1271–129

Wankiewicz, A. (1979), A review of water movement in snow, Proceeding Modelling Snowcover Runoff, *Cold Regions Research and Engineering Laboratory*, Hanover, New Hampshire, 222-252.

Watts, T., Rutter, N., Toose, P., Derksen, C., Sandells, M., and J. Woodward (2016), Brief communication: Improved measurement of ice layer density in seasonal snowpacks, *The Cryosphere*, 10, 2069-2074, doi: 15194/tc-10-2069-2016.

Werner, A. D. and D. A. Lockington (2006), Artificial pumping errors in the Kool-Parker scaling model of soil moisture hysteresis, *Journal of Hydrology*, 325, 118-133, doi: 11016/j.jhydrol.2005.1012.

Wever, N., Fierz, C., Mitterer, C., Hirashima, H., and M. Lehning (2014), Solving Richards equation for snow improves snowpack meltwater runoff estimations in detailed multi-layer snowpack model, *The Cryosphere*, 8, 257-274, doi:15194/tc-8-257-2014.

Wever, N., Schmid, L., Heilig, A., Eisen, O., Fierz, C., and M. Lehning (2015), Verification of the multi-layer SNOWPACK model with different water transport schemes, *The Cryosphere*, 9, 2271-2293, doi:15194/tcd-9-2271-2015.

Wever, N., Wurzer, S., Firez, C., and M. Lehning (2016), Simulating ice layer formation under the presence of preferential flow in layered snowpacks, The Cryosphere, 10, 2731-2744, doi:15194/tc-10-2731-2016.

Williams, M., Erickson, T., and J. Petrzelka (2010), Visualizing meltwater flow through snow at the centimeter-to-meter scale using a snow guillotine, *Hydrological Processes*, 24, 2098-2110, doi:11002/hyp.763

Würzer, S., Wever, N., Juras, R., Lehning, M., and T. Jonas (2017), Modelling liquid water transport in snow under rain-on-snow conditions – considering preferential flow, *Hydrol. Earth. Syst. Sci.*, 21, 1741-1756, doi:15194/hess-21-1741-2017.

Yamaguchi, S., Katsushima, T., Sato, A., T. Kumakura (2010), Water retention curve of sow with different grain sizes, *Cold Regions Science and Technology*, 64(2), 87-93, doi:11016/j.coldregions.20105.008.

Yamaguchi, S., Watanabe, K., Katsushima, T., Sato, A., and T. Kumakura (2012), Dependence of the water retention curve of snow on snow characteristics, *Annals of Glaciology*, 53(61), 6–12, doi:13189/2012AoG61A001.

CHAPTER 4

FIELD EXAMINATION OF PREFERENTIAL FLOW THROUGH SNOWPACKS AND COMPARISON TO MODELS

Abstract

Field studies of snowmelt processes have highlighted the occurrence of preferential flow in melting snow. This phenomenon has a significant impact on the transport of meltwater through snow. Due to the emergence of innovative and complex snow models that can simulate meltwater flow through both snow matrix and preferential flow on both flat and sloping terrains, there is an increasing need for quality field data to validate these new models. In the past, lack of field data has prevented further development of innovative snow models. In this study, two field studies are presented, as well as analysis of the data collected. In the first study, a dye tracer experiment was conducted in initially cold snow. This experiment showed the formation of preferential flow in snow, and photographs were taken of the flow patterns at different locations within the snowpack. Through analysis of the images, the geometry of preferential flow paths was revealed to have fractal characteristics. The second study consisted of a controlled melt experiment. Melt at the surface of a sloping snowpack was artificially generated, and the outflow at a known depth from the surface was measured with a lysimeter. Initial and final snow properties (layer density, grain size, temperature and water content) were also observed. These data were used to run and evaluate the outputs of a 2D snowmelt model that can simulate formation of preferential flow paths in snowpacks and couples mass and energy fluxes through snow. When compared with field observations, the model performed poorly. Some potential reasons for this failure are discussed, principally the use of a water entry pressure is believed to delay the flow of water through the snowpack and prevent formation of preferential flow for snow densities below 350 kg m^{-3}.

4.1 Introduction

In cold regions, snowmelt is the primary hydrological event of the year. Fresh water generated from melting snowpacks feeds mountain streams and downstream rivers. The slope of the terrain partially controls the timing of delivery of meltwater to the streams. In mountainous terrain, accurately predicting the timing of snowmelt runoff is challenging, as sloping snowpacks dominate the landscape. Routing meltwater through sloping snowpacks is a complex process that combines different flow patterns. First, in sloping snowpacks, lateral flow occurs at layer interfaces and capillary barriers (*Williams et al*., 2010; *Eiriksson et al.*, 2013). In addition to lateral flows, field studies have highlighted the occurrence of preferential flow paths in both flat and sloping snowpacks (*Marsh and Woo*, 1984; *Schneebeli*, 1995; *Waldner et al.*, 2004; *Williams et al.*, 2010). These two flow processes are either unaccounted for or crudely accounted for in the most sophisticated operational snow models (e.g. *Würzer et al.*, 2017), resulting in inaccurate prediction of the timing of meltwater reaching the base of the snowpacks (*Hirashima et al.*, 2017).

Field or laboratory data are necessary to evaluate the meltwater routing schemes in snowmelt models. Measurement of the bulk water content in snow (*Morin et al.*, 2012; *Thompson et al.*, 2016; *Smith et al.*, 2017) or observation of liquid water content at different depths within snowpacks during natural snowmelt (*Avanzi et al.*, 2014; *Clayton*, 2017) are crucial data to validate the melt prediction of snowmelt models. This information is now commonly measured in natural snowpacks. Snowmelt outflows at the base of snowpacks have also been recorded in the field using lysimeters (*Tekeli et al.*, 2005; *Eiriksson et al.*, 2013; *Juras et al.*, 2017). Such field data have commonly been used to validate snowmelt models or different schemes for water flow through snow (e.g. *Hirashima et al.*, 2010; *Wever et al.*, 2014, 2015; *D'Amboise et al.*, 2017). The formation of preferential flow within a snowpack (e.g. *Marsh and Woo*, 1984; *Schneebeli*, 1995; *Waldner et al.*, 2004), however, increases the difficulty of accurately measuring water content within snow. Therefore, studies using water sprayed on top of snow have begun looking at the flow of water or capillary pressure through small (< 30 cm) artificial snow samples (*Waldner et al.*, 2004; *Katsushima et al.*, 2013; *Avanzi et al.*, 2016). These data are useful to validate snow models capable of simulating preferential flow paths (*Hirashima et al.*, 2014, 2017; *Leroux and Pomeroy*, 2017). These models should be evaluated at macroscale (~1 m) under controlled conditions. Additionally, the melt component of these models must be verified without having to

compute the energy balance over snow. This energy balance cannot be closed using current theories (*Helgason and Pomeroy*, 2012), therefore resulting in uncertainties when estimating mass flux at the snow surface.

Tracer dye experiments have been applied in many studies of water flow through snow, in laboratory experiments and in natural snowpacks (*Marsh and Woo*, 1984; *Schneebeli*, 1995; *Waldner et al.*, 2004; *Campbell et al.*, 2006; *Williams et al.*, 2010; *Avanzi et al.*, 2016). The first experiments were mainly qualitative; they highlighted the occurrence of preferential flow paths in snow (*Schneebeli*, 1995), the effect of ice layers in decelerating the downward flow of water (*Campbell et al.*, 2006), and the ponding and lateral spread of water at stratigraphic interfaces (*Waldner et al.*, 2004; *Campbell et al.*, 2006). In a few studies, the spatial distribution and the dimensions of preferential flow paths were quantified during tracer dye experiments (*Marsh and Woo*, 1984; *Williams et al.*, 2010). Additional data on the spatial distribution of preferential flow paths in snow and relating them to snow layer properties (such as grain size and density) would help validate the emerging models that are able to simulate preferential flow through snow (*Hirashima et al.*, 2014; *Leroux and Pomeroy*, 2017).

This study presents a field experiment conducted in the Canadian Rockies, during which melt at the surface of natural snowpacks was artificially generated. The data collected are presented, and used to evaluate the SMPP, a 2D snow model that can simulate preferential flow and snowmelt (*Leroux and Pomeroy*, 2017). Data collected during dye experiments are also shown and analysed.

4.2 Dye Experiment

4.2.1 Field Measurements

A snowmelt and tracer dye experiment was conducted at the Fortress Mountain Laboratory in the Canadian Rockies on April 1, 2015. The experiment was conducted on flat terrain. The snowpack was about 1 m deep and the snow surface was wind-scoured. Prior to the experiment, the snowpack temperature was below freezing (the upper 20 cm were between -2^{o}C and -3^{o}C). The upper snowpack (10 cm) was composed of fresh snow with a density of 198 kg m^{-3}, which was separated by an ice layer from a 30 cm faceted snow layer of 320 kg m^{-3} density. The rest of the snowpack was a mix of faceted layers and compacted snow. Powder Brilliant Blue food dye, as used in *Williams et al.* 2010, was sprinkled over the flat snowpack. A hot plate was designed to generate

rapid melt on top of the dyed snow surface. The hot plate consisted of a 90x90 cm sheet metal on which a 6 m heat tape (Omega SRT101-180) was fixed. The heat tape was plugged into a portable gasoline generator to generate melt at the surface (UnitedPower GG1300).

After about 4 hours of melt, the hot plate was turned off and removed from the snow surface. The melted snow surface lowered by about 16 cm and meltwater was observed to have percolated down to between 40 cm and 60 cm from the snow surface. This artificial melt generated by the hot plate is faster than melt rates under many natural conditions. However, a snowpack depletion of 16 cm can be observed in the alpine over a whole day under warm conditions. The accelerated melt rate most likely resulted in somewhat different meltwater routing than that under natural conditions. In particular, no refreezing of meltwater occurred in the upper snowpack during the field experiment because of the high input heat flux from the hot plate that raised the upper snowpack temperature to 0^{o}C before meltwater could reach the initially dry and subfreezing upper snowpacks. The high flux and fast melt rate most likely accelerated snow metamorphism in the upper snowpack; for instance, the rapid increased of liquid water content within the snowpack due to the high input heat flux, the transition between the pendular and funicular regimes was short and grain growth only occurred in the funicular regime. The accelerated melt at the surface might have resulted in more matrix flow occurring in the upper snowpack than what would be observed under natural conditions, and in increased meltwater velocity within the preferential and matrix domains. Despite the added uncertainties by accelerating melt rate at the snow surface, the results of the dye experiment (Fig. 4.1) qualitatively agree with other experiments conducted under natural conditions (e.g. Marsh and Woo, 1984). This lends confidence that results from the artificial melt experiment are applicable to many natural snowmelt conditions involving rapid melt onset over cold snowpacks. Such conditions are not uncommon in the Canadian Rockies

After the hot plate was turned off, four snowpits were then dug under the blue dyed surface and photographs were taken of the snowpit faces, showing blue areas where liquid water percolated the snow and remaining white areas where the snow stayed dry and cold (Fig. 4.1). The flow patterns showed the presence of both matrix flow at the upper snowpack and preferential flow paths below the matrix flow. Liquid water also ponded at layer interfaces, which was characterised by darker blue colours. The presence of liquid water was observed down to 60 cm from the snow

surface. During the experiment, seven photographs were taken, all showing similar flow behaviours.

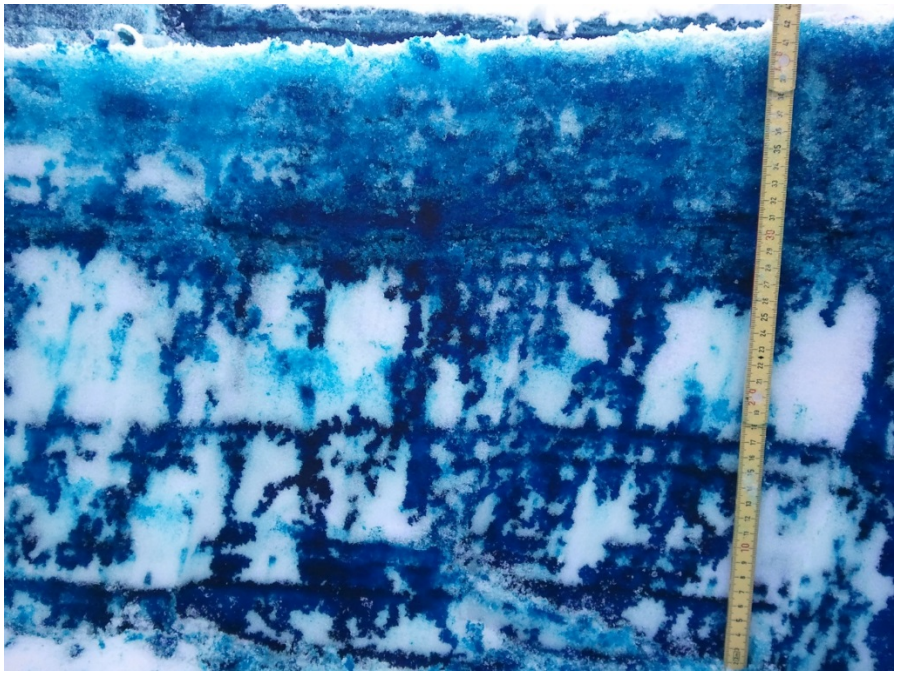

Figure 4.1 Photo of a snowpit face after 4 hours of melt of the dyed surface. The blue represents the dyed meltwater that percolated from the surface.

4.2.2 Data Processing

In each picture taken after the melt, preferential flow paths were observed. The photographs were cropped to isolate sections that only include connected preferential flow paths between two consecutive snow layers. These cropped images were binary in black and white, where white represents observed preferential flow paths (blue colour in the RGB photos) and the black exhibits the dry and cold snow areas. The binarization was done by filtering the blue and green spectral bands out of the images, leaving only the red spectral band. In these images in the red band, the initial blue colours from the dyed water appeared black. An example of a binary image is shown in Figure 4.2.

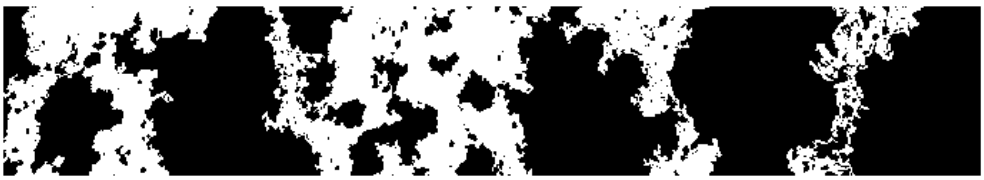

Figure 4.2 Binary image from RGB photograph of snowpit face after the melt and dye experiment. The black represents dry and cold snow and the white shows the preferential flow paths characterized by the blue dye color in the original photograph (e.g. Fig. 4.1).

Using Matlab (MATHWORK) functions, the connected components present in the binary images were separated. A threshold corresponding to a number of pixels was manually chosen to disregard the small connected components, to consider only well-developed preferential flow paths. For instance, a threshold of 2500 pixels was selected for the binary image in Fig. 4.2. Figure 4.3 shows the connected components found in the binary image of Fig. 4.2. Each colour corresponds to a different connected preferential flow path.

Figure 4.3 Processed image from the binary image in Fig. 4.2 that shows the isolated connected preferential flow paths in different colours.

4.2.3 Fractal Objects

A total of 16 images (similar to Fig. 4.3), each containing 2 or more connected preferential flow paths were produced. This resulted in a total of 40 isolated connected preferential flow paths. A Matlab function (*regionprops*) was applied to obtain the area (A) and perimeter (P) of each connected preferential flow path, which were determined by the number of pixels within and at the boundary of each isolated preferential flow path, respectively.

In this section, the geometry of preferential flow paths is analysed. The geometry of preferential flow paths is studied using fractal geometry, i.e. their perimeter-area and area-frequency characteristics can be described by power equations (*Mandelbrot*, 1983). This approach is inspired by other snow studies that analyzed the fractal geometry of patchy snowcovers (*Shook et al.*, 1993)

and of intercepted snow by forest canopies (*Pomeroy and Schmidt*, 1993; *Pomeroy et al.*, 1998). The equations used in this section were also used in these snow studies.

The power law describing the perimeter-area relationship is:

$$P = k\, A^{D_P/2}, \tag{4.1}$$

where k is a constant and D_p the fractal dimension (> 1.0).

Figure 4.4 shows a scatter plot of the estimated P values against the estimated A values for the 51 connected preferential flow paths. R^2 for the scatter data against the fitted line was equal to 0.93. The coefficients k and D_p, determined from the equation of the fitted line were 4.43 pixels and 1.24, respectively. Ironically, the fractal dimension of the preferential flow paths is close to the fractal dimension of the Koch snowflake (=1.26).

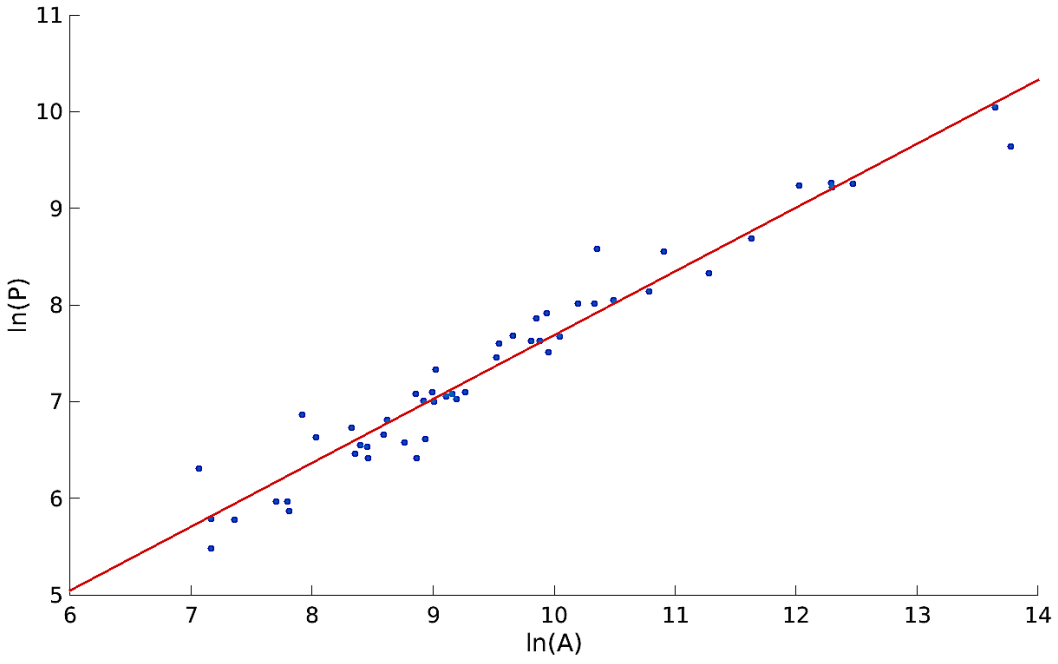

Figure 4.4 Scatter plot of logarithmic values of the estimated perimeters (P) and logarithmic values of the areas (A) for all the 51 isolated preferential flow paths. The red line is a linear fit to the scatter plot.

Korcak's law is:

$$F(A) = cA^{-D_K/2}, A > A_{\min} \quad (4.2)$$

with $F(A)$ the number of objects with a size equal to or greater than area A, c is a constant, and D_K a fractal dimension (different from D_p).

Figure 4.5 plots logarithmic values of $F(A)$ against logarithmic values of A (blue dots), as well as the fitted linear curve (red line); R^2 was equal to 0.89. The fractal dimension D_K was found equal to 1.36, which is the same value as for D_p and c was equal to 15733 pixels.

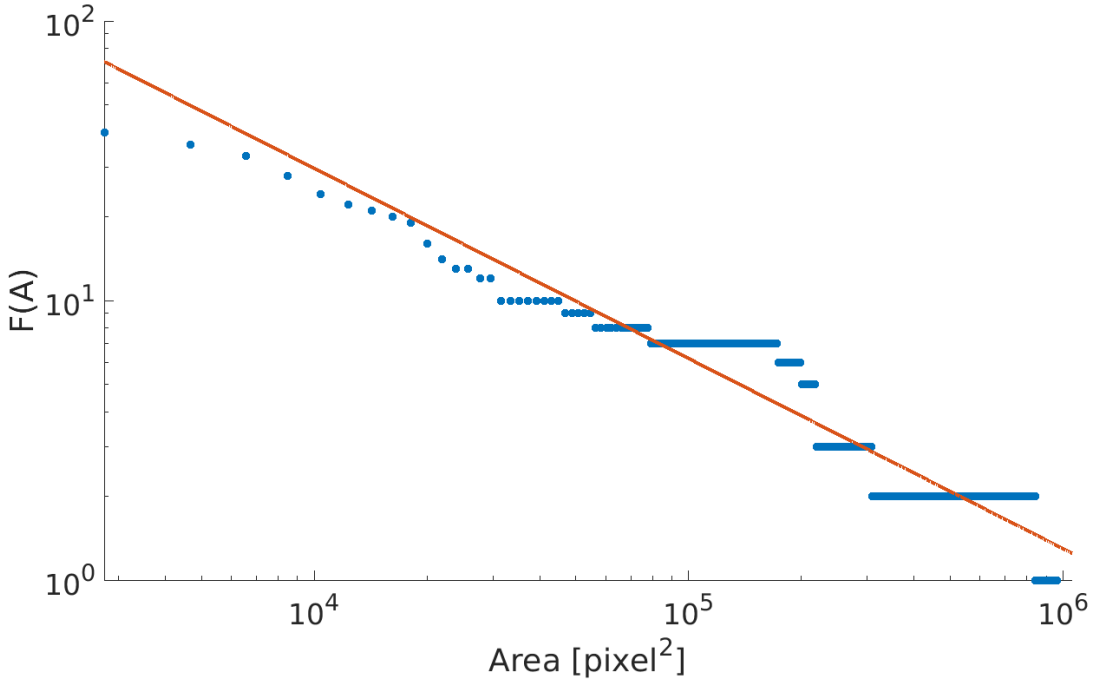

Figure 4.5 Scatter plot of the logarithmic values of the estimated numbers of objects with areas equal or greater to A ($F(A)$) and the logarithmic values of areas (A) from the processed images. The red line is a linear fit to the scatter plot.

4.2.4 Discussion and Conclusion

From 2D images of 40 isolated preferential flow paths, analysis showed that the geometry of preferential flow paths is similar to those of fractals. The fractal dimensions of preferential flow paths were similar to the fractal dimension of intercepted snow that varied between 1.22 and 1.44 (*Pomeroy and Schmidt*, 1993) and to the fractal dimension of patchy snowcovers that varied

between 1.2 and 1.4 (*Shook et al.*, 1993). To expand the results presented in this study, a similar analysis could be done on 3D observations of preferential flow paths, such as with the data collected by *Williams et al.* (2010). These results could then be used to evaluate new emerging models that have the potential to simulate preferential flow in snow (*Hirashima et al.*, 2014, 2017; *Leroux and Pomeroy*, 2017). To compare such models with the results presented in this study, simulations of preferential flow paths must be done at very fine resolution to accurately compute the fractal relationships from the simulation results.

Future studies should relate the shape and spatial distribution of preferential flow paths with snowpack internal properties. Thus, future similar analyses, while also measuring the snow internal properties (layer densities, grain sizes and temperatures) prior to melting the dyed snow surface, could potentially relate the fractal geometry of preferential flow paths to snow properties.

4.3 Melt Flow Measurement and Model Comparison

4.3.1 Field Measurements

A "hot plate experiment" was designed to generate melt at the surface of a natural snowpack. The outflow resulting from surface melt was then measured at a known depth inside the snowpack. This experiment was conducted at Bonsai Clearing, Fortress Snow Laboratory, Kananaskis Country, Alberta. This site is approximately 30 m in diameter and the ground is slightly sloped by an angle of 6/7^{o}.

In this field study, the "hot plate" from the dye experiment (Section 4.2) is again used. In the field, the hot plate was placed onto the snow surface and the heat tape was plugged into a generator to artificially generate melt of the snow surface. The top of the hot plate that was facing the sky was insulated with a comforter and a silver blanket. Two heat flux plates (Huskeflux HFP01) were placed between the hot plate and the snow surface to measure the heat flux delivered to the snowpack every 10 min. After placing the hot plate on the snowpack, a snowpit was dug at the downward edge of the plate to insert a 1 x 1 m lysimeter into the snow at a certain depth below the surface (Fig. 4.6). A tipping bucket rain gauge (Campbell Scientific TE525) was positioned below the hose of the lysimeter (situated downward of the lysimeter) to measure the meltwater flow released from the lysimeter (Fig. 4.6). The snowpit face was covered with a silver blanket to insulate the snow from the atmosphere and prevent lateral melt.

Another snowpit was dug about a meter away from the hot plate before running the experiment. The initial snow stratigraphy, i.e. the depth and properties (snow density, layer grain size, temperature, and water content) of the different snow layers was observed. Snow density was measured every 10 cm using a 1000 cc wedge cutter, snow surface and internal temperatures were obtained with a dial stem thermometer (accuracy of ± 1°C), the grain size of each layer was estimated using a crystal card and a magnifying loop, and snow water content in the middle of each 10 cm layer was measured using a Denoth meter (*Denoth*, 1994). After running the experiments, snow properties of the melted snowpack were once again measured at two different locations.

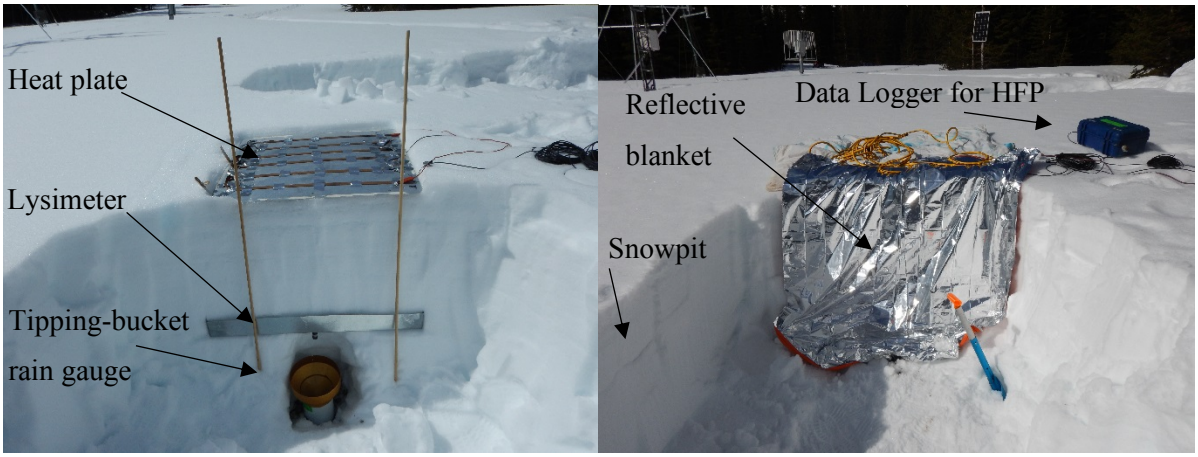

Figure 4.6 "Hot plate" experiment field setup.

Experimental data were collected on April 1, April 4, April 5, and April 8, 2016. Table 4.1 summarizes the average snowpack properties before and after each experiment. The snowpacks on 04/01 and 04/04 presented cold snow layers, and the snowpacks on 04/05 and 04/08 were isothermal at the melting point. The three first studies (04/01, 04/04, and 04/05) were conducted in 50 cm snowpacks, and the snowpack on 04/08 was 70 cm high. The experiments began each day around 11 am and lasted for about 3 hours. For each experiment, the snowpack had a slope angle of 6.5°.

Figure 4.7 shows the time at which the first outflow through the hose of the lysimeter was observed. As the snowpack warmed up, from the first experiment to the third experiment, the time of first outflow occurred sooner. For both isothermal snowpacks (04/05 and 04/08), outflow occurred later for the deeper snowpack.

Table 4.1 Measured snow properties prior and after the experiments.

Date (Month/day)		Depth [m]	Average dry density [kg m^{-3}]	Average water content [%]	Number of ice layers	Average snowpack temperature [^{o}C]	Average input flux [W m^{-2}]
04/01	Before	0.5	276	5	4	-8	861
	After	0.42	217	9.6	NA	0	
04/04	Before	0.5	325	4	5	-4	914
	After	0.44	271.4	9.4	NA	0	
04/05	Before	0.5	300	8	3	0	923
	After	0.42	220	13.0	NA	0	
04/08	Before	0.7	329	1.2	4	0	646
	After	0.65	216	14.7	NA	0	

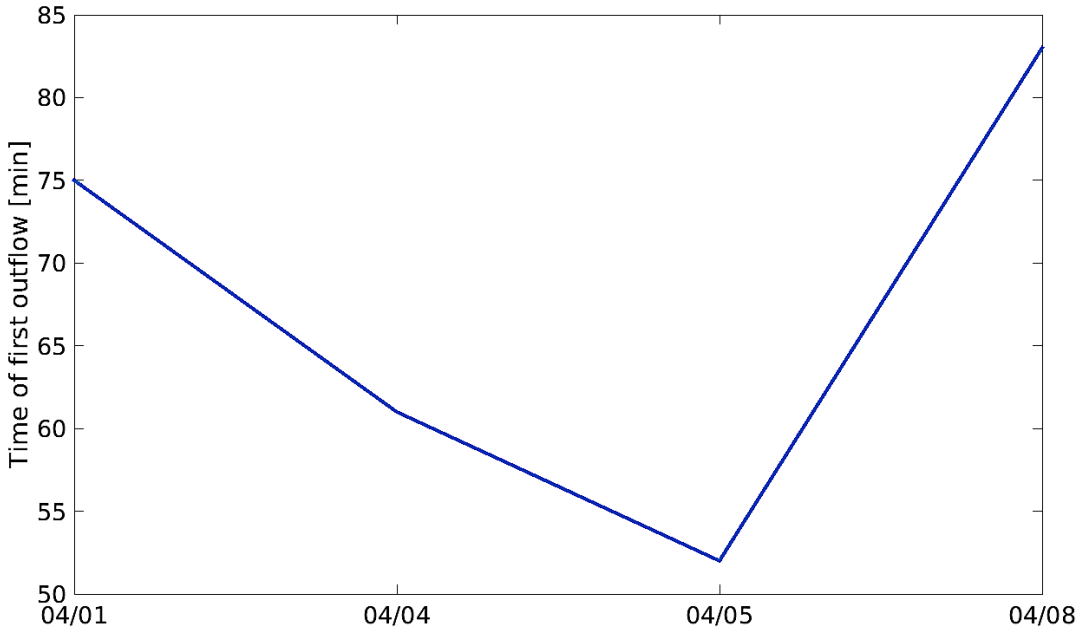

Figure 4.7 Times at which first outflow was observed for the experiments conducted on 04/01, 04/04, 04/05, and 04/08.

4.3.2 Model Comparison

The model developed by *Leroux and Pomeroy* (2017) was used to represent meltwater outflow observed during the four experiments. Because this model is 2D, only a two-dimensional cross section (parallel to the slope) of the natural snowpacks was modelled, and homogeneity was assumed in the third dimension (perpendicular to the slope). Fluctuations following a Gaussian distribution of standard deviation of 10% and 5% were applied in each numerical cell to the observed average grain size and density of each snow layer. The height of the snowpack in the model corresponded to the depth at which the lysimeter was inserted. The lateral length of the snowpack was set to be the same as the length of the hot plate (90 cm). The numerical grid resolution was 1x1 cm. The snow properties that were measured prior to running each experiment (density, grain size, temperature, and water content every 10 cm) were used to initialize the model. Given that the experiments were conducted in the spring and melting and refreezing of the snowpack had previously occurred, round snow grains were observed in the upper part of the snowpack, except for the ice layers. Therefore, the mean grain diameter that was measured in the field was assumed to be equivalent to the optical grain diameter, and it was estimated at 1 mm. The average heat flux from the two heat flux plates was applied in the model as an upper boundary condition to generate melt (top graphs in Fig. 4.8). It can be observed that the two heat fluxes measured at different locations on the snow surface are relatively similar. Thus, it is assumed that the heat flux from the hot plate to the snow surface is spatially homogeneous. In the simulation, the heat flux at the bottom of the snowpack was assumed to be 0 W m^{-2}. The hole in the lysimeter that allowed meltwater to flow to the tipping bucket rain gauge was 2 cm in diameter. Thus, in the model, liquid water was allowed to leave the snowpack at the endmost 2 cm downhill of the snowpack. The rest of the bottom boundary condition was set to no-flow.

The simulated and observed meltwater outflows for each experiment are compared in the lower graphs in Fig. 4.8. The simulated outflow was plotted every 10 min, which is the interval over which the input flux was averaged. In all cases, the time at which simulated outflow first occurred was later than the observed times. Simulated total outflows were all under-estimated. At the end of each simulation, the model simulated an ablation of 7.3 cm, 7.2 cm, 9.7 cm, and 4.6 cm for the simulations corresponding to the 04/01, 04/04, 04/05, and 04/08, respectively. This is in close agreement with the data presented in Table 4.1.

Figure 4.9 shows the distribution of simulated liquid water content at different times using the data collected on 04/01. The model simulated no preferential flow paths; neither was water estimated to be ponding at the layer interfaces. However, lateral flows throughout all cells occurred despite the small slope angle (6°). A high saturation layer was modelled at the bottom of the snowpack. This was also observed during the field experiments.

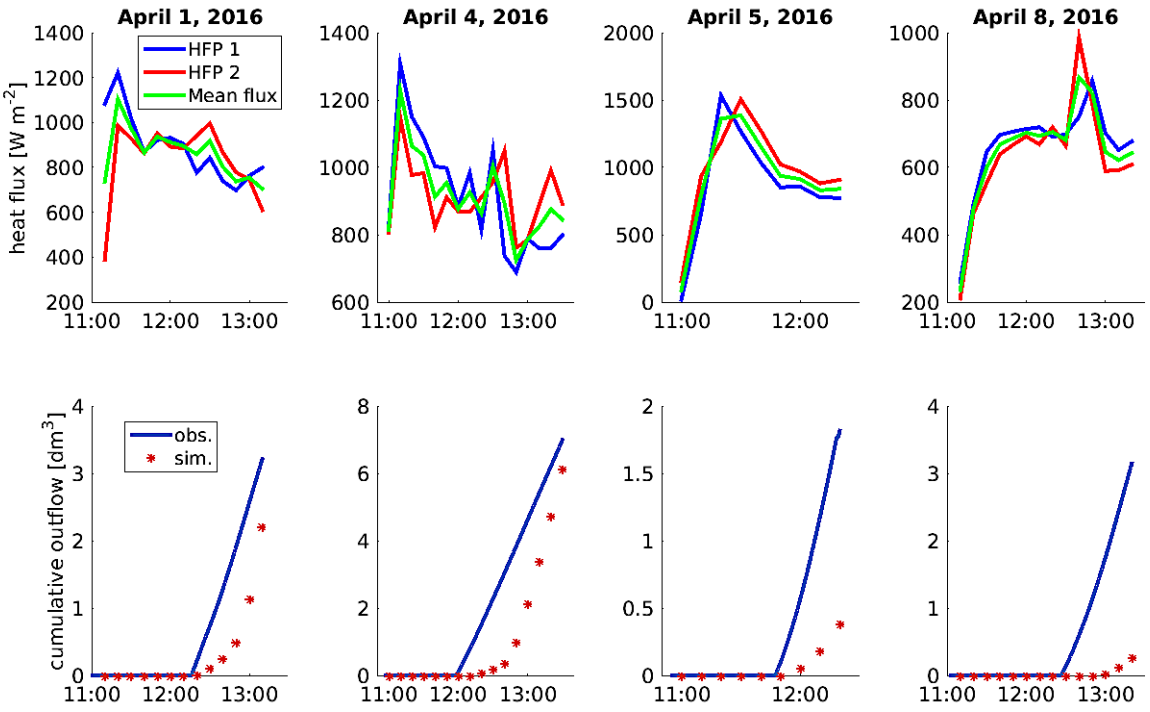

Figure 4.8 Top graphs show the two measured heat fluxes and the average of the two between the hot plate and the snowpack for 4 different experiments. The bottom graphs show the observed (blue line) and simulated (red dots) outflows during 4 different experiments.

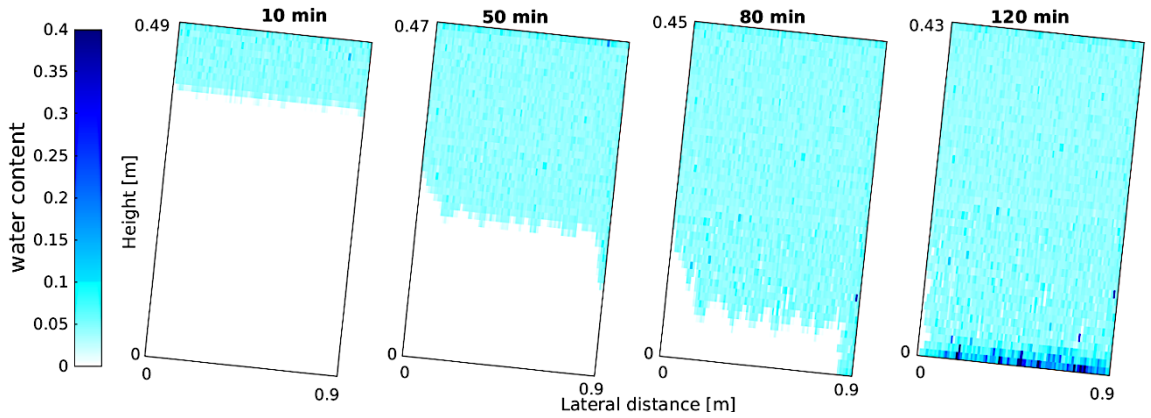

Figure 4.9 Simulated water content distribution at different times using the data collected on 04/01.

4.3.3 Discussion

The field campaign was designed to evaluate the model developed by *Leroux and Pomeroy* (2017). The melt of a natural snowpack was generated using a hot plate to avoid uncertainties when applying the energy balance above snow to estimate melt at the surface. The layered structure (layer depth and properties) of the snowpacks was observed for every 10 cm of vertical resolution prior to running each experiment. Many ice layers were distinguished within the snowpacks; however, they could not be included in the numerical model, as the optical grain size and density of ice layers are not known and because of the vertical resolution of 10 cm of the field data that prevented describing ice layers in the model initial conditions. Including the ice layers in the initial snowpack stratigraphy in the model could have resulted in a slightly improved prediction of the timing and magnitude of meltwater outflow. However, due to the high heat input flux at the surface and the high meltwater content within the snowpack (observed at the end of the field experiment), ice layers degenerated rapidly in the field experiments and this process cannot be accurately simulated in the model due to lack of information on how ice layer properties change during melt (*Marsh*, 1991). Similarly, even though grain size was measured using a snow crystal card and a magnifying loop, these values could not be used as inputs in the model, as optical grain size is required to estimate snow hydraulic parameters. Because the experiments were conducted early in the melt season, natural melt-freeze cycles already occurred prior to doing the experiments. This resulted in the presence of rounded grains with diameters ranging between 1 and 1.5 mm in the upper snowpack (except for the ice layers) caused by wet snow metamorphism during the previous melt cycles. This justifies the use of a constant value of optical grain size. In this case 1 mm was

used in the model for all snow layers. As model behaviour varies with the input value of optical grain size (*Leroux and Pomeroy*, 2017), this assumption created additional uncertainties in the simulated outflow.

The model poorly represented the observations; the simulated outflow occurred later than in the observations. This lag can be caused by the 3D nature of the field data, as well as uncertainties in the model inputs. In addition, no preferential flow paths were simulated. The model inputs and initial conditions were varied to determine under which conditions preferential flow paths occurred using the data. From 04/01: the grid resolution was decreased (from 1 cm to 5 cm), as well as the optical grain size for each layer (from 1 mm to 5 mm) and the heat input flux (down to a constant flux of 100 W m^{-2}), the heterogeneities in grain size and density were increased (by a factor of 2), and the snow density of each layer was also increased (to 450 kg m^{-3} for each layer). Preferential flow paths formed in the model only when the snow density of each layer was increased (Fig. 4.10); for the other conditions stated above, matrix flow was simulated. As the snow density increased, the estimated capillary pressure within the snow also increased and the water content accumulating at the interface of wet to dry snow layers increased; an increase of snow density in the model created the necessary conditions for preferential flow to form. It was thus concluded that the conditions for preferential flow to form in the model were not met when using the natural snowpack properties, i.e. water accumulation and fast percolation (*Leroux and Pomeroy*, 2017). This raises the question of whether the capillary entry pressure estimated by *Katsushima et al.* (2013) is valid for a wide range of snow densities, as it was developed for snow samples with densities greater than 380 kg m^{-3}. The use of water entry pressure in snow may not be appropriate to simulate preferential flow paths, and future study should consider other methods to estimate preferential flow in snow.

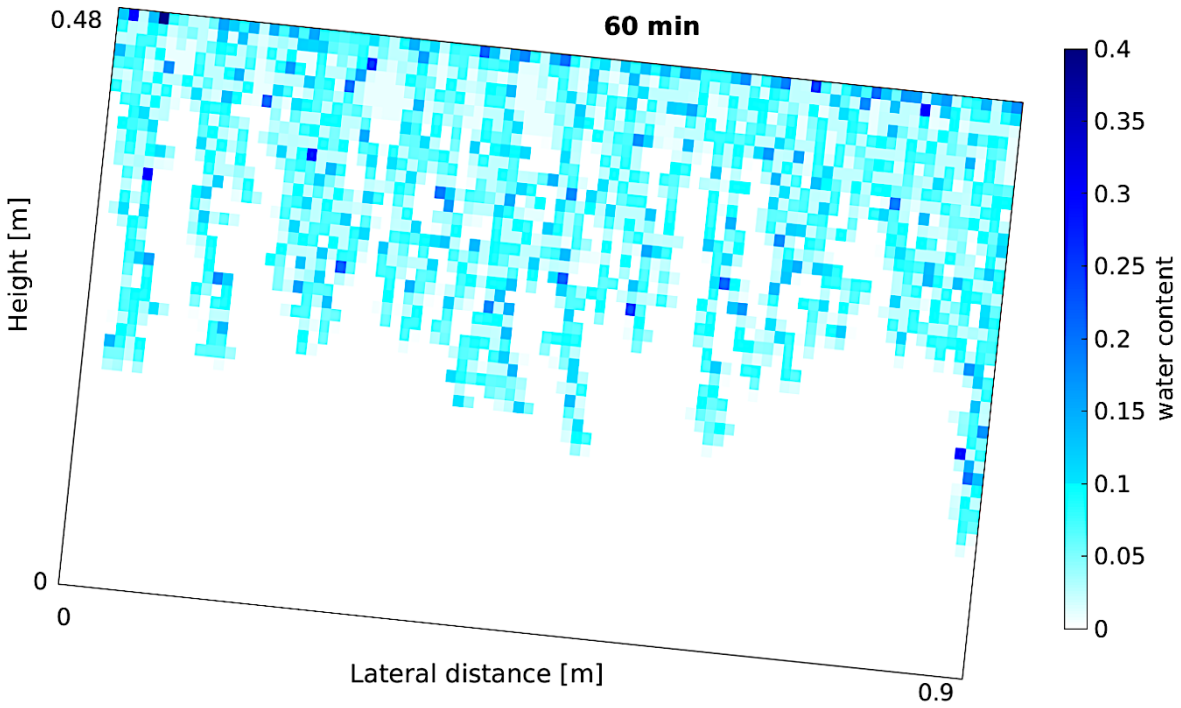

Figure 4.10 Simulated water content distribution using the heat flux measured during the experiment on 04/01 with a snow density of 450 kg m^{-3}.

4.4 Conclusion

In the first section of this chapter, a dye field experiment was presented and the fractal geometry of 2D preferential flow paths was analyzed. The fractal dimensions of the 2D preferential flow paths were similar to those of other snow processes, such as snow interception by canopy and patchy snowcover. Further work is required to measure the fractal geometry of more preferential flow paths in different snowpacks with different properties. This could then be used to evaluate the simulation of preferential flow paths by new emerging numerical snow models (*Hirashima et al.*, 2014, 2017; *Leroux and Pomeroy*, 2017).

The second study presented a field campaign designed to artificially generate the melt of natural snowpacks and to measure meltwater outflow. These data were used to evaluate a 2D numerical snow model capable of representing preferential flow in snow. The 2D model was not able to simulate formation of preferential flow paths, resulting in a delay in estimated meltwater outflow. The use of water entry pressure to generate preferential flow paths was deemed not appropriate for natural snow with densities lower than 380 kg m^{-3} (the density used in the laboratory experiments

to estimate the water entry pressure equation). Therefore, the current approach applied to trigger the formation of preferential flow in a snow model could be improved.

Additional field studies such as the one presented here are needed to improve the accuracy of emerging models that can simulate both matrix and preferential flows. When evaluating the model against field data, problems were encountered with the data applied as model inputs and with the model representation of water transport. In future studies, the optical snow grain size of each layer should be measured in the field; for example, using near-infrared images (*Montpetit et al.*, 2012). This would help better predict the snow hydraulic properties in the model.

Key Points for the Next Chapter

- Understanding the current limitations of using water entry pressure to simulate preferential flow, how can preferential flow paths be simulated without using water entry pressure?
- How can the water retention curve be modified to estimate capillary pressure when the water content is below the residual value?

4.5 References

Avanzi, F., Caruso, M., Jommi, C., De Michele, C., and A. Ghezzi (2014), Continuous-time monitoring of liquid water content in snowpacks using capacitance probes: a preliminary feasibility study, *Adv. in Water Resour.*, 68, 32-41.

Avanzi, F., Hirashima, H., Yamaguchi, S., Katsushima, T. and C. De Michele (2016), Observations of capillary barriers and preferential flow in layered snow during cold laboratory experiements, *The Cryosphere*, 10, 2013-2026, doi: 15194/tc-10-2013-2016.

Campbell F, Niewnow P, and R. Purves (2006), Role of the supraglacial snowpack in mediating meltwater delivery to the glacier system as inferred from dye tracer experiments. *Hydrological Processes* 20: 969–985.

Clayton, W. S. (2017), In situ measurement of meltwater percolation flux in seasonal alpine snowpack using self potential and capillary pressure sensors, *The Cryosphere Discuss.,* doi: 5194/tc-2017-187

D'Amboise, C. J. L., Müller, K., Oxarango, L., Morin, S., and T. V. Schuler (2017), Implementation of a physically based water percolation routine in the Crocus/SURFEX (V7.3) snowpack model, *Geosci. Model Dev.*, 10, 3547-3566, doi:https://doi.org/15194/gmd-10-3547-2017

Eiriksson, D., M. Whitson, C. H. Luce, H. P. Marshall, J. Bradford, S. G. Benner, T. Black, H. Hetrick, and J. P. Mcnamara (2013), An evaluation of the hydrologic relevance of lateral flow in snow at hillslope and catchment scales, *Hydrol. Process.*, *27*, 640–654, doi:11002/hyp.9666.

Helgason, W. and Pomeroy, J. (2012). Problems closing the energy balance over a homogeneous snow cover during midwinter. *Journal of Hydrometeorology*, 13:557–572.

Hirashima, H., Avanzi, F., and S. Yamaguchi (2017), Liquid water infiltration into a layered snowpack: evaluation of a 3-D water transport model with laboratory experiments, *Hydrol. Earth Syst. Sci.*, 21, 5503-5515, doi:15194/hess-21-5503-2017.

Hirashima, H., Yamaguchi, S., and T. Katsushima (2014), A multi-dimensional water transport model to reproduce preferential flow in the snowpack, *Cold Regions Science and Technology*, 108, 80-90, doi:11016/j.coldregions.2014.09.004.

Hirashima, H., Yamaguchi, S., Sato, A. and M. Lehning (2010), Numerical modeling of liquid water movement through layered snow based on new measurements of the water retention curve, *Cold Regions Science and Technology*, 64(2), 94-103, doi:11016/j.coldregions.20109.003.

Leroux, N. R. and J. W. Pomeroy (2017), Modelling capillary hysteresis effects on preferential flow through melting and cold layered snowpacks, *Adv. in Water Res*., 107, 250-264, doi: 11016/j.advwatres.2017.06.024.

Mandelbrot, B. B. (1983), The fractal geometry of nature, W.H. Freeman and Co., New York. NY.

Marsh, P. and M. Woo (1984), Wetting front advance and freezing of meltwater within a snow cover: 1. Observations in the Canadian Arctic, *Water Resources Research*, 20(12), 1853–1864, doi:11029/WR020i012p01853.

Montpetit, D., Royer, A., Langlois, A., Cliché, P., Roy, A., Cjampollion, N., Picard, G., Domine, F., and R. Obbard (2012), New shortwave infrared albedo measurements for snow specific surface area retrieval, *Journal of Glaciology*, 58(211), doi:13189/2012JoG11J248.

Morin, S., Lejeune, Y., Lesaffre, B., Panel, J.-M., Poncet, D., David, P., and M. Sudul (2012), An 18-yr long (1993–2011) snow and meteorological dataset from a mid-altitude mountain site (Col de Porte, France, 1325 m alt.) for driving and evaluating snowpack models, *Earth Syst. Sci. Data*, 4, 13-21, https://doi.org/15194/essd-4-13-2012.

Pomeroy, J.W., Parviainen, J., Hedstrom, N., and D.M. Gray (1998), Coupled modeling of forest snow interception and sublimation, *55th Eastern Snow Conference*, 101-114.

Pomeroy, J.W., and R.A. Schmidt (1993), The use of fractal geometry in modeling intercepted snow accumulation and sublimation, *50th Eastern Snow Conference, 61th Western Snow Conference*, 1-1.

Schneebeli, M. (1995), Development and stability of preferential flow paths in a layered snowpack, *Biogeochemistry of Seasonally Snow-Covered Catchments* (Proceedings of a Boulder Symposium July 1995). IAHS Publ. no. 228.

Shook, K., Gray, D.M., and J.W. Pomeroy (1993), Geometry of patchy snowcovers, *proceedings, 50th Annual Eastern Snow Conference,* Quebec, QC, 89-98.

Smith, C. D., Kontu, A., Laffin, R., and J. W. Pomeroy (2017), An assessment of two automated snow water equivalent instruments during the WMO Solid Precipitation Intercomparison Experiment,*The Cryosphere*, 11, 101-116, doi:15194/tc-11-101-2017.

Tekeli, A., Sorman, A., Sensoy, A., Sorman, A., Bonta, J., and G. Schaefer (2005), Snowmelt lysimeters for real-time snowmelt studies in Turkey. *Turkish J. Eng. Env. Sci.*, 29, 29-4.

Thompson, S. S., Kulessa, B., Essery, R. L. H., and M. P. Lüthi (2016), Bulk meltwater flow and liquid water content of snowpacks mapped using the electrical self-potential (SP) method, *The Cryosphere*, 10, 433-444, https://doi.org/15194/tc-10-433-2016.

Waldner, P., Schneebeli, M., Schultze-Zimmermann, U., and H. Flühler (2004), Effect of snow structure on water flow and solute transport, *Hydrological Processes*, 18 (7), 1271–129

Wever, N., Fierz, C., Mitterer, C., Hirashima, H., and M. Lehning (2014), Solving Richards equation for snow improves snowpack meltwater runoff estimations in detailed multi-layer snowpack model, *The Cryosphere*, 8, 257-274, doi:15194/tc-8-257-2014.

Wever, N., Schmid, L., Heilig, A., Eisen, O., Fierz, C., and M. Lehning (2015), Verification of the multi-layer SNOWPACK model with different water transport schemes, *The Cryosphere*, 9, 2271-2293, doi:15194/tcd-9-2271-2015.

Williams, M. W., T. a. Erickson, and J. L. Petrzelka (2010), Visualizing meltwater flow through snow at the centimetre-to-metre scale using a snow guillotine, *Hydrol. Process.*, *2110*(April), n/a–n/a, doi:11002/hyp.763.

Würzer, S., Wever, N., Juras, R., Lehning, M., and T. Jonas (2017), Modelling liquid water transport in snow under rain-on-snow conditions – considering preferential flow, *Hydrol. Earth. Syst. Sci.*, 21, 1741-1756, doi:15194/hess-21-1741-2017.

CHAPTER 5

SIMULATION OF CAPILLARY OVERSHOOT IN SNOW [3]

Abstract

The timing and magnitude of snowmelt discharge and subsequent runoff are controlled by both matrix and preferential flows of water through snowpacks. Matrix flow can be estimated using the Richards equation and, recently, preferential flow in snowpacks has been represented in 2D and 3D models. A challenge for representing preferential flow through porous media is capillary overshoot, and soil studies have developed sophisticated and largely realistic approaches to represent this, but it has not been addressed in snowpack water flow models. Here, a 1D non-equilibrium Richards equation model is implemented with dynamic capillary pressure and is then combined with a new concept of entrapment of liquid water within the pore space. This new model was capable of quantitatively simulating capillary overshoot, as estimated by published capillary pressure measurements in snow samples of various grain sizes under different rates of liquid water infiltration. Three model parameters were calibrated and their impacts on model outputs were evaluated. This improvement is a substantial step towards better understanding and simulating physical processes occurring while liquid water percolates an initially dry snowpack.

[3] Leroux, N.R., and J.W. Pomeroy (2018), Simulation of capillary overshoot in snow combining trapping of the wetting phase with a non-equilibrium Richards equation model, under review in *Water Resources Research*. Nicolas Leroux is the lead author and investigator of this manuscript. John Pomeroy provided assistance with conceptualization, editorial assistance and discussion of the results.

5.1 Introduction

During snowmelt and rain-on-snow events, the timing and magnitude of runoff at the base of a snowpack are primary controlled by infiltration of water through snow (*Horton*, 1915; *Colbeck*, 1972; *Wankiewicz*, 1979). Understanding water flow through snow is not only crucial to better predicting cold regions hydrology, it is also an important factor in triggering wet snow avalanches (e.g. *Kattelman*, 1984; *Wever et al.,* 2016). Under a warming climate, slower and earlier snowmelt is forecast (*Rauscher et al.*, 2008; *Lopez Moreno et al.*, 2017; *Pomeroy et al.*, 2015; *Musselman et al.*, 2017) and the number of rain-on-snow events, sometimes causing extreme flooding (*Pomeroy et al.*, 2016), is expected to increase (*Cohen et al.*, 2015). Accurately predicting the timing and amount of snowmelt runoff is critical to better forecasting of extreme melt events.

Preferential flow paths in snow have been widely documented in experimental studies (*Marsh and Woo*, 1984; *Schneebeli*, 1995; *Waldner et al.*, 2004; *Katsushima et al.*, 2013; *Avanzi et al.*, 2016). Preferential flow in snow accelerates the infiltration of water, which bypass zones in the snowpack that remain dry and cold (*Marsh and Woo*, 1984; *Marsh*, 1991). Only recently, multi-dimensional numerical models were developed to simulate the formation and propagation of preferential flow in snow (*Hirashima et al.*, 2014, 2017; *Leroux and Pomeroy*, 2017). In these models, water entry pressure, that is "the water pressure that is required for water to enter a new region of the pore space" (*DiCarlo*, 2010), was used to estimate the water pressure in air-dry snow, i.e. when the water content was initially below its residual value. These models simulated capillary overshoots in snow, but the predicted values failed to mimic laboratory experiments with artificial snow samples (*Katsushima et al.*, 2013). In particular, the model of *Hirashima et al.* (2014) greatly overestimated capillary pressure, most likely because capillary hysteresis was neglected (*Leroux and Pomeroy*, 2017). The pore processes that cause hysteresis also impact the width and length of preferential flow paths (*Leroux and Pomeroy*, 2017). Despite these improvements in modeling water flow through snow, the use of capillary entry pressure for dry snow contradicts the hydrophilic nature of ice. Indeed, water entry pressure represents the repellency between dry snow and liquid water. Dry snow is, however, expected to be hydrophilic due to the existence of a thin layer of liquid water around the ice grains (*Dash et al.*, 1995, 2006) and a small contact angle of water on ice (~12^{o}) (*Knight*, 1967). Thus, introducing water entry pressure for dry snow in

Richards equation results in capillary overshoot and preferential flow paths, and its implementation in a numerical model is based on a physically inaccurate concept.

Capillary pressure overshoot and saturation overshoot have been observed in soil (*Glass and Nicholl*, 1996; *Bauters et al.*, 1998, 2000; *DiCarlo*, 2004). Saturation and pressure overshoots were found to be the reason for unstable flow (*Eliassi and Glass*, 2001; *DiCarlo*, 2013), but unstable flow cannot be represented by solutions of the standard Richards equation, which are unconditionally stable (*Egorov et al.*, 2003). Different extensions to the Richards equation have been proposed to simulate the hold-back behaviour in saturation observed at the tips of the preferential flow paths (summarized in *DiCarlo* (2005, 2010, 2013)). *Hassanizadeh and Gray* (1993) suggested adding a dynamic term in the capillary pressure equation to account for the relaxation mechanism between water saturation and water pressure. The use of a dynamic capillary pressure in the Richards equation allowed for the simulation of saturation and pressure overshoots in 1D models, as well as unstable flows in 2D and 3D models (*Nieber et al.*, 2003; *DiCarlo*, 2005; *Sander et al.*, 2008; *Chapwanya and Stockie*, 2010; *Zhang and Zegeling*, 2017). *DiCarlo* (2010) noted that the capillary pressure and saturation at the tip of a flow finger followed a dynamic (transient) capillary wetting curve that matched the static capillary pressure wetting curve, i.e. the curve relating the capillary pressure and the saturation of the wetting phase at equilibrium during a wetting process. Therefore, applying a dynamic capillary pressure to simulate capillary pressure overshoot and preferential flow in snow should be more appropriate than using a single-value water entry pressure when the media is initially dry. This is demonstrated here.

Where water flow is estimated using the Richards equation in snowpack models, constant values of residual water content have often been applied, neglecting the potential impact of snow properties on this parameter (*Jordan*, 1983; *Illangasekare et al.*, 1990; *Daanen and Nieber*, 2009; *Wever et al.*, 2014; *Leroux and Pomeroy*, 2017; *D'Amboise et al.*, 2017). The values of the volumetric residual water content used in snowpack models were determined during drainage experiments using small snow samples (*Yamaguchi et al.*, 2010; *Katsushima et al.*, 2013). Prior to the first snowmelt, the temperature of a snowpack is below freezing with no liquid water present within the pore space (outside of the thin fluid of liquid water existing around the snow grains). Thus, the residual value for the first wetting process should be zero.

Pragmatic strategies were used in snow models to determine residual water content in wetting snow layers that were initially air-dry (*Wever et al.*, 2014; *D'Amboise et al.*, 2017). These methods can be seen as simple trapping models that determine the amount of isolated liquid water within the pore space as a function of available liquid water. This is analogous to trapping of the non-wetting phase in soil petroleum engineering (*Land*, 1968; *Lenhard and Parker*, 1987), where the trapped non-wetting phase (usually oil or gas) is extracted from the porous medium by a moving wetting phase (usually water). *Land* (1968) developed a model to estimate residual saturation of a non-wetting phase as a function of the initial saturation of the non-wetting phase. *Land* (1968) separated the non-wetting fluid into a mobile fluid and a trapped fluid. A trapping model to estimate residual saturation of the wetting phase that can be combined with a hysteretic water retention curve in snow is introduced here.

In this study, a 1D numerical model to simulate water flow through snow that addresses the two gaps in the literature is presented. A dynamic capillary pressure is included in the Richards equation to simulate capillary overshoot in snow. This new non-equilibrium Richards equation model also incorporates a new water retention model, including a method for estimating residual water content in wetting snow layers that are initially air-dry. In addition, this model is compared to published data and sensitivity of model outputs on model parameters is examined.

5.2 Theory

To simulate the vertical flow of liquid water in snow, the 1D Richards equation is solved:

$$\frac{\partial \theta_{\mathrm{w}}}{\partial t} = \frac{\partial}{\partial z}\left(k_{\mathrm{rw}}(\theta_{\mathrm{w}})K_{\mathrm{s}}\frac{\partial P_{\mathrm{c}}(\theta_{\mathrm{w}})}{\partial z}\right) - \frac{\partial}{\partial z}(k_{\mathrm{rw}}(\theta_{\mathrm{w}})K_{\mathrm{s}}), \tag{5.1}$$

where θ_{w} is the volumetric water content [$\mathrm{m^3\ m^{-3}}$], $k_{\mathrm{rw}}(\theta_{\mathrm{w}})$ is the relative permeability [-] (c.f. Section 5.2.2), K_{s} is the saturated hydraulic conductivity [$\mathrm{m\ s^{-1}}$] and $P_{\mathrm{c}}(\theta_{\mathrm{w}})$ is the static capillary pressure [unit head] (c.f. Section 5.2.1). In this study, saturation is defined as $S_{\mathrm{w}} = \theta_{\mathrm{w}}/\theta_{\mathrm{ws}}$, where θ_{ws} is the volumetric water content at saturation.

Prior to the first snowmelt or rain-on-snow event, the pores within a snowpack are air-dry, i.e. no liquid water is present. In the present study, the contribution of liquid water from the thin film surrounding the ice grains to bulk water content at macroscale is neglected. For initially dry snow, *Hirashima et al*. (2014) used constant water entry pressure in their model until the water saturation

reached a residual saturation value, S_{wr}, after which the capillary pressure was estimated from the drainage water retention curve. The various values of volumetric residual water content, θ_{wr}, measured for snow, ranging between 0.018 m^3 m^{-3} and 0.04 m^3 m^{-3} (e.g. *Yamaguchi et al.*, 2010; *Katsushima et al.*, 2013) were determined by draining snow samples initially fully saturated until only the water held by capillary forces remained in the pores (e.g *Yamaguchi et al.*, 2010; *Katsushima et al*., 2013). These published values of S_{wr} correspond to maximum residual saturations on the drainage curve, hereby called $S_{\mathrm{wr}}^{\max}$.

A new water retention curve in snow that can be applied from initially dry to fully saturated snow for both wetting and draining processes is introduced here. The main wetting and the main drainage curves start at $S_{\mathrm{w}} = S_{\mathrm{wr}} = 0$ and $S_{\mathrm{w}} = S_{\mathrm{wr}}^{\max}$, respectively. The trapping model of *Land* (1968) is adapted to account for entrapment of the wetting phase by using saturation of the reversal point between wetting and drainage, in contrast to entrapment of the non-wetting phase for which it was developed. This modified model is used to determine residual saturation of the wetting phase ($S_{\mathrm{wr}} \in [0, S_{\mathrm{wr}}^{\max}]$) based on saturation of the reversal point (S_{id}^{Δ}) when the process switches from wetting to drainage:

$$S_{\mathrm{wr}} = \frac{S_{\mathrm{id}}^{\Delta}}{1 + C S_{\mathrm{id}}^{\Delta}}, \tag{5.2}$$

with $C = \frac{1}{S_{\mathrm{wr}}^{\max}} - 1$.

5.2.1 Water Retention Curve

The relationship between static capillary pressure (P_{cs} in Eq. 5.1) and saturation of the wetting phase, i.e. the water retention curve includes a main wetting curve initiating at $S_{\mathrm{w}} = 0$, a main draining curve starting at $S_{\mathrm{w}} = S_{\mathrm{wr}}^{\max}$, as well as drying and wetting scanning curves. From this point, the superscripts i and d represent the wetting and draining modes of parameters. The main wetting and drying curves are estimated using the van Genuchten model (*van Genuchten*, 1980):

$$P_{\mathrm{c}} = \frac{1}{\alpha^j} \left(\left(\frac{\theta_{\mathrm{w}}^j - \theta_{\mathrm{wr}}^j}{\theta_{\mathrm{ws}} - \theta_{\mathrm{wr}}^j} \right)^{-\frac{1}{m^j}} - 1 \right)^{1/n^j}, \text{ with } m^j = 1 - 1/n^j \tag{5.3}$$

where θ_{ws} is the water content at saturation [m^{-3} m^{-3}], α [m-1], n^j and m^j are parameters, and $j \in \{w, d\}$. The van Genuchten parameters α^w and n^w for the main wetting curve are scaled from the

parameters of the main draining curve (α^d and n^d) according to the method of *Kool and Parker* (1987), i.e. $n^{\mathrm{w}} = n^{\mathrm{d}}$ and $\alpha^{\mathrm{w}} = \gamma\alpha^{\mathrm{d}}$, with γ usually taken equal to 2. In snow, parametric equations for α^{d} and n^{d} exist, relating these parameters to snow grain size and dry density.

The scanning curves are simulated according to the model of *Huang et al.* (2005). The scanning curves are forced to pass through the reversal points on the main wetting and drainage curves to obtain closure of the loops, thus preventing artificial pumping errors (*Werner and Lockington*, 2006). The water content on each scanning is estimated by fitting the van Genuchten model to pass through the two reversal points on each main curve, which are known.

Figure 5.1a presents an example of the water retention curve for α^d = 10 m^{-1}, n^d = 10, θ_{ws} = 0.6, $\gamma = 2$ and $\theta_{\mathrm{wr}}^{\max}$ = 0.02 (values similar to the observations of *Katsushima et al.*, 2010). The main wetting and drainage curves started at two different residual saturations (S_{wr}= 0 and S_{wr}= $S_{\mathrm{wr}}^{\max}$, respectively), while the drying scanning curve that initiated from the main wetting curve (black dot in Fig. 5.1a) had a residual saturation calculated from Eq. 5.2.

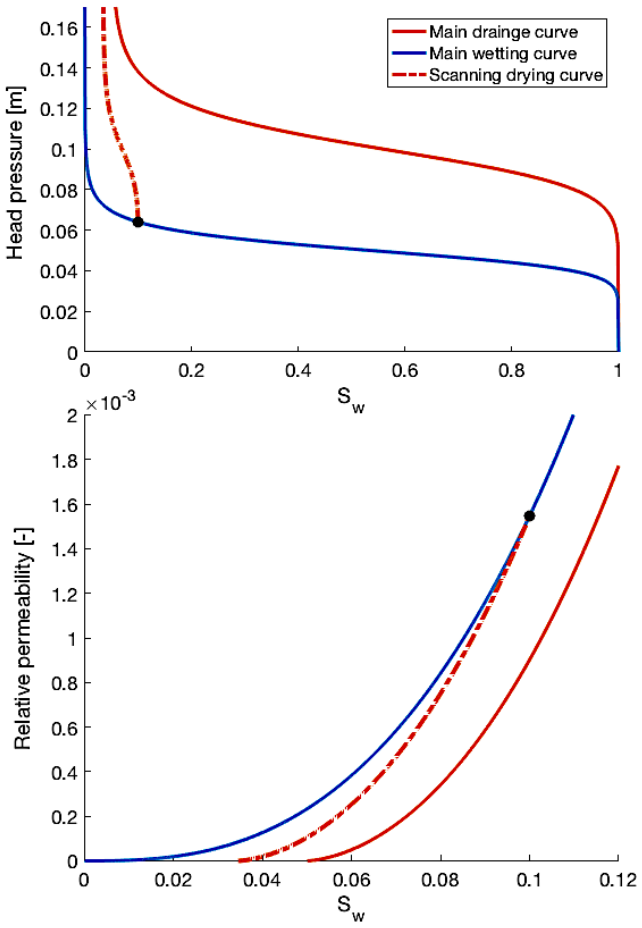

Figure 5.1 a) Example of a water retention curve for α^d = 10 m^{-1}, n^d = 10 and $\theta_{\mathrm{wr}}^{\max}$ = 02 (values similar to those measured by *Katsushima et al.* (2013)). The black dot represents the reversal point from the main wetting curve to the drying scanning curve at S_{w} = 1. **b**) Example of hysteresis in the relative permeability for the same parameters as in **a)**. The black dot represents the same reversal point as in **a**).

5.2.2 Water Relative Permeability

In a trapping model, a fluid is divided into flowing (mobile) saturation ($S_{\mathrm{w}}^{\mathrm{f}}$) and a trapped (disconnected) saturation ($S_{\mathrm{w}}^{\mathrm{t}}$), such that $S_{\mathrm{w}} = S_{\mathrm{w}}^{\mathrm{t}} + S_{\mathrm{w}}^{\mathrm{f}}$. The model of *Land* (1968) is used to estimate saturation of the flowing fluid as it qualitatively represented the trend observed during wetting in soil (*Joekar-Niasar et al.*, 2013):

$$S_{\mathrm{w}}^{\mathrm{f}} = \frac{1}{2}\left((S_{\mathrm{w}} - S_{\mathrm{wr}}) + \sqrt{(S_{\mathrm{w}} - S_{\mathrm{wr}})^2 + \frac{4}{C}(S_{\mathrm{w}} - S_{\mathrm{wr}})}\right). \tag{5.4}$$

The Mualem-van Genuchten model (*Mualem*, 1974; *van Genuchten*, 1980) is applied to estimate relative permeability of the wetting phase. During the main wetting, relative permeability of the

wetting phase ($k_{\mathrm{rw}}^{\mathrm{w}}$) is a function of the total saturation S_{w}, while the drainage relative permeability of the wetting phase (k_{rw}^{d}) was estimated from Land's model (*Land*, 1968):

$$k_{\mathrm{rw}}^{\mathrm{d}}\left(S_{\mathrm{w}}^{\mathrm{f}}\right) = k_{\mathrm{rw}}^{\mathrm{w}}(S_{\mathrm{w}}) \,. \tag{5.5}$$

Figure 5.1b illustrates an example of hysteresis in relative permeability, resulting from entrapment of the wetting phase. For each flow process, relative permeability follows a unique curve. At a fix water content, relative permeability of the wetting phase is smaller during a drainage process than during wetting because of a reduced flowing saturation during drainage.

5.2.3 Non-Equilibrium Richards Equation Model

Saturation or pressure overshoots cannot be represented when solving the standard Richards equation (*DiCarlo*, 2005; *Eliassi and Glass*, 2001, 2002, 2003). Several extensions have been added to Richards equation to simulate saturation or capillary overshoots in snow or soil. Water entry pressure was previously used to simulate water ponding at the interface between wet and dry snow layers (*Hirashima et al*., 2014; *Leroux and Pomeroy*, 2017). *Hassanizadeh and Gray* (1993) proposed a non-equilibrium model for capillary pressure. They suggested the use of a dynamic capillary pressure (the actual capillary pressure within the pores, $P_{\mathrm{c,d}}$ in unit head) in the Darcy-Buckingham equation:

$$P_{\mathrm{c,d}}(\theta_{\mathrm{w}}) = P_{\mathrm{c}}(\theta_{\mathrm{w}}) - \tau \frac{\partial \theta_{\mathrm{w}}}{\partial t}, \tag{5.6}$$

where τ is a relaxation coefficient [m s]. In soil, capillary pressure and saturation at the front of a preferential flow path form a dynamic wetting curve that matches the main static wetting curve (*DiCarlo*, 2010). Hence, using a dynamic capillary pressure to simulate saturation and capillary overshoots in snow might be more appropriate than using a single-value water entry pressure.

Different models exist to relate the relaxation coefficient τ to the dynamic capillary pressure and saturation (e.g. *Cuesta et al.*, 2000; *Dautov et al*., 2002; *Nieber et al*., 2005). Here, the relaxation coefficient τ is assumed to be a function of the flowing saturation, following the power law relation of *Cuesta et al.* (2000):

$$\tau = \tau_0 \left(S_{\mathrm{w}}^{\mathrm{f}}\right)^{\lambda} , \tag{5.7}$$

where τ_0 [m s] and λ are two constant coefficients to determine. The flowing saturation $S_{\mathrm{w}}^{\mathrm{f}}$ is used in Eq. 5.7 as it remained continuous when the flow process switched from wetting to drainage and a new residual saturation was estimated (Eq. 5.2), as opposed to the effective saturation used in *Cuesta et al.* (2000).

5.3 Numerical Simulations

A one-dimensional model was developed to simulate vertical water flow through snow. The non-equilibrium Richards equation, which includes the trapping and the hysteresis models presented in Section 5.2, was solved using an explicit finite difference method, as presented in *Sander et al.* (2008). An arithmetic average was used to estimate the parameters at the interface of two numerical cells and the time step was smaller or equal to $5\text{x}10^{-4}$ s.

5.3.1 Comparison with Katsushima et al. (2013) Experiments

The model results were compared to the experimental data of *Katsushima et al.* (2013). In their study, *Katsushima et al.* (2013) applied a known water influx (~22 mm h^{-1}, ~70 mm h^{-1}, and ~ 200 mm h^{-1}) at the surface of snow samples of similar density but different grain sizes (from finest to coarsest snow sample, the snow samples are named: SM, SL and SLL). The snow samples were each 27 cm high and 5 cm wide and their density and grain size were recorded prior to the infiltration experiments. The physical properties (density and grain size) of the snow samples are summarized in Table 5.1. In the model, the 27 cm tall snow columns were uniformly discretized into 108 vertical numerical cells (each 0.25 cm thick). Drainage water retention curves were also measured for each snow sample, and the van Genuchten model was fitted to the data to obtain the parameters $\theta_{\mathrm{wr}}^{\mathrm{max}}$, the water content at saturation θ_{ws}, and α^{d} and n^{d}. In addition, the hydraulic conductivity (K_{s}) of each snow sample was determined. These parameters (summarized in Table 5.1) were directly applied in the model, as well as the known influx at the snow surface. The main wetting curve and the scanning curves were estimated as detailed in Section 5.2.1. Free-drainage was chosen as lower boundary condition. During the experiments, the upper two centimetres of the snow samples were initially wet at $\theta_{\mathrm{w}} = \theta_{\mathrm{wr}}^{\mathrm{max}}$, while the rest of the snow sample was initially air-dry ($\theta_{\mathrm{w}} = 0$). To avoid numerical divergence in the model, the water content profile in each snow sample was initialized as follow:

$$\theta_{\mathrm{w}} = \begin{cases} \theta_{\mathrm{wr}}^{\max} + \epsilon & \text{if } z \geq 25 \text{ cm} \\ 0 + \epsilon & \text{if } z < 25 \text{ cm} \end{cases} \quad \text{with } \epsilon = 10^{-3}.$$

As the wet snow was obtained from drainage experiments after equilibrium was reached in the model, for $z \geq 25$ cm, the pressure was initialized on the main drainage curve, while it was on the main wetting curve for the rest of the snow sample ($z < 25$ cm).

Table 5.1 Summary of the snow properties and model parameters.

Snow sample	Mean grain size [mm]	Mean density [kg m^{-3}]	K_{s} [m hr^{-1}]	θ_{ws}	$\theta_{\mathrm{wr}}^{\max}$	α^d [m^{-1}]	n^d
SLL	1.439	498	19.34	368	039	16.3	9.48
SL	1.049	511	5.9	353	038	11	13.95
SM	421	483	3.18	420	040	6.1	14.54

During the infiltration experiments, *Katsushima et al.* (2013) measured capillary pressure with a tensiometer at the interface between wet and dry snow (at 25 cm < z < 25.6 cm). Due to the short time scale and the transient nature of the experiments, the pressure measured at the interface is the dynamic capillary pressure within the snow. At this interface, capillary overshoots were observed for all three snow samples (SM, SL, and SLL) at all three different input fluxes. In the snow sample SS used in the study by *Katsuhima et al.* (2013), capillary overshoot was not observed. Therefore, this snow sample is disregarded in this analysis. In most experiments, the capillary pressure overshoot was greater for finer snow. An analysis of the capillary pressure measurements showed that the time at which minimum pressure was reached was longer for decreasing grain size and was shorter with increasing input flux.

The simulated capillary pressures at the wet to dry interface with the non-equilibrium Richards equation model was compared to the capillary pressure observations of *Katsushima et al*. (2013). Initial simulations were run to observe the ability of the model to represent capillary pressure overshoot. The three model parameters τ_0, γ, and λ were manually varied to match the observations. A more detailed sensitivity analysis, showing the impact of each parameter on the model response, is presented in Section 5.3.3.

Water infiltration through the three snow samples was simulated under the three different water influxes. The effect of the relaxation coefficient τ for different snow grain sizes is first evaluated by holding λ constant at 0 and varying τ_0 and γ. As expected, the results from the standard Richards equation (no capillary overshoot) were reproduced for $\tau = 0$. Figure 5.2 presents the simulated capillary pressures at the wet to dry snow interface compared to observations for the three snow samples SLL, SLL and SM (left to right figures, respectively) with the three different water influxes (increasing influx from top to bottom figures). The values of the two parameters $\{\tau_0,\gamma\}$ for all 9 simulations are summarized in Table 5.2 ($\lambda = 0$). γ was observed to primarily impact the simulated value of minimum pressure and τ_0 controlled the value of pressure at steady state. For the snow sample SM, γ dramatically increased with input flux, while it only slightly increased for the other two snow samples. In all snow samples, τ_0 decreased for increasing input fluxes. For decreasing grain size, τ_0 and γ respectively increased and decreased to successfully represent the increase of capillary overshoot observed in the data. The magnitudes of capillary pressure overshoot were well represented in the model. The biases between individual simulated and observed values of minimum pressure and pressure at steady state were less than 1 % (Fig. 5.2). For most of the simulations, the timing of the modeled capillary pressure failed to reproduce observations. The modeled minimum capillary pressure and modeled steady state were reached slightly prior to and later than the observed times, respectively. For all simulations, the minimum pressure was reached when the water content was maximum (not shown).

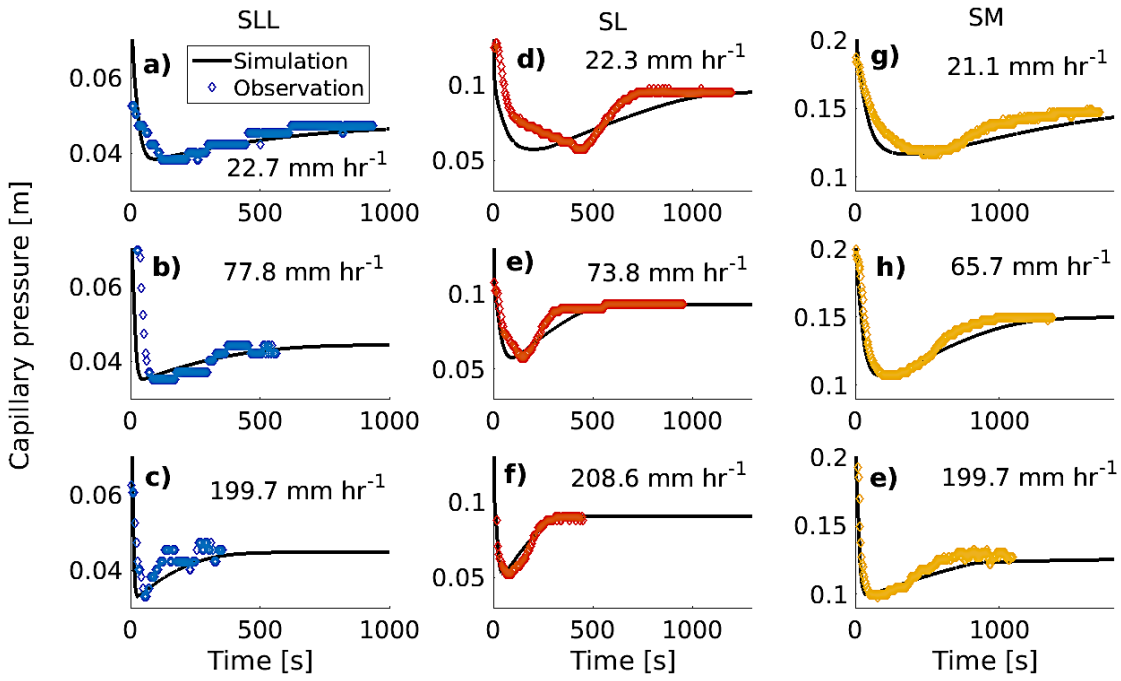

Figure 5.2 Simulated (black lines) and observed (coloured diamonds) capillary pressures for three different snow samples (from left to right columns, coarse to finer snow: SLL, SL, and SM) at three different input fluxes (lower to higher fluxes from top to bottom of graphs). For all simulations, λ was equal to 0 and the values of the coefficients τ_0 and γ are as summarized in Table 5.2.

Table 5.2 Parameters $\{\tau_0,\gamma\}$ for the Snow Samples SLL, SL, and SM and Three Different Input Fluxes (λ=0).

	SLL			SL			SM		
Flux [mm hr^{-1}]	22.7	77.8	199.7	22.3	73.8	208.6	21.1	65.7	195.3
τ_0 [m s]	1.3	0.25	0.12	15	4.2	1.1	20	6	0.75
γ	2.16	2.23	2.23	1.9	1.82	1.92	1.57	1.62	1.72

The impact of λ on simulated capillary pressure was also investigated. Figure 5.3 shows the simulated capillary pressure in the snow sample SLL under the lower influx for values of λ and τ_0 (shown in Fig. 5.3), with γ fixed at 2.16. Because τ_0 and λ were adjusted to match the observations (with a bias ≤ 1 %), similar results were obtained in the different cases. It was observed that, for increasing λ, the minimum value of capillary pressure. The time and value of capillary pressure at

steady state randomly varied with λ. In addition, as τ_0 was increased with λ to reproduce the observations, these two parameters combined controlled capillary pressure overshoot.

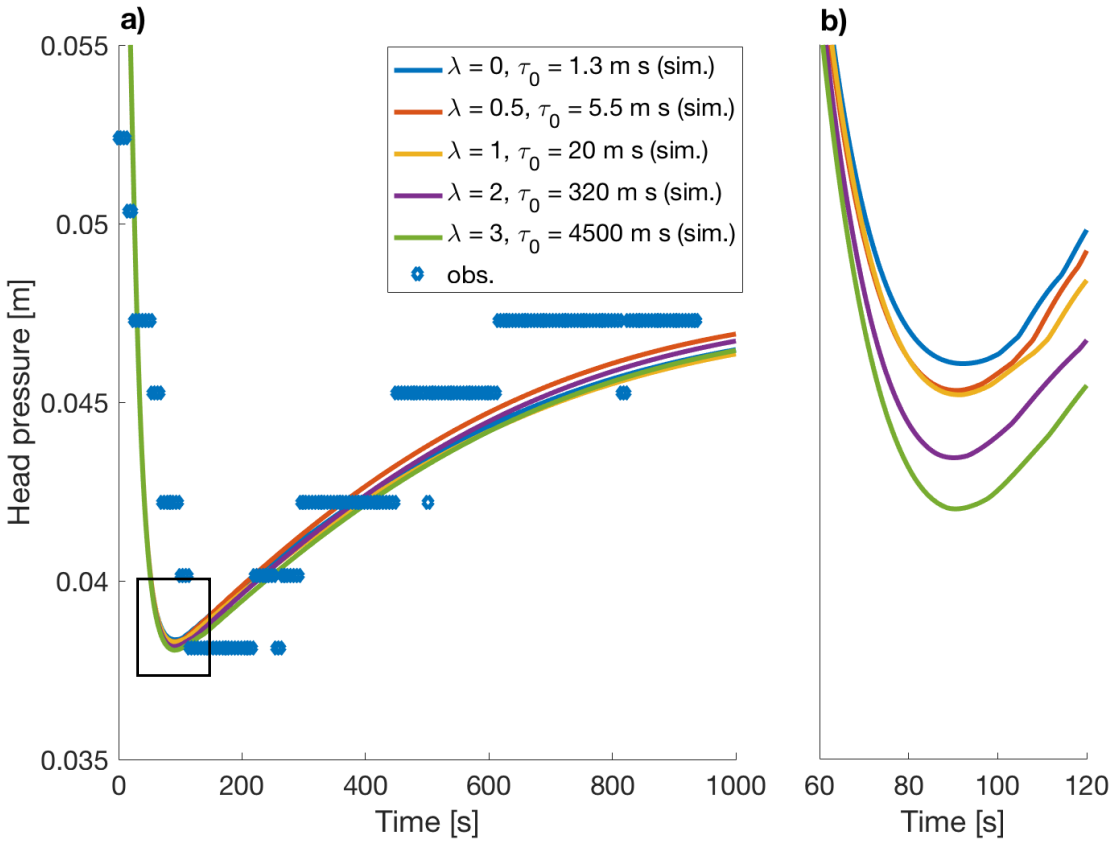

Figure 5.3 a) Simulated capillary pressure through time for different values of λ and τ_0 in the snow sample SLL under an input flux of 22.7 mm hr^{-1}. γ was fixed at 2.16. The blue diamonds represent the measured capillary pressure by Katsushima et al. (2013) for the same snow sample and same input flux. **b**) Simulated capillary pressures for the same conditions as in **a**) from 50 s and 150 s (zoomed in from the black box in **a**))

5.3.2 Saturation Overshoot in Snow

Water content distribution simulated within the three snow samples for the three different input fluxes was examined. Water content distribution within the three snow samples for the lower input flux (~20 mm hr^{-1}) at 1000 s, 1800 s, and 3000 s for the snow samples SLL, SL, and SM, respectively, are presented in Fig. 5.4. The parameters γ and τ_0 used for these simulations are the same as those from Section 5.3.1 and are presented in Table 5.2, with λ again set at 0. In all snow samples, a peak of saturation was observed at the interface between wet and dry snow, and saturation overshoots were simulated at the wetting fronts. This was expected from using a

dynamic capillary pressure in the Richards equation. For decreasing grain size, the overall simulated water saturation in the snow and the water saturation at the wet to dry snow interface increased and the velocity of the wetting front was slower, due to higher capillary pressure in the pore space. In addition, the saturation overshoot was greater for higher input flux (not shown).

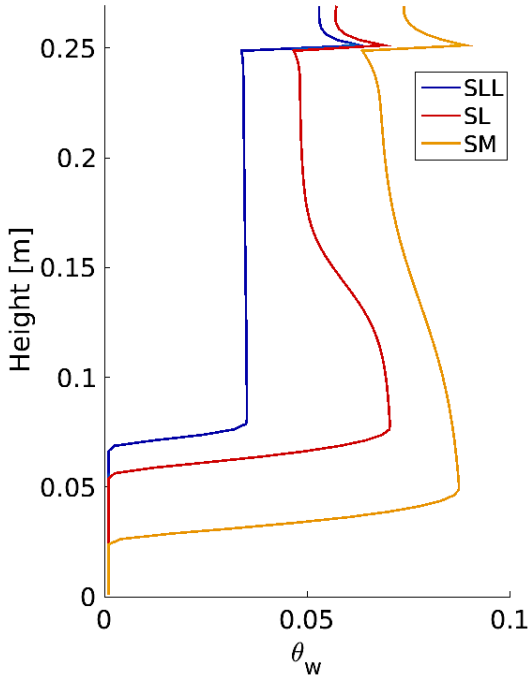

Figure 5.4 Simulated water content distributions within the three snow samples SLL, SL, and SM each at a different time (1000 s, 1800 s, and 3000 s, respectively). The input flux used was ~22 mm hr^{-1}, λ was chosen equal to 0, γ was equal to 2.16, 1.9, and 1.57 and τ_0 equal to 1.3 m s, 15 m s, and 20 m s for the snow samples SLL, SL, and SM, respectively.

5.3.3 Sensitivity of Model Parameters

The three model parameters (τ_0, λ, and γ) impact the timing and magnitude of minimum capillary pressure, and the values of pressure at steady state. The sensitivity analysis was conducted using the snow sample SLL under the lowest input flux (22.7 mm hr^{-1}). This snow sample was chosen because it presented the lowest values of τ_0 in Section 5.3.1 (Table 5.2). Thus, a narrower range of τ_0 values was necessary in the sensitivity analysis to correctly quantify the impact of this parameter on model outputs, using less iteration and less CPU time to conduct the sensitivity analysis than using the other snow samples. The results of the sensitivity analysis in the other snow

samples is expected to be comparable, as the model parameters behaved similarly during the manual calibration in Section 5.3.1.

Values of τ_0 and λ for snow are unknown. From Section 5.3.1, capillary pressure overshoot in SLL under the lowest water influx was well represented for $\tau_0 \in [1.3,320]$, $\lambda \in [0,2]$, and $\gamma = 2.16$. From these initial results, the three input parameters in the sensitivity analysis were chosen to vary as follow: $\tau_0 \in [1,350]$ m s^1, $\gamma \in [1.5, 2.5]$, and $\lambda \in [0, 2]$. The VARS toolbox (*Razavi and Gupta*, 2016a, 2016b) was used to create an input file for the sensitivity analysis and analyze the model behaviors. Based on a "star-based" sampling strategy, VARS creates the samples for the sensitivity analysis from the factor space of each parameter. The 1D non-equilibrium Richards equation model was then run with each sample (each containing values for the set $\{\tau_0, \lambda, \gamma\}$) The input coefficients in the VARS toolbox were kept to their default values, resulting in a total number of model runs (number of samples) equal to 560. VARS was then applied to analyze the model responses, i.e. the biases between each of the three model outputs and their corresponding value in the observations, to each sample. The sensitivity of a model response to each factor was determined using the Integrated Variogram Across a Range of Scales (IVARS) over a range between 0 and 10 % ($IVARS_{10}$), between 0 and 30 % ($IVARS_{30}$), and between 0 and 50 % ($IVARS_{50}$) as suggested by *Razavi and Gupta* (2016a).

Figure 5.5 presents the normalized $IVARS_{50}$ value of each parameter plotted for the three model responses; results from other IVARS metrics were similar. Some capillary pressure distributions presented one oscillation before reaching steady state at high values of τ (high τ_0 and small λ). These solutions were included in the sensitivity analysis. When including the parameter λ in the model, γ had less effects on the value of minimum pressure and barely impacted the other two model outputs. The parameter λ affected the value of minimum pressure (blue color) and the pressure at steady state (yellow color) the most and τ_0 had the main influence on the time at which minimum pressure was reached (orange color). However, the 90 % confidence intervals for the time of minimum pressure and the pressure at steady state for the parameters τ_0 and λ were wide. Therefore, the two parameters τ_0 and λ each had great impact on both the timing of minimum pressure and the pressure at steady state.

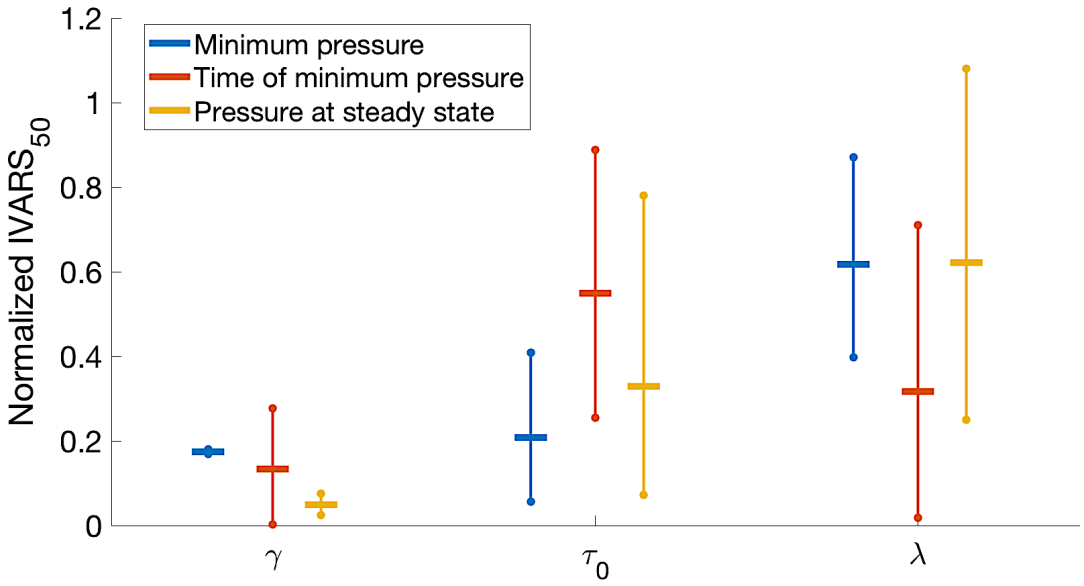

Figure 5.5 . Normalized $IVARS_{50}$ values for the model parameters γ, τ_0, and λ for three different model outputs: values of minimum capillary pressure (blue), time at which minimum pressure was reached (red) and value of capillary pressure at steady state (yellow). The colored dots present the values of the 90 % confidence intervals. The $IVARS_{50}$ values are normalized so that, for each model output (color on the graph), the sum of $IVARS_{50}$ for the parameters γ, τ_0, and, λ equals 1.

5.4 Discussion

The new 1D non-equilibrium Richards equation model presented here was able to quantitatively represent capillary overshoots observed in different snow samples by *Katsushima et al.* (2013). This model differs from previous numerical studies (*Hirashima et al.*, 2014; *Leroux and Pomeroy*, 2017) that used capillary entry pressure for air-dry snow to simulate capillary pressure overshoot in snow. The use of a single-value capillary pressure to estimate capillary pressure at the tip of a preferential flow path is not accurate (*Dicarlo*, 2010). Figure 5.6 shows a qualitative comparison of the simulated capillary pressures from this study (black line) against the model results from *Leroux and Pomeroy* (2017) (dashed line). The results from the 1D non-equilibrium Richards equation model were closer to the observations than the model using capillary entry pressure (*Leroux and Pomeroy*, 2017). As expected when considering a dynamic capillary pressure, saturation overshoots at the wetting fronts were also represented in all snow samples when $\tau > 0$. This is in accordance with other non-equilibrium Richards equation models that simulate water infiltration in soil (e.g. *Nieber et al.*, 2002; *DiCarlo*, 2005; *Sander et al.*, 2008; *Zhang and*

Zegeling, 2017). The estimated water content was higher for larger influx and for smaller grain sizes due to a higher capillary pressure within the pores. The simulated water content (up to 9 %) was within the range of observed values in other snow samples with similar grain sizes and densities (*Waldner et al.*, 2004; *Avanzi et al.*, 2016).

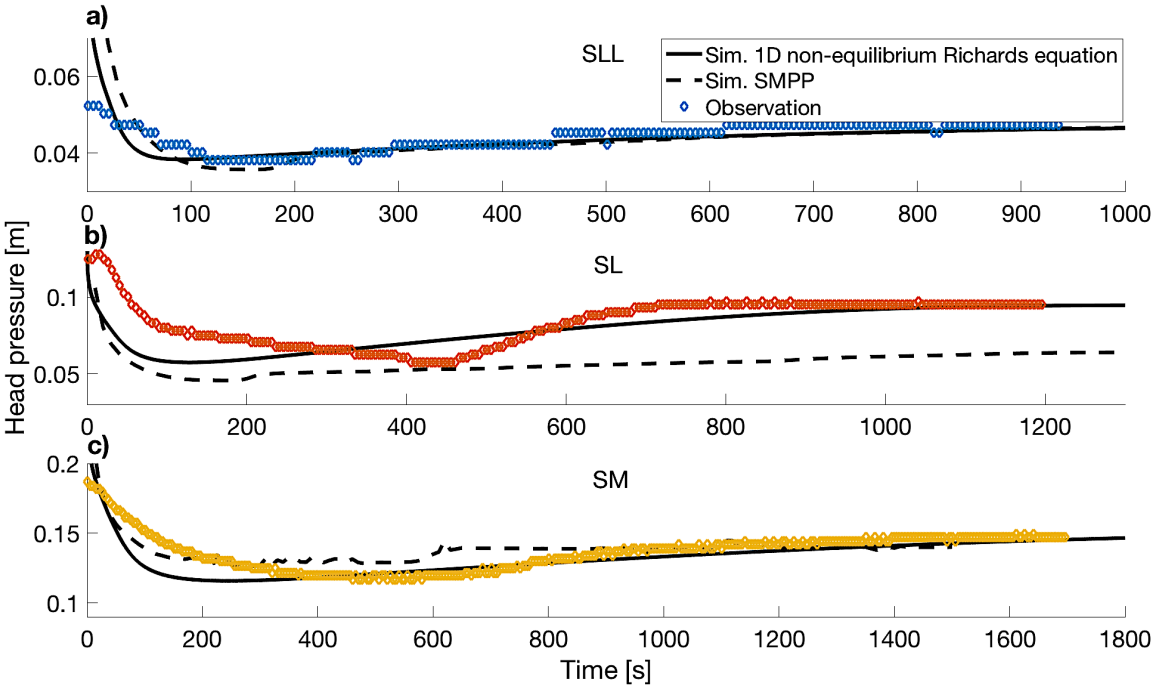

Figure 5.6 Comparison of simulated capillary pressure at the interface between wet to dry snow for the three snow samples SLL (**a**), SL (**b**), and SM (**c**). The black line represents the results from the 1D non-equilibrium Richards equation model introduced in this study, the purple line presents the results from the model SMPP (*Leroux and Pomeroy*, 2017), and the colored diamonds are the observations of *Katsushima et al*. (2013).

The 1D model was compared to 3D data and so care must be taken in such an evaluation. As the data from *Katsushima et al*. (2013) are qualitatively similar to 1D overshoot profiles measured in soil (e.g. *DiCarlo*, 2007), they were deemed to be suitable for comparison with the 1D model. After adjusting three model parameters (τ_0, γ, and λ), the model accurately reproduced the capillary overshoots observed during the snow experiments. The short transition between the minimum pressure and the pressure at steady state from the experiments resulted from a fast percolation of the liquid water into the lower layer due to preferential flow paths. By collecting 1D vertical flow through snow data, this model could be better parameterized. This could be done by conducting experiments similar to *Katsushima et al.* (2013) but using tube samples of diameters

smaller than the lateral extent of preferential flow paths, so such flow paths cannot form (*DiCarlo*, 2010).

The relaxation coefficient τ symbolizes the rate of redistribution of the wetting phase within the pores (*DiCarlo*, 2013). For finer snow samples (smaller grain sizes), higher values of τ were necessary to represent the measured capillary overshoots. This was also observed in soil by *Camps-Roach et al.* (2010). This might be caused by stronger capillary pressure within smaller pores slowing down the redistribution of liquid water within the pores. Additionally, τ decreased for increasing input fluxes, as less time would be required for the water to be redistributed within the pore space. The present study, through comparisons with data from *Katsushima et al.* (2013), provides some initial understanding of the relaxation coefficient (τ) for different snow grain sizes and input fluxes. However, incorporating this model into operational snowmelt models requires a better understanding of how τ varies for different densities and a parameterization of τ_0 as a function of snow properties.

Many models have been developed to estimate capillary or saturation overshoot in soil, as well as 2D or 3D unstable flow (*Nieber et al*., 2003; *Sander et al.,* 2008; *Chapwanya and Stockie*, 2010; *Zhang and Zegeling*, 2017). Including capillary hysteresis in these models has proven to suppress oscillations in simulated capillary pressure (*Sander et al*., 2008). Oscillations in the present model were obtained only for very high values of τ (values of an order of magnitude larger than those on Fig. 5.3) in the sensitivity analysis (Section 5.3.3). As the main wetting curve was scaled from the main drainage curve through the parameter γ, its impact on simulated capillary pressure overshoots was evaluated. This research shows that γ had, however, little impact on the model outputs (Section 5.3.3). From the analysis in Section 5.3.1, γ was smaller for finer grain size, as previously observed by *Likos et al.* (2013) during soil experiments.

More experiments in natural snowpacks under controlled conditions are required to better understand and estimate the parameters introduced in this study (τ, λ, and γ), as well as to validate the applicability of Land's model (*Land*, 1968) for estimating residual water saturation (Eq. 5.2). An experiment similar to *Camps-Roach et al*. (2010) should be conducted using different snow samples to investigate τ dynamics through measurements of both dynamic and static curves. Because the snowpack matrix evolves under a thermal gradient and the presence of liquid water,

pore-scale modeling of two-phase flow through snow can be a tool to improve the understanding of hysteresis in the relative permeability of the wetting phase in snow, as well as the suitability of different trapping model to estimate residual saturation in snow, as has been done for soil (e.g. *Spiteri et al.*, 2005; *Joekar-Niasar et al.*, 2013).

The impact of refreezing of liquid water within the pore space (*Humphrey et al.*, 2012) and snow metamorphism (*Colbeck*, 1982, 1998; *Brun*, 1989) on capillary pressure in snow has yet to be studied. Water flow through snow, and thus the forecasting ability of snowmelt models, would greatly benefit from better estimates of capillary pressure within the snow pore during melting, refreezing, and metamorphism processes.

5.5 Conclusions

A new water retention model for snow, combining a trapping model for the wetting phase, was presented. When compared to previously published experiment data, capillary pressure overshoot in snow was properly represented using dynamic capillary pressure in the Richards equation. The use of dynamic capillary pressure in snow, instead of a single-value water entry pressure for dry snow (*Hirashima et al*., 2014, 2017; *Leroux and Pomeroy*, 2017), was motivated by experimental findings in soil studies (*DiCarlo*, 2010) showing that capillary pressure at the tip of a preferential flow path follows a dynamic capillary pressure curve similar to the static wetting curve. A relaxation coefficient was introduced that symbolizes dynamic effects at pore scale. The behavior of the relaxation coefficient for different grain sizes and under various water influxes is in accordance with soil studies and helps better understand the non-equilibrium process of water flow through porous media.

In soil, capillary overshoot proved to be the cause of unstable flow in multi-dimensional models. Therefore, a future study should consider upscaling this 1D non-equilibrium Richards equation model to simulate formation and propagation of preferential flow paths through snow. This research provides initial values for the model parameters that could be used in a multi-dimensional model. These model parameters varied with grain size. Parametric relationships are therefore needed to relate the parameters to snow density and grain size, and these relationships would be implemented in snowmelt models that forecast meltwater runoff.

Key Points for the Next Chapter

- In order to implement the new theories in a snow model and validate the water routing scheme with natural snowmelt data using meteorological data, how can the energy balance be improved to limit uncertainties in estimating meltwater flow through snow?
- Can a missing flux within snowpacks improve the estimation of snow surface temperature, which is one of the main drivers of the energy balance?

5.6 References

Avanzi, F., Hirashima, H., Yamaguchi, S., Katsushima, T. and De Michele, C. (2016), Observations of capillary barriers and preferential flow in layered snow during cold laboratory experiments, *The Cryosphere*, 10, 2013-2026, doi:10.5194/tc-10-2013-2016.

Bauters, T.W., D.A. DiCarlo, T.S. Steenhuis, and Parlange, J.-Y. (1998), Preferential flow in water-repellent sands, *Soil Science Society of America Journal*, 62(5), 1185–1190.

Bauters, T.W.J., DiCarlo, Steenhuis, T., and Parlange, J.-Y. (2000), Soil water content dependent wetting front characteristics in sands, *Journal of Hydrology*, 231-232, 244–254.

Brun, E. (1989), Investigation on wet-snow metamorphism in respect of liquid-water content, *Annals of Glaciology*, 13, 22-26.

Camps-Roach, G., O'Carroll, D.M., Newson, T.A., Sakaki, T., and Illangasekare, T.H. (2010), Experimental investigation of dynamic effects in capillary pressure: Grain size dependency and upscaling, *Water Resource Research*, 46, W08544, doi:10.1029/2009WR008881.

Chapwanya, M., and Stockie, J.M. (2010), Numerical simulations of gravity-driven fingering in unsaturated porous media using a nonequilibrium model, *Water Resource Research*, 46, W09534, doi:10.1029/2009WR008583.

Cohen, J., Ye, H., and Jones, J. (2015), Trends and variability in rain-on-snow events, *Geophysical Research Letters*, 42, doi:10.1002/2015GL065320

Colbeck, S.C. (1972), A theory of water percolation in snow, *Journal of Glaciology*, 11(63), 369-385.

Colbeck, S.C. (1982), An overview of seasonal snow metamorphism, *Review of Geophysics*, 20(1), 45–61, doi:10.1029/RG020i001p00045.

Colbeck, S.C. (1998), Sintering in a dry snow cover, *Journal of Applied Physics*, 84(8), 4585-4589, doi:10.1063/1.368684.

Cuesta, C., van Duijn, C.J., and Hulshof, J. (2000), Infiltration in porous media with dynamic capillary pressure: travelling waves, *European Journal of Applied Mathematics*, 11:381–397.

Daanen, R.P., and Nieber, J.L. (2009), Model for coupled liquid water flow and heat transport with phase change in a snowpack, *Journal of Cold Regions Engineering*, 23(2), 43–68, doi:10.1061/(ASCE)0887-381X(2009)23:2(43).

D'Amboise, C.J.L., Müller, K., Oxarango, L., Morin, S., and Schuler, T.V. (2017), Implementation of a physically based water percolation routine in the Crocus/SURFEX (V7.3) snowpack model, *Geoscientific Model Development*, 10, 3547-3566, doi:10.5194/gmd-10-3547-2017.

Dash, J.G., Fu, H., and Wettlaufer, J.S. (1995), The premelting of ice and its environmental consequences, Reports on Progress in Physics, 58, 115-167.

Dash, J.G., Rempel, A.W., and Wettlaufer, J.S. (2006), The physics of permelted ice and its geophysical consequences*, Reviews of Modern Physics*, 78 (3), 695-741, doi:10.1103/RevModPhys.78.695.

Dautov, R.Z., Egorov, A.G., Nieber, J.L. and Sheshukov, A.Y. (2002), Simulation of two-dimensional gravity-driven unstable flow, *Developments in Water Science*, 47, 9-16, doi: 10.1016/S0167-5648(02)80039-9

DiCarlo, D.A. (2004), Experimental measurements of saturation overshoot on infiltration, *Water Resources Research*, 40, W04215, doi:10.1029/2003 WR002670.

DiCarlo, D.A. (2005), Modeling observed saturation overshoot with continuum additions to standard unsaturated theory, *Advances in Water Resources*, 28, 1021-1027, doi:10.1016/j.advwatres.2004.12.003.

DiCarlo, D.A. (2007), Capillary pressure overshoot as a function of imbibition flux and initial water content, *Water Resources Research*, 43, W08402, doi:10.1029/2006WR005550.

DiCarlo, D.A. (2010), Can continuum extensions to multiphase flow models describe preferential flow?, *Vadose Zone Journal*, 9, 268-277. doi:10.2136/vzj2009.0099.

DiCarlo, D.A. (2013), Stability of gravity-driven multiphase flow in porous media: 40 Years of advancements, *Water Resources Research*, 49(8), 4531-4544, doi:10.1002/wrcr.20359.

Egorov, M., Dautov, R.Z., Nieber, J.L., and Sheshukov, A.Y. (2003), Stability analysis of gravity-driven infiltration flow, *Water Resources Research*, 39(9), doi:10.1029/2002WR001886.

Eliassi, M., and Glass, R.J. (2001), On the continuum-scale modeling of gravity-driven fingers in unsaturated porous media: The inadequacy of the Richards Equation with standard monotonic constitutive relations and hysteretic equations of state, *Water Resources Research*, 37(8), 2019–2035, doi:10.1029/2000WR900403.

Eliassi, M., and Glass, R.J. (2002), On the porous-continuum modeling of gravity-driven fingers in unsaturated materials: Extension of standard theory with a hold-back-pile-up effect, *Water Resources Research*, 38(11), 1234, doi:10.1029/2001WR001131.

Eliassi, M., and Glass, R.J. (2003), On the porous continuum-scale modeling of gravity-driven fingers in unsaturated materials: Numerical solution of a hypodiffusive governing equation that incorporates a hold-back-pile-up effect, *Water Resources Research*, 39, 1167, doi:10.1029/2002WR001535, 6.

Glass, R.J., and Nicholl, M.J. (1996), Physics of gravity fingering of immiscible fluids within porous media: An overview of current understanding and selected complicating factors, *Geoderma*, 70, 133–163.

Hassanizadeh, S.M., and Gray, W.G. (1993), Thermodynamic basis of capillary pressure in porous media, *Water Resources Research*, 29(10), 3389–3405, doi:10.1029/93WR01495.

Hirashima, H., Avanzi, F., and Yamaguchi, S. (2017), Liquid water infiltration into a layered snowpack: evaluation of a 3-D water transport model with laboratory experiments, *Hydrology and Earth System Sciences,* 21, 5503-5515, https://doi.org/10.5194/hess-21-5503-2017.

Hirashima, H., Yamaguchi, S., and Katsushima, T. (2014), A multi-dimensional water transport model to reproduce preferential flow in the snowpack, *Cold Regions Science and Technology*, 108, 80-90, doi:10.1016/j.coldregions.2014.09.004.

Horton, R.E. (1915), The melting of snow, *Monthly Weather Review*, 43, 599–605.

Huang, H.C., Tan, Y.C. Liu, C.W., and Chen, C.H. (2005), A novel hysteresis model in unsaturated soil, *Hydrological Processes*, 19, 1653-1665, doi: 10.1002/hyp.5594.

Humphrey, N.F., Harper, J.T., and Pfeffer, W.T. (2012), Thermal tracking of meltwater retention in Greenland's accumulation area, *Journal of Geophysical Research*, 117, F01010, doi:10.1029/2011JF002083.

Illangasekare, T.H., Walter, R.J., Meier, M.F., and Pfeffer, W.T. (1990), Modeling of meltwater infiltration in subfreezing snow, *Water Resources Research*, 26(5), 1001–1012, doi:10.1029/WR026i005p01001.

Joekar-Niasar, V., Doster, F., Armstrong, W.T., Wildenschild, D., and Celia, M.A. (2013), Trapping and hysteresis in two-phase flow in porous media: A pore-network study, *Water Resources Research*, 49, 4244–4256, doi:10.1002/wrcr.20313.

Jordan, P. (1983), Meltwater movement in a deep snowpack: 2. Simulation model, *Water Resources Research*, 19(4), 979–985, doi:10.1029/WR019i004p00979.

Katsushima, T., Yamaguchi, S., Kumakura, T., and Sato, A. (2013), Experimental analysis of preferential flow in dry snowpack, *Cold Regions Science and Technology*, 85, 206-216, doi:10.1016/j.coldregions.2012.09.012.

Kattelmann, R. (1984), Wet slab instability, *Proceedings of the 1984 International Snow Science Workshop*, 102-108.

Knight, C.A. (1967), The contact angle of water on ice, *Journal of Colloid and Interface Sciences*, 25(2), 280-284, doi:10.1016/0021-9797(67)90031-8.

Kool, J. B., and Parker, J. C. (1987), Development and evaluation of closed-form expressions for hysteretic soil hydraulic properties, *Water Resources Research*, 23(1), 105-114, doi:10.1029/WR023i001p0010.

Land, C.S. (1968), Calculation of imbibition relative permeability for two- and three-phase flow from rock properties, *Society of Petroleum Engineers Journal*, 8(2), 149–156.

Lenhard, R.J., and Parker, J.C. (1987), A model for hysteretic constitutive relations governing multiphase flow: 2. Permeability-saturation relations, *Water Resources Research*, 23(12), 2197–2206, doi:10.1029/WR023i012p02197.

Leroux, N.R., and Pomeroy, J.W. (2017), Modelling capillary hysteresis effects on preferential flow through melting and cold layered snowpacks, *Advances in Water Resources*, 107, 250-264, doi:10.1016/j.advwatres.2017.06.024.

Likos, W., Lu, N., and Godt, J. (2013), Hysteresis and uncertainty in soil-water retention curve parameters, *Journal of Geotechnical and Geoenvironmental Engineering*, 140(4), doi:10.1061/(ASCE)GT.1943-5606.0001071.

Lopez-Moreno, J.I., Gascoin S., Herrero J. Sproles E.A., Pons M., Alonso-González, E. Hanich L., Boudhar A., Musselman K.N., Molotch N.P., Sickman J. and J.W. Pomeroy (2017), Different sensitivities of snowpacks to warming in Mediterranean climate mountain areas, *Environmental Research Letters*, 12, 1-10, doi:10.1088/1748-9326/aa70cb

Marsh, P. (1991), Water flux in melting snow covers, Chapter 2 in: M.Y. Corapcioglu (Editor), *Advances in Porous Media*, Vol. 1, Elsevier, Amsterdam, 61–124.

Marsh, P., and Woo, M. (1984), Wetting front advance and freezing of meltwater within a snow cover: 1. Observations in the Canadian Arctic, *Water Resources Research*, 20(12), 1853–1864, doi:10.1029/WR020i012p01853.

Mualem, Y. (1974), A conceptual model of hysteresis, *Water Resources Research*, 10(3), 514-520, doi:10.1029/WR010i003p00514.

Musselman, K., Clark, M.P., Liu, C., Ikeda, K., and Rasmussen, R. (2017), Slower snowmelt in a warmer world, *Nature Climate Change*, 7, 214-219, doi:10.1038/NCLIMATE3225.

Nieber, J.L., Dautov, R.Z., Egorov, A.G., and Sheshukov, A.Y. (2005), Dynamic capillary pressure mechanism for instability in gravity-driven flows; review and extension to very dry conditions, *Transport in Porous Media*, 58(1-2), 147-172. doi:10.1007/s11242-004-5473-5

Nieber, J.L., Sheshukov, A., Egorov, A., and Dautov, R. (2003), Non-equilibrium model for gravity-driven fingering in water repellent soils: formulation and 2D simulations, *Soil Water Repellency: Occurrence*, Consequences and Amelioration, edited by C. J. Ritsema and L. W. Dekker, 245–257, Elsevier Sci., New York.

Pomeroy, J.W., Fang, X., and Marks, D. (2016), The cold rain-on-snow event of June 2013 in the Canadian Rockies - characteristics and diagnosis, *Hydrological Processes*, doi: 10.1002/hyp.10905.

Pomeroy J.W., Fang X., and K. Rasouli (2015), Sensitivity of snow processes to warming in the Canadian Rockies, *Proceedings, 72nd Eastern Snow Conference*, 22-33.

Rauscher, S. A., J. S. Pal, N. S. Diffenbaugh, and M. M. Benedetti (2008), Future changes in snowmelt-driven runoff timing over the western US, *Geophysical Research Letters*, 35, L16703, doi:10.1029/2008GL034424.

Razavi, S., and Gupta, H.V. (2016a), A new framework for comprehensive, robust, and efficient global sensitivity analysis: I. Theory, *Water Resources Research*, 51, doi:10.1002/2015WR017558.

Razavi, S., and Gupta, H.V. (2016b), A new framework for comprehensive, robust, and efficient global sensitivity analysis: II. Application, *Water Resources Research*, 51, doi:10.1002/2015WR017559.

Sander, G.C., Glidewell, O.J., and Norbury, J. (2008), Dynamic capillary pressure, hysteresis and gravity-driven fingering in porous media, *Journal of Physics: Conference Series*, 138, 12023, doi:10.1088/1742-6596/138/1/012023.

Schneebeli, M. (1995), Development and stability of preferential flow paths in a layered snowpack, *Biogeochemistry of Seasonally Snow-Covered Catchments* (Proceedings of a Boulder Symposium July 1995). IAHS Publ. no. 228.

Spiteri, E.J., Juanes, R., Blunt, M.J., and Orr, M.J. (2005), Relative-permeability hysteresis: trapping models and application to geological CO2 sequestration, paper presented at *Society of Petroleum Engineering Annual Technical Conference and Exhibition*, Dallas, Tex., doi:10.2118/96448-MS.

van Genuchten, M.T. (1980), A closed-form equation for prediction the hydraulic conductivity of unsaturated soils, *Soil Science Society of America Journal*, 44, 892-898.

Waldner, P., Schneebeli, M., Schultze-Zimmermann, U., and Flühler, H. (2004), Effect of snow structure on water flow and solute transport, *Hydrological Processes*, 18 (7), 1271–1290.

Wankiewicz, A. (1979), A review of water movement in snow*, Proceeding Modelling Snowcover Runoff*, Cold Regions Research and Engineering Laboratory, Hanover, New Hampshire, 222-252, 1979.

Werner, A.D., and Lockington, D.A. (2006), Artificial pumping errors in the Kool-Parker scaling model of soil moisture hysteresis, *Journal of Hydrology*, 325, 118-133, doi: 10.1016/j.jhydrol.2005.10.012.

Wever, N., Fierz, C., Mitterer, C., Hirashima, H., and Lehning, M. (2014), Solving Richards Equation for snow improves snowpack meltwater runoff estimations in detailed multi-layer snowpack model, *The Cryosphere*, 8, 257-274, doi: 10.5194/tc-8-257-2014.

Wever, N., Vera Valero, C., and Fierz, C. (2016), Assessing wet snow avalanche activity using detailed physics based snowpack simulations, *Geophysical Research Letters*, doi:10.1002/2016GL068428.

Würzer, S., Wever, N., Juras, R., Lehning, M., and Jonas, T. (2017), Modelling liquid water transport in snow under rain-on-snow conditions – considering preferential flow, *Hydrology and Earth System Sciences*, 21, 1741-1756, doi:10.5194/hess-21-1741-2014

Yamaguchi, S., Katsushima, T., Sato, A., and Kumakura, T. (2010), Water retention curve of sow with different grain sizes, *Cold Regions Science and Technology*, 64(2), 87-93, doi:10.1016/j.coldregions.2010.05.008.

Zhang, H., and Zegeling, P.A. (2017), A numerical study of two-phase flow models with dynamic capillary pressure and hysteresis, *Transport in Porous Media*, 116, 825-846, doi:10.1007/s11242-016-0802-z.

CHAPTER 6

IMPACT OF HEAT CONVECTION INDUCED BY TOPOGRAPHY-DRIVEN AIR VENTILATION ON SNOW SURFACE TEMPERATURE

Abstract

In snowpack models, thermal conduction is the only heat mechanism accounted for to simulate the energy exchange between the upper and lower boundaries of a snowpack, changes of snow internal energy, and kinetic metamorphism. Snow surface temperature is used not only as the upper boundary for the heat flow equation but is critical in estimating the energy balance over snow in a manner that fully couples the lower atmosphere to snow on the ground. This research investigates the impact of heat convection within snow on the simulation of snow surface temperature. A 2D model was created to simulate the heat conduction-convection equation in a homogeneous snowpack. In this model, thermal convection is induced by topography-driven airflow within the snowpack, and the upper boundary for the snow internal energy equation is determined by solving for the energy balance at the snow surface using meteorological data. This study suggests that heat convection through snow can produce a non-uniform spatial distribution of snow surface temperature, which follows the shape of the pressure distribution at the surface. Taller dunes and snow dunes with short wavelengths increased thermal convection through snow. A sensitivity analysis on snow properties (density, grain size, and depth) demonstrated that air convection was reduced in denser and finer snowpacks and that the layering system of a snowpack greatly impacted the estimated snow surface temperature. This study is a step toward better predicting energy flows through snow and the energy transfer between the atmosphere and snow.

6.1 Introduction

Exchange of energy between the atmosphere and the snow surface drives snowmelt at the surface of a snowpack (*Male and Granger*, 1981; *Gray and Landine*, 1988). In numerical models, assumptions are made to simplify the energy balance; for instance, turbulent fluxes are simplified by 1st order theories and the snow surface is considered an impermeable and flat boundary. In real conditions, the snow-atmosphere boundary is a permeable wall that permits penetration of wind flow. Air ventilation in snow and firn has been observed in both natural and artificial snowpacks (*Albert and Hardy*, 1995; *Clifton et al.,* 2008; *Drake et al.*, 2017) and modeled (*Colbeck*, 1989, 1997; *Clarke and Waddington,* 1991, *Albert*, 1993). Airflow through pore spaces impacts the thermal regime of ice sheets and snowpacks by transporting heat and water vapor (*Clarke et al.*, 1987; *Powers et al.,* 1985), as well as the transport of chemical species (*Waddington and Cunningham,* 1996).

Several processes can be responsible for the ventilation of air within snow, such as turbulence in the lower layer of the atmosphere (*Clifton et al*., 2008), topographic-driven pressure gradients at the snow surface (*Waddington and Cunningham,* 1996), or internal temperature gradients (*Sturm,* 1991). In wind tunnel experiments with restricted turbulence compared to outdoor conditions (*Aksamit and Pomeroy*, 2018), *Clifton et al.* (2008) observed that shear-driven ventilation occurred only at the surface of a snowpack in a wind tunnel and had, therefore, a negligible effect on heat transfer within snow. *Colbeck* (1989) demonstrated through numerical experiments that the topography of the snow surface creates a pressure distribution that is the main process responsible for airflow through snow. This was later confirmed by *Bartlett and Lehning* (2011).

Albert and Hardy (1995) conducted a field experiment to induce wind flow at the surface of a snowpack while measuring temperature distributions within the snowpack. They observed highly non-uniform internal snow temperature distributions which were represented by a 2D advection-conduction heat transfer model.

The radiative snow surface temperature is the temperature at the upper skin of the snow surface that is exposed for thermal and near infrared radiative transfer (*Pomeroy et al.,* 2016). It controls the boundary condition for longwave radiation emission and near-infrared reflectance from the snowpack. It is possible to model the snow surface temperature, the temperature of the upper

molecular layer of snow crystals that are most exposed to the atmosphere, as a function of radiative or convective exchange without reference to internal snowpack energetics because of the poor thermal conductivity between snow surface and underlying snowpack (*Pomeroy et al*., 2016; *Harder et al.*, 2018). However, as not all turbulent exchange occurs at the snow surface when there is wind flow under this surface, the upper snowpack layer is the upper boundary driving the internal heat transfer, and thermal convection within snow may sometimes impact the snow surface temperature. This was evident in the scatter measured by *Pomeroy et al.* (2016) compared to an energy balance relationship that did not include conduction between the snow surface and the snowpack. The spatial variability of snow surface temperature is unknown.

Some studies have used the radiative snow surface temperature as an index to assess snow model performance (*Lapo et al.,* 2015; *Conway et al.*, 2018). This index has exposed the under-estimation of turbulent fluxes by the current theories under stable atmospheric conditions that are often encountered above snow (*Cullen et al.*, 2007). In particular, *Helgason and Pomeroy* (2012) observed that the measured sensible flux could not offset heat loss through longwave radiation during clear sky conditions, which resulted in unrealistic drops in simulated snow surface temperature using the SNTHERM model. *Helgason and Pomeroy* (2012) suspected that forced convection under the presence of sastrugi might have influenced measured snow surface temperature. To resolve this issue, a numerical strategy consists in adding a 'windless coefficient' to increase estimated sensible heat flux under stable conditions (*Brun et al.*, 1989; *Jordan et al.*, 1999; *Brown et al*., 2006). This method, however, lacks physical realism.

This study investigates the impact of thermal convection induced by topography-driven pressure fluctuations at the snow surface coupled with surface energy balance on simulated near snow surface temperature. The effects of meteorological input data, snow properties (density, grain size, and depth), and snow layering system on heat convection are also examined.

6.2 Snow Energy Balance

Energy fluxes applied at both the upper and lower boundaries of a snowpack (surface energy balance and ground heat flux, respectively) contribute to the change of snow internal energy ($\frac{dU}{dt}$ in [W m^{-2}]) (e.g. *Male and Gray,* 1975):

$$\frac{dU}{dt} = Q_{\mathrm{H}}(T_{\mathrm{s}}) + Q_{\mathrm{E}}(T_{\mathrm{s}}) + Q_{\mathrm{G}} + Q_{\mathrm{net}}(T_{\mathrm{s}}) + Q_{\mathrm{p}} - Q_{\mathrm{m}}, \tag{6.1}$$

where Q_{H} is the sensible heat flux [W m^{-2}], Q_{E} is the latent heat flux [W m^{-2}], Q_{G} is the ground heat flux [W m^{-2}], Q_{net} is the net radiation flux at the surface [W m^{-2}], Q_p is the energy advected by from rain [W m^{-2}] and Q_{m} is the energy available for melt [W m^{-2}] and T_{s} is the temperature of the surface exchange layer between the atmosphere and the snowpack [K]. Q_{p} and Q_{m} are neglected in this study.

Pomeroy et al. (2016) developed an energy balance model to solve for the radiative snow surface temperature, assuming that the snow surface is thermally disconnected from the underlying snow (i.e. there is no heat conduction between the snow surface and the underlying layer). Their model considers a no-mass "skin snow surface" of zero energy. In this study, the energy balance at the snow surface is applied to an exchange layer of a few centimeter. This exchange layer is assumed to have no mass and is linked to the snowpack via a heat conduction term (Q_{cond} in [W m^{-2}], positive towards the snow surface) is considered. The surface energy balance applied to the snow surface exchange layer is therefore:

$$Q_{\mathrm{H}} + Q_{\mathrm{E}} + Q_{\mathrm{L}} + Q_{\mathrm{K,3}} + Q_{\mathrm{cond}} = 0\ . \tag{6.2}$$

where $Q_{\mathrm{K,3}}$ is the net near-infrared shortwave radiation [W m^{-2}] (Eq. 6.4) and Q_{L} is the net longwave radiation [W m^{-2}] (Eq. 6.3). From this point, the surface exchange layer is simply called the "snow surface" and its temperature is denoted T_{s}. The no-mass assumption will be discussed in Section 6.6.

6.2.1 Radiative Fluxes

The net radiation flux is the sum of the net longwave radiation and the net shortwave radiation (Q_{K} in [W m^{-2}]). The net longwave radiation, which is assumed to occur at the snow surface (Dozier and Warren, 1982) is the difference between incoming and outgoing longwave radiation (Eq. 6.3). In this study, snow emissivity (ϵ) was assumed constant equal to 1, as in *Vionnet et al.* (2012) and *Essery* (2015).

$$Q_{\mathrm{L}} = L_{\mathrm{in}} - L_{\mathrm{out}}, \tag{6.3a}$$

$$L_{\text{out}} = (1 - \epsilon) L_{\text{in}} + \epsilon \, \sigma \, T_{\text{s}}^4 \,, \tag{6.3b}$$

where L_{in} and L_{out} are the incoming and outgoing longwave radiation [W m^{-2}], respectively, σ is the Stefan-Boltzmann constant (σ=5.67x10^{-8} W m^{-2} K^{-4}).

Shortwave radiation penetrates the snowpack following an exponential decay (*Male and Granger*, 1981; *Lehning et al.*, 2002). Incoming shortwave radiation can be separated into three different spectral bands (Eq. 6.4), for which the snow albedo depends on snow optical grain size and snow age (*Vionnet et al.*, 2012). Shortwave radiation in spectral bands 1 and 2 penetrates the snow surface, while that in spectral band 3 is absorbed or reflected at the surface.

$$Q_{\text{K}}(z) = \Sigma_{i=1}^{3} \, (1 - A_i) K_{\text{in}} \, e^{-\beta_i \, z} \tag{6.4}$$

where A_i is the snow surface albedo for spectral band i (c.f. *Vionnet et al*. (2012) for the equations relating A_i to snow optical grain size and snow age), K_{in} is the incoming shortwave radiation [W m^{-2}], and β_i is the extinction coefficient for spectral band i [m^{-1}] (c.f. *Vionnet et al*., 2012).

6.2.2 Turbulent Fluxes

A first-order closure is applied to estimate the vertical fluxes of momentum, sensible heat, and latent heat, i.e. these fluxes are proportional to the vertical gradients of wind speed, temperature, and specific humidity, respectively. To account for atmospheric stability, the Monin-Obukohv similarity theory is used (*Monin and Obukhov,* 1954). Friction velocity (u_* in [m s^{-1}]), sensible heat flux, and latent heat flux are expressed as

$$u_* \; = \; k \, u(z) \left[\ln\left(\frac{z - d_0}{z_{0\text{m}}}\right) - \Psi_{\text{m}}\left(\frac{z - d_0}{L}\right) \right]^{-1} \,, \tag{6.5a}$$

$$Q_{\text{H}} \; = \; u_* \, k \, C_{\text{p,a}} \, \rho_a \; (T_{\text{a}} \; - \; T_{\text{s}}) \left[\ln\left(\frac{z - d_0}{z_{0\text{h}}}\right) - \Psi_{\text{h}}\left(\frac{z - d_0}{L}\right) \right]^{-1}, \tag{6.5b}$$

$$Q_{\text{E}} \; = \; u_* \, k \, L_{\text{v}} \, \rho_a \, (q \; - \; q_{\text{s}}) \left[ln\left(\frac{z - d_0}{z_{0\text{q}}}\right) - \Psi_{\text{q}}\left(\frac{z - d_0}{L}\right) \right]^{-1}, \tag{6.5c}$$

where k is the von Karman constant (= 0.4), u is wind speed at the reference height z. $z_{0\text{m}}$, $z_{0\text{h}}$ and $z_{0\text{q}}$ are roughness lengths for momentum, heat and vapor transfers, respectively, d_0 is displacement height (equal to snow depth), ρ_a is air density, T_{a} is air temperature at the reference height, q and q_{s} are specific humidities at the reference height and at the surface, respectively, $C_{\text{p,a}}$

is heat capacity of the air, L_v is latent heat of sublimation. Ψ_m, Ψ_h and Ψ_q are stability correction functions for momentum, heat transfer, and vapour transfer, respectively and L is the Monin-Obukhov length [m] (Eq. 6.6). Roughness length for momentum was assumed constant at 1 mm (*Andreas et al.*, 2005), and z_{0h} and z_{0q} are scaled from z_{0m} by a factor 0.1 (*Essery*, 2015).

An indicator of stability was suggested by *Monin and Obukhov* (1954):

$$\zeta = \frac{z-d_0}{L}, \tag{6.6a}$$

$$L = \left(\frac{u_*^3}{\rho_a}\right)/\left(k\, g\, \frac{Q_H}{T_a C_p}\right), \tag{6.6b}$$

where L is the Monin-Obukhov length [m] that accounts for buoyancy effects and g is acceleration by gravity (g=9.81 m s^{-2}).

In a stable atmosphere (ζ>0), turbulent motions are reduced and stability functions defined by *Holtslag and De Bruin* (1988) are used:

$$\Psi_m = \Psi_h = \Psi_q = -\left(a\zeta + b\left(\zeta - \frac{c}{d}\right)e^{-d\zeta} + \frac{bc}{d}\right), \tag{6.7}$$

with a = 0.7, b = 0.75, c = 5, and d = 0.35.

Under unstable atmospheric conditions (ζ<0), turbulent motions are enhanced and correction functions are estimated from *Paulson* (1970):

$$\Psi_m = 2\ln\left(\frac{1+x}{2}\right) + \ln\left(\frac{1+x^2}{2}\right) - 2\arctan(x) + \frac{\pi}{2}, \tag{6.8a}$$

$$\Psi_h = \Psi_q = 2\ln\left(\frac{1+x^2}{2}\right), \tag{6.8b}$$

where $x = (1-\gamma\,\zeta)^{0.25}$ and γ is an empirical coefficient commonly taken equal to 16.

6.3 Thermal Convection in Porous Media

Heat convection is driven by velocity of the air phase, which should be estimated first.

6.3.1 Airflow calculation

The topography-driven airflow theory is taken from previous studies of airflow through snow (e.g. *Bartlett and Lehning*, 2011). It is assumed that the air phase saturates the pore space. The velocity vector of the air phase ($\boldsymbol{q}$) is estimated using Darcy's law:

$$\boldsymbol{q} = -\frac{k_s}{\mu} \nabla P \tag{6.9}$$

where k_s is snow intrinsic permeability [m^2] estimated from *Calonne et al.* (2012), μ is dynamic viscosity of air [Pa s] and P is pressure within the snowpack driving the airflow [Pa].

P is divided into a stationary, homogeneous ambient pressure (P_0 in [Pa]) and a time-varying, inhomogeneous pressure fluctuation of smaller magnitude ($p'(\boldsymbol{x}, t)$ in [Pa] with $\boldsymbol{x}$ the position vector and t the time variable):

$$P = P_0 + p'(\boldsymbol{x}, t), \tag{6.10}$$

Assuming the flow is incompressible, $\boldsymbol{q}$ followed:

$$\nabla . \boldsymbol{q} = 0 , \tag{6.11}$$

thus, if k_s is isotropic and homogeneous, p' is the solution of the Laplace equation:

$$\Delta p' = 0 . \tag{6.12}$$

Surface pressure distribution along the snow surface was described as in *Colbeck* (1989), *Cunningham and Waddington* (1993), and *Bartlett and Lehning* (2011):

$$p'(z = h, t) = P_\mathrm{d} \sin(\frac{2\pi}{\Lambda} x), \tag{6.13}$$

where Λ is the wavelength of the dunes [m], h is the height of the snow surface [m], and P_d is the amplitude of pressure distribution at the snow surface [Pa] caused by the snow dune and the wind speed at the surface. Following *Bartlett and Lehning* (2011), P_d is estimated by:

$$P_\mathrm{d} = M \rho \frac{H}{\Lambda} u^2 , \tag{6.14}$$

where M is an empirical coefficient (chosen equal to 4 as in *Bartlett and Lehning*, 2011), H is half the height of the dune [m].

For simplicity, a flat surface is approximated under the condition that (*Bartlett and Lehning,* 2011):

$$\frac{H}{\Lambda} << 0.35 \tag{6.15}$$

Figure 6.1 shows an example of simulated pressure distribution (colors) above a snow surface for a wind speed of 5 m s^{-1}, a 5-cm high snow dune and 2-m snow dune wavelength. The airflow direction and intensity resulting from the pressure distribution (direction and magnitude of the arrows, respectively) are also presented.

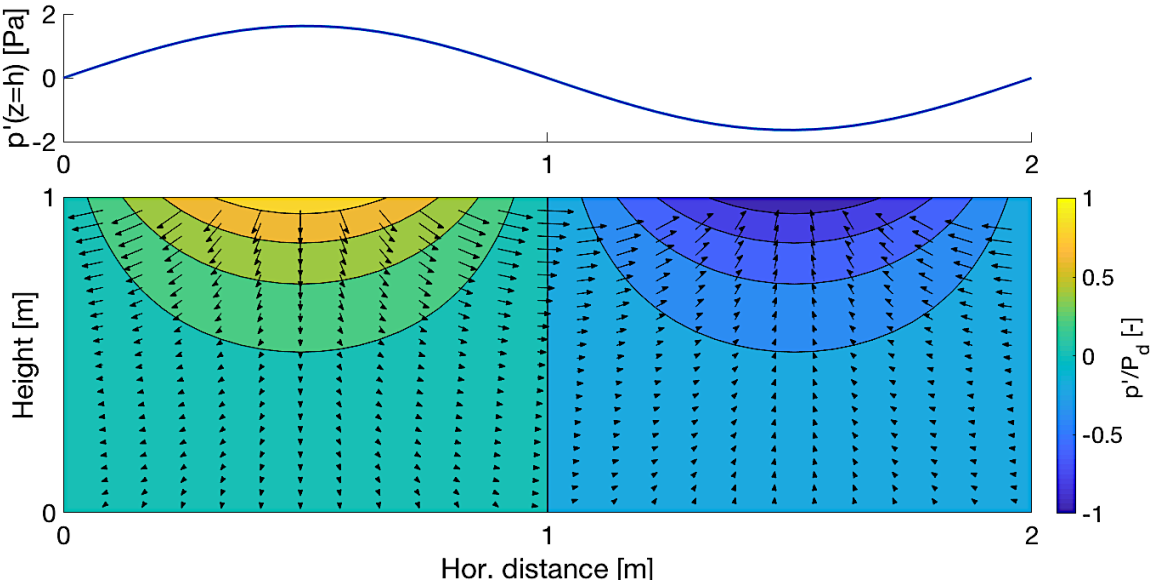

Figure 6.1 a) Pressure distribution at the snow surface for a 5-cm high and 2-m long dune and a wind speed of 5 m s^{-1}. **b)** The colormap presents the 2D pressure distribution within the snowpack resulting from the pressure at the surface (**a**) and the arrows show the direction and magnitude of the airflow within the snowpack as a result of the 2D pressure distribution.

6.3.2 Heat Transfer

In this study, liquid water within the pore space is neglected. Thus, the snowpack is only composed of the ice and air phases. Assuming incompressible airflow and thermal equilibrium between the gas and solid phases, the convection-conduction heat equation within the snowpack is:

$$\left(\rho\, C_{\mathrm{p}}\right)_s \frac{\partial T}{\partial t} + \phi\, \left(\rho\, C_{\mathrm{p}}\right)_a \boldsymbol{u}\,.\nabla T = \nabla.\left(\kappa_s\, \nabla T\right) \tag{6.16}$$

where T is snow temperature [K], ϕ is snow porosity, and κ_s is snow thermal conductivity [W K^{-1} m^{-1}] estimated from *Calonne et al*. (2011).

6.4 Model Design

A 2D model was developed to simulate the energy balance near the snow surface and heat transfer through advection and conduction within the snowpack. Vapour transport was not considered in this research as it has a small effect on heat transfer (*Albert and McGilvary*, 1992). An explicit upwind finite volume method was applied to solve for the 2D heat convection-conduction equation (Eq. 6.16). The snowpack temperature profile was initially assumed to be linear, ranging from -10ºC at the surface to 0ºC at the bottom. A constant temperature was assumed at the bottom of the snowpack (=0ºC) and periodic boundary conditions were specified at the lateral boundaries. The time step was calculated to meet the CFL condition for the 2D heat conduction-convection equation with a default value of 1 s.

The model was first run simulating heat conduction only and was compared to the analytical solution of the heat conduction equation. A 1-m high and 2-m wide homogeneous snowpack was considered, with a density of 300 kg m^{-3} and a grain size of 1 mm. The meteorological inputs are summarized in Table 6.1. The snowpack was discretized into 50 x 50 cells. Figure 6.2 presents the simulated snow internal temperature at steady state (Fig. 6.2a) and the comparison between the model results and the analytical solutions (Fig. 6.2b). The model reproduced the results from the analytical solution. This discretization will thus be used in the following sections.

Table 6.1 Snow properties, model boundaries, and atmospheric inputs for the reference case.

Density	300 kg m^{-3}
Grain size	1 mm
Temperature at snow-soil interface	0°C
Initial snow surface temperature	-10°C
Dune height	5 cm
Dune wavelength	2 m
Roughness length	1 mm
Height of measurement	2 m
Air temperature	-20°C
Wind speed	5 m s^{-1}
Relative humidity	80 %
Incoming shortwave radiation	100 W m^{-2}
Incoming longwave radiation	200 W m^{-2}

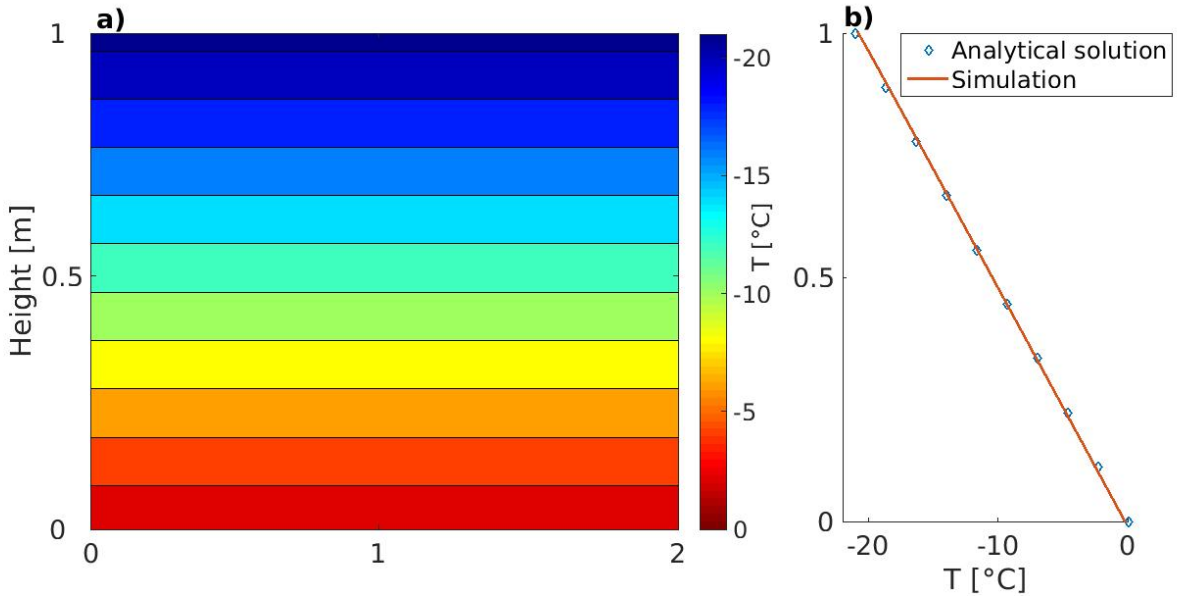

Figure 6.2 a) Simulated internal snow temperature at steady assuming heat conduction only **b**) Comparison of simulated vertical temperature distribution against the analytical solution of the steady state heat conduction equation.

6.5 Results

6.5.1 Impact of Dune Height

To investigate the impact of the height of snow dunes on simulated snow surface and internal temperature, the wavelength of the snow dune was kept constant at 2 m. Snow properties, domain boundaries, and atmospheric inputs for the reference case are summarized in Table 6.1. The height of the snow dune was increased from 5 cm to 15 cm with a constant step of 5 cm for two different air temperatures (-20°C and -10°C). All other variables were kept constant and the simulations were run until steady state. Figure 6.3a presents the lateral (horizontal) distribution of the simulated snow surface temperature for three different dune heights, at an air temperature of -20°C. The snow surface temperature was not homogeneous. At each dune height, the location of maximal snow surface temperature corresponded to the location of minimum pressure at the snow surface (Fig. 6.1). Inversely, the lowest snow surface temperature was estimated where the pressure at the surface was maximal (i.e. where the air moved downward within the snow, Fig. 6.1). For increasing dune height, the maximum value of the snow surface temperature increased, while the minimum value remained similar at all dune heights. The difference between the maximum and minimum values of the estimated snow surface temperatures over the snow surface (ΔT_s), which

symbolizes the heterogeneity in the lateral distribution of snow surface temperature, for all three dune heights and at the two different air temperatures, are shown in Fig. 6.3b. At all dune heights, ΔT_s decreased with increasing air temperature. For the dune height increasing from 5 cm to 15 cm, the maximum value of snow surface temperature increased by 1.1°C for T_a = -20°C and by 0.7°C for T_a = -10°C.

Heterogeneity in snow surface temperature can be explained by looking at the difference between the 2D distribution of the simulated snow internal temperature for all three different dune heights and the internal temperature of flat snow (without thermal convection, Fig. 6.2a) (Fig. 6.4). For taller dunes (from top to bottom in Fig. 6.4), airflow within the snow was faster, resulting in greater thermal convection flux. This caused the cold front on the left-hand side of the snowpack (where the air flowed downward from the surface, Fig. 6.1) to be colder and reach deeper snowpack layers. Conversely, the velocity of the upward airflow (on the right-hand side of the snowpack) increased with dune height and more thermal energy was transported from the warm ground-snow interface to the snow surface, resulting in a warmer internal snow temperature just below the surface on the right-hand side of the snowpack. This corresponded with higher snow surface temperatures simulated on the right-hand side of the snowpack for increasing dune height.

A similar analysis was conducted for two different wind speeds (5 m s^{-1} and 10 m s^{-1}) while the other variables were kept constant (c.f. Table 6.1). The new results were similar to the previous observations. The minimum value of snow surface temperature varied very little with wind speed and dune height, and the highest value of snow surface temperature increased with dune height and agreed with the location of the smallest pressure at the snow surface. ΔT_s increased with wind speed and dune height (Fig. 6.3.b).

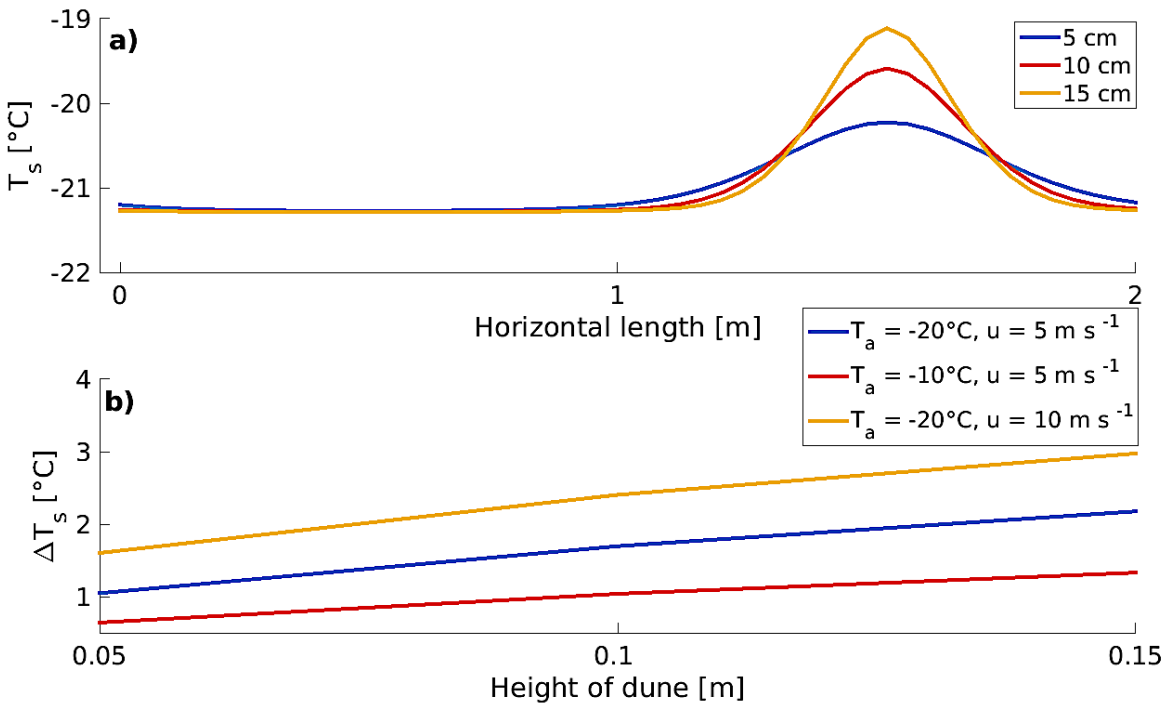

Figure 6.3 a) Horizontal distribution of simulated snow surface temperature for three dune heights (5 cm, 10 cm, and 15 cm) at an air temperature of -20°C and a dune length of 2 m. **b)** Difference between the maximum and the minimum values of the distributed snow surface temperatures (ΔT_s) for two different air temperatures (-20°C and -10°C) and increasing dune height (from 5 cm to 15 cm) with a constant dune length of 2 m.

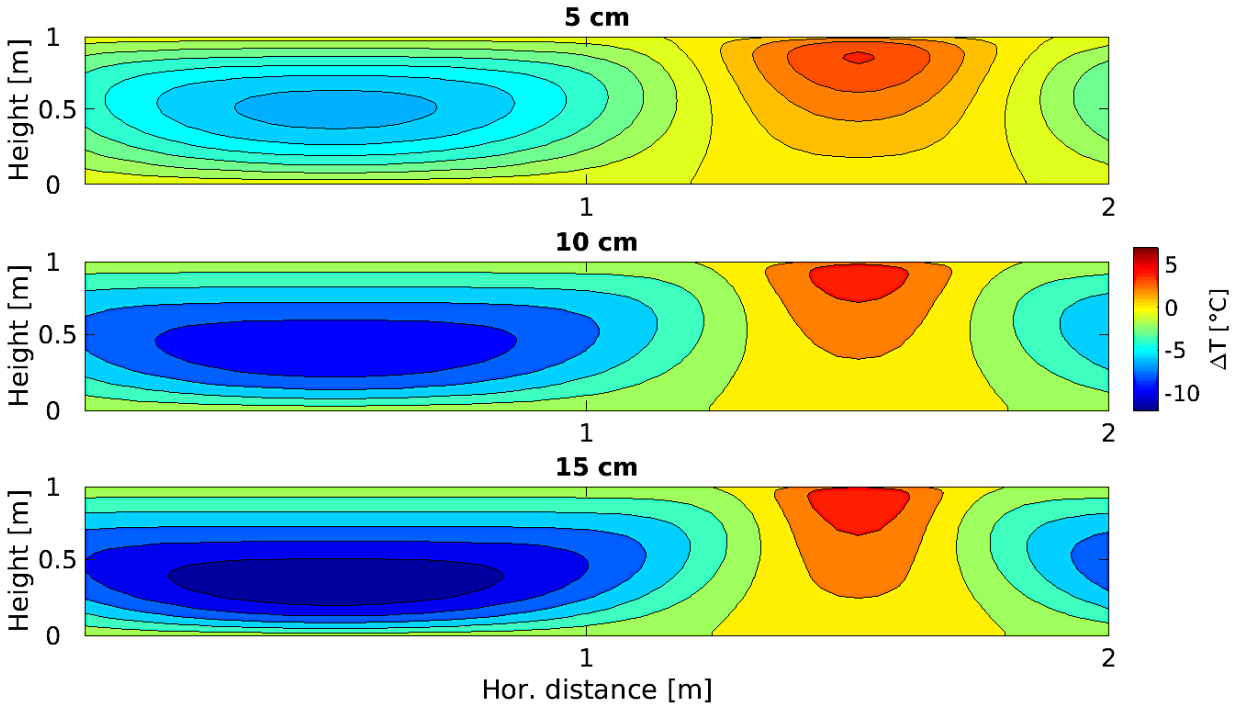

Figure 6.4 Simulated snow internal temperature with the values from the reference case (Table 6.1) for three different dune heights (5 cm, 10 cm, and 15 cm from top to bottom) and a constant dune length of 2 m.

6.5.2 Impact of Dune Wavelength

In this section, the impact of dune length on simulated snow temperature is studied. Simulations were first run for two different air temperatures (-10°C and -20°C) at a fixed dune height of 5 cm. All the other model inputs and initial conditions were kept constant (Table 6.1). The results are presented after steady state was reached.

Figure 6.5a shows the simulated lateral distribution of snow surface temperature for three different dune lengths (1 m, 5 m, and 10 m) and an air temperature of -20°C. Snow surface temperature presented a similar distribution as in Section 6.5.1. For longer dunes, the minimum value of snow surface temperature increased, while the maximum value decreased: snow surface temperature became more homogeneous. Figure 6.5b presents the variation of ΔT_s with air temperature and dune length. ΔT_s was greater for a colder air temperature. The distributed surface temperature flattened with increasing dune length; this was caused by lower air convection from a more uniform pressure gradient at the snow surface (c.f. Eq. 6.13).

The wind speed was increased from 5 m s^{-1} to 10 m s^{-1} for a fixed air temperature of -20°C. The variations of ΔT_s for these two wind speeds and the three different dune lengths are presented in Fig. 6.5b. Unexpectedly, ΔT_s was non-monotonic with dune length: at the highest wind speed, the maximum value of snow surface temperature was higher for a 5-m wavelength than for a 1-m and 10-m wavelength (Fig. 6.5b). This was caused by higher heat convection in 5-m wavelength dune, resulting in more transport of energy from the bottom of the snowpack (warm) to the snow surface.

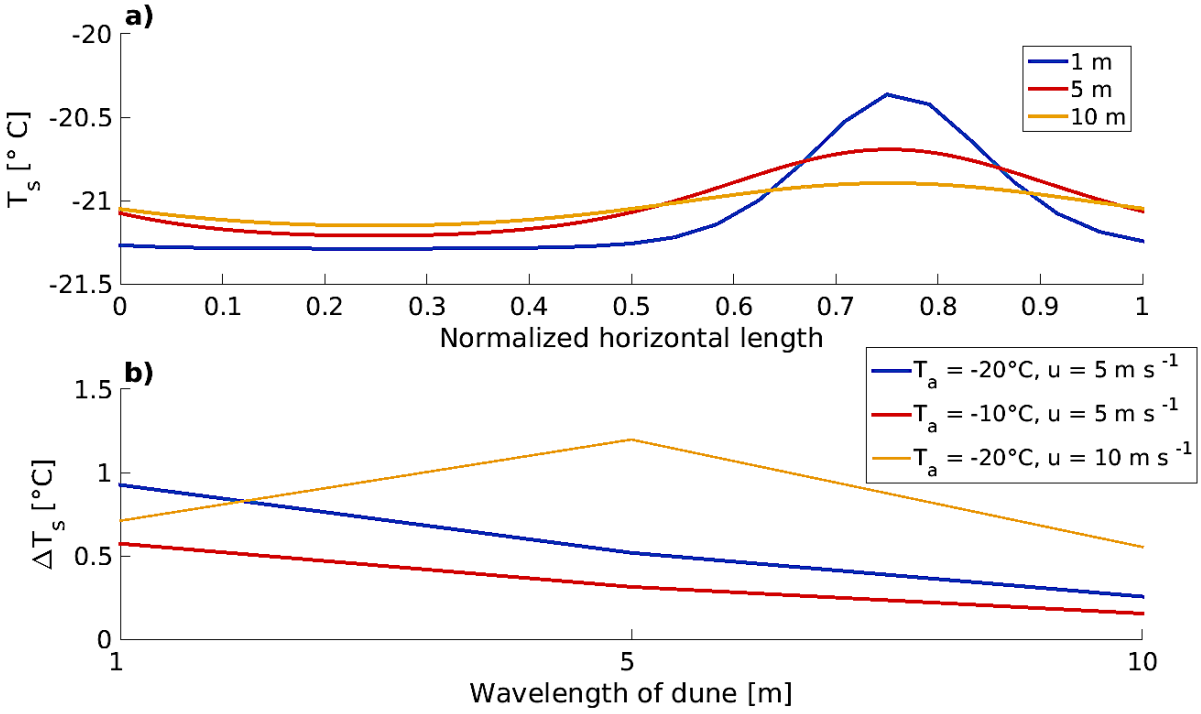

Figure 6.5 a) Horizontal distribution of snow surface temperature for three dune lengths (1 m, 5 m, and 10 m) and an air temperature of -20°C, a wind speed of 5 m s^{-1}, and a dune height of 5 cm. **b)** Difference between the maximum and minimum values of the distributed snow surface temperature (ΔT_s) for two different air temperatures (-10°C and -20°C), two different wind speeds (5 m s^{-1} and 10 m s^{-1}) and an increasing dune wavelength (from 1 m to 10 m), with a fix dune height of 5 cm.

6.5.3 Change of Snow Properties: Density, Grain Size and Depth

In this section, the impacts of snow properties (density, grain size, and depth) on thermal convection within snow and on simulated surface and internal temperatures are analyzed. The reference case for the sensitivity analysis is presented in Table 6.1. Each snow property is varied, while the others are kept constant.

Snow density of the homogeneous snowpack was varied from 150 kg m^{-3} to 450 kg m^{-3}, with a step of 150 kg m^{-3}. As snow density increased, the snow surface temperature distribution became more homogeneous due to a decreasing airflow velocity within the snowpack and. ΔT_s decreased from 2.9^{o}C to 0.13^{o}C (Fig. 6.6a). The average grain size of the snowpack was varied from 0.5 mm to 1.5 mm, with a step of 0.5 mm (Fig. 6.6b). ΔT_s increased with grain size due to higher air ventilation within the snowpack. Finally, snow depth was varied from 0.5 m to 1.5 m with a step of 0.5 m. Airflow velocity through the snow decreased in deeper snowpack, making the snow surface temperature more homogeneous and. ΔT_s decreased (Fig. 6.6c).

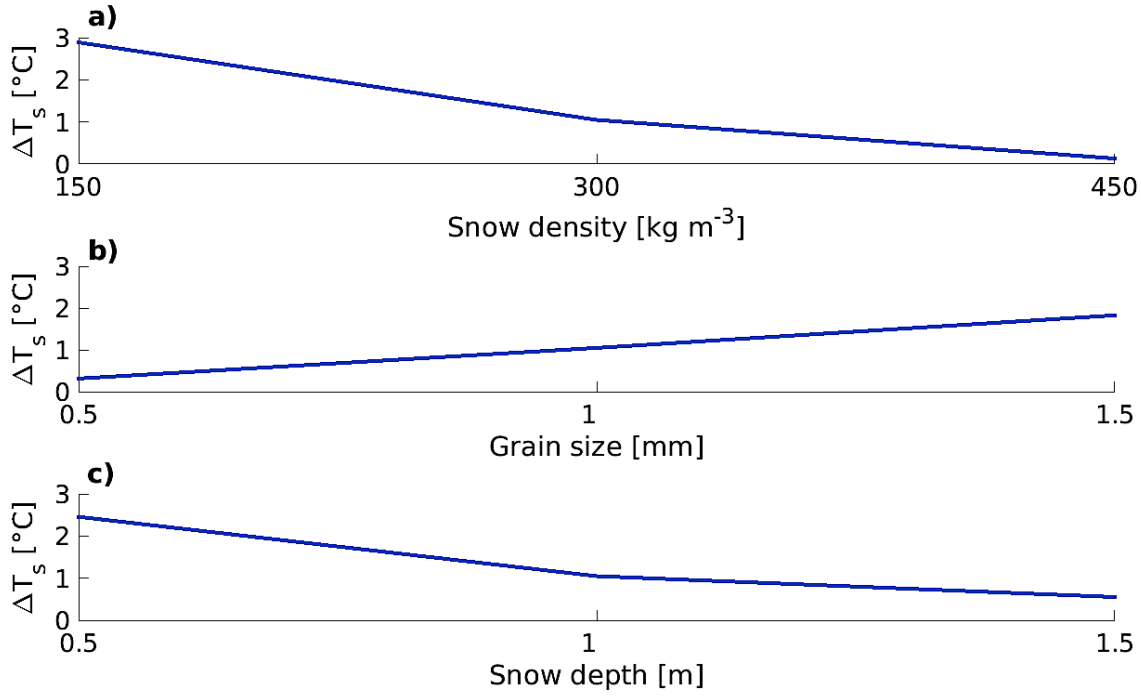

Figure 6.6 Difference between the maximum and minimum values of simulated snow surface temperature over the snow surface (ΔT_s) for **a)** increasing snow density (from 150 kg m^{-3} to 450 kg m^{-3}), **b)** increasing grain size (from 5 mm to 1.5 mm), and **c)** increasing snow depth (from 5 to 1.5 m).

6.5.4 Layered snowpack

The layered structure of a snowpack impacts air ventilation within snow (*Colbeck*, 1997). To solve for the airflow in a vertically layered snowpack, Eq. 6.12 becomes (*Colbeck*, 1997):

$$k_s \frac{\partial^2 p'}{\partial^2 x^2} + k_s \frac{\partial^2 p'}{\partial^2 z^2} + \frac{dk_s}{dz}\frac{\partial p'}{\partial z} = 0 \ . \quad (6.17)$$

Here, only two discontinued snow layers are considered in this section and the term $\frac{dk_s}{dz}\frac{\partial p'}{\partial z}$ in Eq. 6.17 would only impact airflow at the layer interface; hence, this term is neglected for simplicity.

The impact of snow layers on thermal convection is studied. Two 1-m snowpacks are considered: a fine over coarse layered snowpack (FC) and a coarse over fine layered snowpack (CF) (each layer was 0.5 m high). The density of each layer was the same (300 kg m^{-3}), the grain sizes of the fine and coarse layers were equal to 0.5 mm and 1.5 mm, respectively, and the other model inputs and parameters are summarized in Table 6.1. The estimated snow surface and internal temperatures are compared to those of a homogeneous snowpack of equivalent averaged snow properties (density of 300 kg m^{-3} and grain size of 1 mm, c.f. Table 6.1) and of similar dune height (5 cm) and dune wavelength (2 m).

The simulated snow surface temperature of the two layered snowpacks differed from the snow surface temperature of the homogeneous snowpack (Fig. 6.7a); the minimum snow surface temperature was not affected by the snow layers, but the maximum value was significantly higher for a CF snowpack because of greater airflow in the upper coarse layer (Fig. 6.7d). This increase in airflow (thermal convection) in the upper layer resulted in a warmer zone where the pressure is minimal (Fig. 6.7e), causing the increase of maximum snow surface temperature. The snow surface temperature of the FC snowpack was almost uniform due to the upper fine layer limiting the airflow (Fig. 6.7), resulting in a quasi-uniform temperature in the upper snowpack (not shown). The temperature of the lower layer was, however, colder on the left side and warmer on the right side than the homogeneous snowpack.

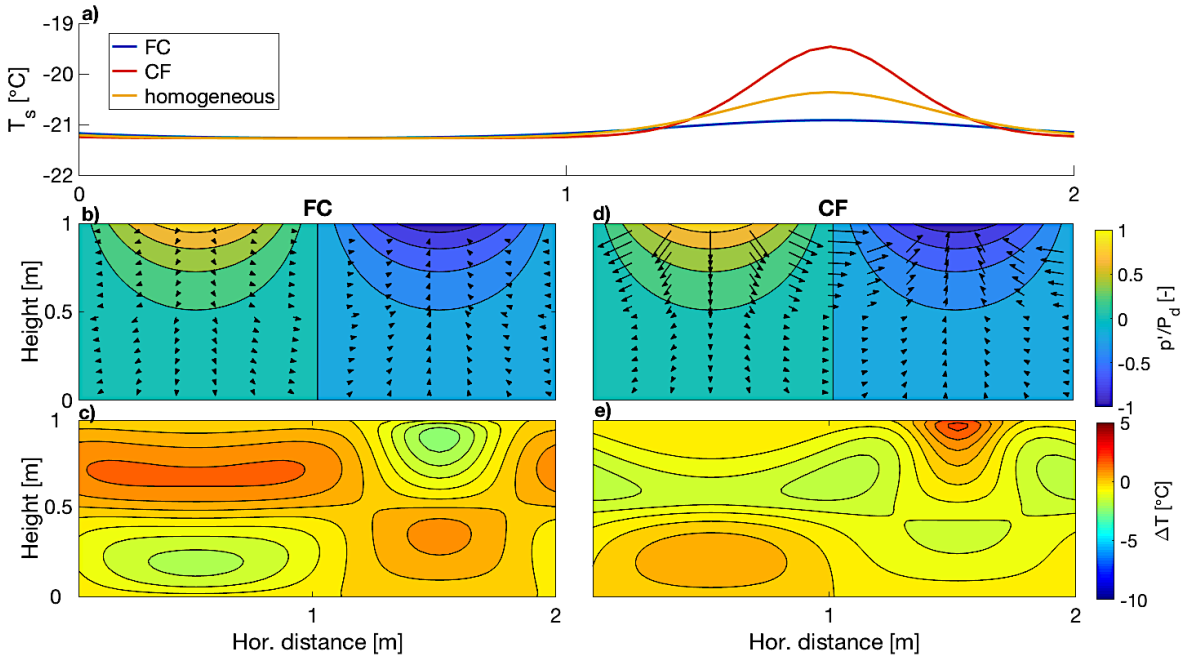

Figure 6.7 a) Simulated distributed snow surface temperature for a fine over coarse layered snowpack (FC, blue line), a coarse over fine snowpack (CF, red line), and a homogeneous snowpack (yellow line) for a 2 m long and 5 cm high snow dune. **b)** and **d)** present the pressure distribution and airflow direction and magnitude (arrows) in the snowpacks FC and CF, respectively. **c**) and **e**) present the difference of simulated internal temperature between the FC and the homogeneous snowpacks and between the CF and homogeneous snowpacks, respectively.

6.6 Discussion

Thermal convection within snow, initiated by topography-driven air ventilation, impacted both the distribution of temperature within the snowpack and the lateral distribution of snow surface temperature. The pressure perturbation at the snow surface was the lowest where upward airflow occurs within the snowpack. Here, the advection of heat through the snow resulted in zones of high thermal gradients within the snowpack, while the advection of heat decreased the temperature gradient in the upper snowpack where the surface pressure perturbation was maximal, as concluded by *Albert* (1993). Under natural conditions, these zones impact the transport of water vapour and kinematic snow metamorphism. Including thermal convection in an avalanche model could help predict conditions of kinetic metamorphism associated with weak layers capable of triggering avalanches.

Snow dunes, as well as sastrugi, can result from wind redistribution (*Pomeroy and Gray,* 1995*, Birnbaum et al.*, 2010, *Filhol and Sturm*, 2015). Dunes have been observed in different landscapes, from the Canadian Prairies (*Shook and Gray*, 1992) to mountain alpine (*Schirmer and Lehning*, 2011) to Arctic tundra with a length scale of 6 m (*Sturm et al*., 2001). Here, snow surface heterogeneities were characterized by their height and wavelength, each impacting airflow through snow and thus the convection of heat through snow. The advection of heat was more affected by variations in dune height than variations in dune wavelength; stronger heat convection was simulated in taller and shorter wavelength snow dunes due to stronger and narrower pressure fluctuations at the snow surface, respectively. *Colbeck* (1989) and *Albert* (1996) also showed that airflow decreases for longer surface pressure forcing wavelengths. Under specific circumstances (e.g. high wind), compaction of the snow surface may occur during wind scouring, resulting in the formation of wind slabs (e.g. *Alley*, 1988; *Jones et al.*, 1999; *Sommer et al*., 2017) of low permeability that would prevent penetration of air from the atmosphere to the snowpacks. Similarly, ice layers have near zero permeability and can completely restrict convection (*Van Bochove et al.*, 2001).

At the surface of the snowpack, the energy balance was solved to estimate the exchange of energy between atmosphere and snowpack, which was used as upper boundary condition for the heat transport equation. Because the results are presented at steady state, the assumption that this surface exchange layer has no-mass is reasonable. The energy balance was driven by meteorological data: air temperature, relative humidity, wind speed, and incoming longwave and shortwave radiation. The sensitivity of the model to air temperature and wind speed, which were varied alongside snow dune height and dune wavelength, was evaluated. ΔT_s decreased (i.e. the snow surface temperature became more homogeneous) with warmer air temperatures. This decrease was less significant for smaller dunes. For longer snow dunes, ΔT_s decreased faster with colder air temperatures. Changes in wind speed had a greater effect on ΔT_s than did the air temperature (Fig. 6.3b). Surprisingly, the maximum snow surface temperature had a non-monotonic behaviour with increasing dune wavelength for a strong wind speed (10 m s^{-1}) (Fig. 6.5); its value peaked for a dune length of 5 m.

Deviations in snow properties (density, grain size, and snow depth) also affected the simulation of thermal convection and therefore the snow surface temperature. The changes in grain size and

snow density primarily impacted snow permeability and thus velocity of airflow within the snow; increasing grain size or decreasing snow density resulted in an increase in snow permeability. *Albert* (1996) demonstrated through numerical modelling that changes in layer permeability impacted the airflow velocity. In this research, it was observed that changes in snow density had a greater impact on simulated snow surface temperature than variations in snow grain size (Fig. 6.6). Changes in snow depth impacted the depth reached by the airflow. Increasing snow depth was similar to decreasing snow dune height, i.e. the taller the snowpack, the less energy from the bottom of the snowpack could be transported to the upper snowpack through thermal convection; thus, a more homogeneous snow surface temperature was estimated for deeper snowpacks. In addition, this research showed that assuming a homogeneous snowpack when simulating heat convection has some limits, as originally demonstrated by *Albert* (1996). *Colbeck* (1997) showed the impact of ice layers on air ventilation through snow. Here, the focus was on comparing heat convection through a homogeneous snowpack against heat convection through a 2-layer snowpack of equivalent averaged properties. The vertical layering system of the snow greatly impacted airflow through snow, and the snow internal temperature and snow surface temperature distributions were different than in a homogeneous snowpack. As previously shown in *Albert* (1996), a low-permeability surface layer (either a dense or fine snow layer) reduces the airflow in the underlying layer. This limited heat advection occurring below the surface and resulted in a quasi-uniform estimated snow surface temperature distribution (Fig. 6.7a). However, the temperature distribution in both layers still differed from that of a homogeneous flat snowpack (Fig. 6.7c).

Local thermal equilibrium between the ice and air phases was assumed. It can be expected, however, that air penetrating the snow surface where the pressure is at a minimum (Fig. 6.1) has a different temperature than the snow matrix. The Darcy velocity of the air phase ($|\boldsymbol{q}|$ in Eq. 6.9) was higher than or equal to 0.0024 m s^{-1} within the upper 20 cm (where the exchange of energy between the air phase and the ice phase can be expected to occur) of a 1-m homogeneous snowpack of density equal to 300 kg m^{-3} and a grain size of 1 mm, with a wind speed of 5 m s^{-1} above the snow surface. This assumption was verified by estimating the evolution of the difference of temperature between the air and ice phases, assuming they initially differ by 5°C (Appendix C). This simple calculation using Newton's law of cooling showed that if the two phases have different initial temperatures, thermal equilibrium through will be reached very quickly (<0.005 s). The

local thermal equilibrium assumption is thus appropriate. The results from this study were presented at steady state; thus, thermal equilibrium between the different phases is an appropriate assumption in this case. Under natural conditions, due to the turbulent nature of the wind above the surface (e.g. *Aksamit and Pomeroy*, 2017), steady state is unlikely to be reached. The pressure perturbation at the surface was assumed invariant in time; this assumption should little effect on the model results if the frequency of the surface pressure perturbation is between 0.1 and 10 Hz (*Albert*, 1996). These results present an ideal case and further explain the impact of dune characteristics and snow properties on thermal convection through snow.

6.7 Conclusions

The impact of thermal advection initiated by topography-induced airflow on snow internal and near surface temperatures was investigated. The input heat flux was estimated by solving for the energy balance at the snow surface, using meteorological data to drive the model. Increasing dune height resulted in an increase in heat convection and therefore in more spatial variability in estimated snow surface temperature. Heat convection within the snowpack decreased with increasing dune wavelength, resulting in a more homogeneous snow surface temperature. The near snow surface temperature was, however, more varied for a colder air temperature and a higher wind speed above the snow surface.

Airflow velocity within the snowpack was, in part, controlled by snow permeability. As permeability decreased with increasing snow density and decreasing grain size, the air convection within the snow became weaker and the surface temperature became more homogeneous. For an increasing snow depth, heat convection was contained in the upper layer of the snowpack and had little effect on internal temperature distribution. In addition, the vertical layering system of the snowpack greatly affected the thermal convection within snow and the resulting snow surface temperature. These numerical results show that topography-driven thermal convection through snow can be significant in cold snowpacks during early- and mid-winter, when the snow accumulation is no greater than 1.5 m, and the snow density is still low. As the snowpack warms up and densifies in the late-winter and spring, thermal convection will not affect snow surface temperature. Further research is needed to confirm the presence of this phenomenon in nature and to validate the model proposed here.

6.8 References

Aksamit, N.O. and Pomeroy J.W. (2017), The Effect of Coherent Structures in the Atmospheric Surface Layer on Blowing-Snow Transport, Boundary-Layer Meteorology, 1-23, doi: 10.1007/s10546-017-0318-2

Aksamit, N. O., and J. W. Pomeroy (2018), Scale Interactions in Turbulence for Mountain Blowing-Snow, Journal of Hydrometerology., 19, 305-320, doi:10.1175/JHM-D-17-0179.1

Albert, M.R (1993), Some numerical experiments on firn ventilation with heat transfer, *Annals of Glaciol.*, 18.

Albert, M.R. (1996), Modeling heat, mass, and species transport in polar firn, *Annals of Glaciol.*, 23.

Albert, M. R., and J. P. Hardy (1995), Ventilation experiments in a seasonal snow cover, *IAHS Publ.*, 41–49.

Alley, R. B. (1988), Concerning the deposition and diagenesis of strata in polar firn, *J. Glaciol*., 34(118), 283–29

Andreas, E. L., Jordan, R. E., and A. O. Makshtas (2005), Parameterizing turbulent exchange over sea ice: the ice station Wedell results, *Boundary-Layer Meteorology*, 114, 439-460, https://doi.org/11007/s10546-004-1414-7

Bartlett, S. J., and M. Lehning (2011), A theoretical assessment of heat transfer by ventilation in homogeneous snowpacks, *Water Resour. Res*., 47, 1–7, doi:11029/2010WR010008.

Birnbaum, G., et al. (2010), Strong-wind events and their influence on the formation of snow dunes: observations from Kohnen station, Dronning Maud Land, Antarctica, *Journal of Glaciology*, 56(199), 891-902, doi:13189/002214310794457272.

Brown, R., P. Bartlett, M. MacKay, and D. Verseghy (2006), Evaluation of snow cover in CLASS for SnowMIP, *Atmosphere-Ocean*, 44, 223–238, doi:13137/ao.440302.

Brun, E., E. Martin, V. Simon, C. Gendre, and C. Coleou (1989), An energy and mass model of snow cover suitable for operational avalanche forecasting, *J. Glaciol.*, 35, 333–342.

Calonne, N., Flin, F., Morin, S., Lesaffre, B., Rolland du Roscoat, S., and C. Geindreau (2011), Numerical and experimental investigations of the effective thermal conductivity of snow, *Geophys. Res. Lett.*, 38, L23501, doi:11029/2011GL049234.

Calonne, N., Geindreau, C., Flin, F., Morin, S., Lesaffre, B., Rolland Du Roscoat, S., and P. Charrier (2012), 3-D image-based numerical computations of snow permeability: links to specific surface area, density, and microstructural anisotropy, The Cryosphere, 6, 939–951, doi: 15194/tc-6-939-2012.

Clarke, G. K. C., and E. D. Waddington (1991) A three-dimensional theory of wind pumping, *J. Glaciol.*, 37, 89–96, doi:11017/S002214300004283

Clarke, G. K. C., D. A. Fisher, and E. D. Waddington (1987), Wind pumping: A potentially significant heat source in ice sheets, *Phys. Basis Ice Sheet Model, IAHS Publ.*, 169–18

Clifton, A., C. Manes, J. D. Rüedi, M. Guala, and M. Lehning (2008), On shear-driven ventilation of snow, *Boundary-Layer Meteorol.*, 126, 249–261, doi:11007/s10546-007-9235-

Colbeck, S. C. (1997), Model of wind pumping for layered snow, *J. Glaciol.*, 43, 60–65.

Colbeck, S. C. (1989) Air movement in snow due to windpumping, *J. Glaciol.*, 35, 209–213.

Conway, J.P., Pomeroy, J.W., and W.D. Helgason (2018), Challenges in modelling turbulent heat fluxes to snowpacks in forest clearing, *Journal of Hydrometeorology,* in review.

Cullen, N. J., Steffen, K., and P. D. Blanken (2007), Nonstationarity of turbulent heat fluxes at Summit, Greenland, *Boundary-Layer Meteorology,* 122(2), 439-455, doi:1007/s10546-006-9112-2.

Cunningham, J., and E. D. Waddington (1993), Air flow and dry deposition of non-sea salt sulfate in polar firn: Paleoclimatic implications, *Atmos. Environ. Part A, Gen. Top.*, 27, 2943–2956, doi:11016/0960-1686(93)90327-U.

Dozier, J., and S. G. Warren (1982), Effect of viewing angle on the infrared brightness temperature of snow, *Water Resour. Res.*, 18(5), 1424–1434, doi:11029/WR018i005p01424.

Drake, S.A., Selker, J.S., and C. W. Higgins (2017), Wind enhances differential air advection in surface snow at sub-meter scales, *The Cryosphere*, 11, 2075-2087, doi:15194/tc-11-2075-2017.

Essery, R. (2015) A factorial snowpack model (FSM 1.0), *Geosci. Model Dev.*, 8, 3867-3876, https://doi.org/15194/gmd-8-3867-2015.

Filhol, S., and M. Sturm (2015), Snow bedforms: A review, new data, and a formation model, *J. Geophys. Res. Earth Surf.*, 120, 1645–1669, doi:11002/2015JF003529.

Gray, D.M. and P.G. Landine (1988), An energy-budget snowmelt model for the Canadian Prairies, *Can. J. Earth Sci.,* 25, 1292-1303.

Harder, P., and J. Pomeroy (2018), paper under review in *Journal of Hydrometeorology*.

Helgason, W., and J. Pomeroy (2012), Problems closing the energy balance over a homogeneous snow cover during midwinter, *J. Hydrometeorol.*, 13, 557–572, doi:11175/JHM-D-11-0135.1.

Holtslag, A., and H. De Bruin (1988), Applied Modeling of the Nighttime Surface Energy Balance over Land, *J. Appl. Meteorol.*, 27, 689–704, doi:11175/1520-0450(1988)027<0689:AMOTNS>2.CO;2.

Jones, H.G., Pomeroy, J.W, Davies, T.D., Tranter, M, and P. Marsh (1999), CO_2 in Arctic snow cover: landscape form, in-pack gas concentration gradients, and the implications for the estimation of gaseous fluxes, *Hydrological Processes*, 13, 2977-2989, doi: 10.1002/(SICI)1099-1085(19991230)13:18<2977::AID-HYP12>3.0.CO;2-#

Jordan, R. E., E. L. Andreas, and A. P. Makshtas (1999) Heat budget of snow-covered sea ice at North Pole 4, *J. Geophys. Res. Ocean.*, 104, 7785–7806, doi:11029/1999JC900011. http://doi.wiley.com/11029/1999JC900011.

Lapo, K. E., L. Hinkelman, M. Raleigh, and J. D. Lundquist (2015), Impact of errors in the downwelling irradiances on simulations of snow water equivalent, snow surface temperature, and the snow energy balance, *Water Resour. Res.*, 51, 1649–1670, doi:11002/2015WR017096.

Lehning, M., P. Bartelt, B. Brown, and C. Fierz (2002), A physical SNOWPACK model for the Swiss avalanche warning: Part III: Meteorological forcing, thin layer formation and evaluation, *Cold Reg. Sci.*, 35, 169–184.

Male, D. H., and R. J. Granger (1981), Snow surface energy exchange, *Water Resour. Res.*, 17, 609–627, doi:11029/WR017i003p00609.

Male, D.H., and D. M. Gray (1975), Problems in developing a physically based snowmelt model, *Canadian Journal of Civil Engineering*, 2(4), 474–488.

Monin, A. S., and A. M. Obukhov (1954), Basic laws of turbulent mixing in the surface layer of the atmosphere, *Contrib. Geophys. Inst. Acad. Sci. USSR*, 24, 163–187.

Paulson, C. A. (1970), The Mathematical Representation of Wind Speed and Temperature Profiles in the Unstable Atmospheric Surface Layer, *J. Appl. Meteorol.*, 9, 857–861, doi:11175/1520-0450(1970)009<0857:TMROWS>2.CO;2.

Pomeroy, J. W., Essery, R. L. H., and W. D. Helgason (2016), Aerodynamic and Radiative Controls on the Snow Surface Temperature, *J. Hydrometeorol.*, 17, 2175–2189, doi:11175/JHM-D-15-0226.1.

Pomeroy J.W. and Gray D.M. (1995), Snowcover Accumulation, Relocation and Management, *Division of Hydrology*: NHRI Science Report No. 7, 1-135

Powers, D., O'Neill, K., and S. C. Colbeck (1985), Theory of natural convection in snow, *J. Geophys.*, 90, 641–649.

Shook, K., and D. M. Gray (1992), Small-scale spatial structure of shallow snow covers, *Hydrological Processes*, 10, 1283-1293.

Sommer, C. G., Lehning, M., and C. Fierz (2017), Wind tunnel experiments: saltation is necessary for wind-packing, *Journal of Glaciology*, 53. http://doi.org/11017/jog.2017.53

Sturm, M. (1991), The role of thermal convection in heat and mass transport in the subarctic snow cover, *CRREL Rep. 91-19,* U.S Army Cold Reg. Re. Eng. Lab., Hanover, N. H., 1991.

Sturm, M., Liston, G.E., Benson, C.S., and J. Holmgren (2001), Characteristics and growth of a snowdrift in arctic Alaska, USA, *Artic Antarctic Alpine Research*, 33, 319-329.

Van Bochove, E., Thériault, G., Rochette, P., Jones, H.G., and J.W. Pomeroy (2001), Thick ice layers in snow and frozen soil affecting gas emissions from agricultural soils during winter, *Journal of Geophysical Research*, 106, 23061-23071

Vionnet, V., E. Brun, S. Morin, a. Boone, S. Faroux, P. Le Moigne, E. Martin, and J.-M. Willemet (2012), The detailed snowpack scheme Crocus and its implementation in SURFEX v7.2, *Geosci. Model Dev.*, 5, 773–791, doi:15194/gmd-5-773-2012.

Waddington E, and J. Cunningham (1996), The effect of snow ventilation on chemical concentrations. Wolff EW, Bales RG (eds) Chemical exchange between the atmosphere and polar snow, NATO ASI series, 143, 403–451.

CHAPTER 7

CONCLUSIONS

7.1 Concluding Remarks

The motivation for this research was to improve the theories applied in snowmelt numerical modelling in order to better estimate the magnitude and timing of snowmelt runoff generation. This thesis focusses on developing new theories and new numerical methods to better represent the physical processes involved in the infiltration of meltwater through subfreezing snowpacks and on the energetics of snowpacks. The formation and propagation of preferential flow paths in snow were of particular interest, as they greatly impact the rate of meltwater delivery to the base of the snowpack. The main conclusions of this research with regards to the objectives presented in Chapter 1 are summarized below:

Objective 1: What factors control the formation and development of preferential flow paths and ice layers in snow?

Chapters 2 and 3 present the development of a 2D snowmelt model (SMPP) that simulates the coupling of water flow with heat transfer, as well as the formation of preferential flow paths. Preferential flow was represented in the model by including single-value water entry pressure for initially dry snow, combined with heterogeneities in snow density and grain size. The use of single-value capillary pressure for dry snow was a simple macroscale representation of dynamic effects at pore-scale to represent a holdback and pile-up at the wetting front that is a characteristic of preferential flow paths (*Eliassi and Glass*, 2002). For the first time in a snowpack model, ice layers were represented at capillary barriers. The representation of preferential flow in the model was crucial for the formation of ice layers, and preferential flow paths permitted the percolation of meltwater to dry and cold snow zones. This model was compared to two sets of laboratory data; measured capillary overshoots within three snow samples and vertical distributions of liquid water content within four snow samples were qualitatively and quantitatively well represented.

A field study was conducted to evaluate the model presented in Chapters 2 and 3 against melt data from a natural snowpack (Chapter 4). Initial and boundary conditions were measured in the field,

and used to drive the model; snowmelt outflow was measured in the field with a lysimeter and was compared to predicted snowmelt outflow. The model performed poorly when compared with field observations, in particular because SMPP was unable to simulate preferential flow when using natural snowpack properties, resulting in a delay in the estimated snowmelt outflow. These findings were instructive, and it is suspected that the empirical equation of water entry pressure, determined from laboratory data (*Katsushima et al.*, 2013), is not adequate for natural snow properties, particularly for snow densities below 350 kg m^{-3}. This finding motivated the search for a new way to simulate preferential flow in snow; this is presented in Chapter 5.

Objective 2: To what degree do pressure relationships control water retention and flow in snow?

In SMPP (Chapters 2 and 3), capillary pressure hysteresis was introduced for the first time in a snowmelt model. Capillary hysteresis had an important effect on meltwater routing: it impacted the shape and length of preferential flow paths, as well as the values of water content within the snowpack. The use of water entry pressure to estimate capillary pressure within air-dry snow pores was necessary to simulate preferential flow and capillary overshoot in Chapters 2 and 3. This simple macroscale model was deemed not realistic to simulate capillary pressure overshoot in soil (*DiCarlo*, 2007). Its applicability in natural snow was questioned in Chapter 4 after evaluating the model against field data. This led to the work presented in Chapter 5.

In Chapter 5, a new water retention curve was developed to avoid the use of water entry pressure. This new water retention curve included a main wetting curve that started at a water content equal to zero and a main drainage curve that started at a residual water content, determined from experimental drainage data. The drainage scanning curves, initiating from the main wetting curve, were determined using an entrapment model for the wetting phase. This new hysteretic water retention curve was included in a 1D model to simulate water flow through snow. A dynamic capillary pressure in the Richards equation was introduced to account for transient effects when liquid water is redistributed within the pore space during infiltration. This model successfully simulated capillary pressure overshoots observed in different snow samples under various influxes, as well as saturation overshoots. As capillary and saturation overshoots are the cause of unstable flow in 2D or 3D, implementing this new theory of capillary pressure in a multi-dimensional snowmelt model should result in the simulation of preferential flow in snow.

Objective 3: Can a convective heat flux within a snowpack enhance the snow energetics estimate?

In SMPP presented in Chapters 2 and 3, only heat conduction was considered as a heat mechanism. Chapter 6 presents a new version of SMPP that includes topography-driven air flow through snow, which resulted in a heat convection flux that was coupled with the energy balance near the snow surface. The effect of heat convection on simulated near snow surface temperature was analysed. Including thermal convection within a snowpack resulted in a non-uniform near snow surface temperature. The maximum and minimum values of near snow surface temperature differed by a few degrees and were affected by the height and length of the snow dunes, as well as the snow internal properties (density, grain size, and snow depth). This research is a step forward to better understand the coupling of heat transfer within snowpacks with the energy balance above the snow.

7.2 Concluding Discussion

There has been an increasing interest in better simulating the flow of water through snowpacks in order to enhance the prediction of snowmelt runoff. This process is usually simplified in operational snowmelt models to reduce the computational cost of these models. Only recently preferential flow was included in the operational snow model SNOWPACK (*Würzer et al.*, 2017) using a dual-domain approach. While this is a significant step forward, the approach has limitations that only a model with more physical realism can overcome. *Hirashima et al.* (2014, 2017) developed a 3D research snow model that simulates matrix and preferential flows in small snow samples. This model is limited to mass flow, applies a simplified representation of the water retention curve, and has not been compared to natural snowmelt data. The research presented in this thesis builds from the work of *Hirashima et al.* (2014, 2017) and addresses some of the main limitations. Particularly, this thesis presents an improved representation of the snow water retention curve by including a main wetting curve to the known main drying curve. Capillary hysteresis impacted the shape and length of preferential flow, as well as the distribution of liquid water within snowpacks (Chapters 2 and 3). The advanced capillary hysteresis model presented in Chapter 5 could (and maybe should) be included in 1D snow models that solve for Richards equation, instead of only applying a unique drying boundary curve for both wetting and drying flow processes.

From *Hirashima et al.* (2014, 2017), adding water entry pressure for dry snow to the Richards equation was necessary to simulate preferential flow in snow and capillary overshoot within snow samples. The use of water entry pressure was, however, questioned by *DiCarlo* (2007), who observed that the pressure at the tip of preferential flow paths is given by the main wetting curve. When evaluating the 2D model developed in Chapters 2 and 3, which uses a water entry pressure, it was hypothesized that the equation of water entry pressure for dry snow might not be suitable with natural snow properties (Chapter 4). Using a dynamic capillary pressure that depends on the rate of water infiltration provided better results than using a water entry pressure when simulating capillary pressure overshoot in three different snow samples (Chapter 5). This approach has been applied in recent soil studies to represent capillary and saturation overshoots, as well as preferential flow in soil (*Nieber et al.*, 2002; *Sander et al.,* 2008; *Chapwanya and Stockie,* 2010). This novel approach raises questions about the snow pore scale processes responsible for dynamic non-equilibrium effects. In soils, some explanations are the entrapment of water within the pores, a dynamic contact angle, and microscale heterogeneities (*Diamantopoulos and Durner*, 2012); they can be expected to also create dynamic non-equilibrium effects in snow pores; wet snow metamorphism might also be of great importance to cause dynamic non-equilibrium pore scale processes.

Wind pumping in snow has received little interest in the last decade. There is a consensus that the predominant trigger of wind pumping in snow is snow surface topography (*Colbeck*, 1989; *Waddington and Cunningham,* 1996; *Clifton et al.*, 2008). Models that simulate wind pumping in homogeneous and layered snowpacks have been developed (e.g. *Colbeck*, 1989, 1997; *Clarke and Waddington*, 1991), as well as the resulting thermal convection within snow (e.g. *Albert and McGilvary,* 1992; *Bartlett and Lehning*, 2011). During a study on closure of the energy balance over snow, *Helgason and Pomeroy* (2012) hypothesized that the presence of sastrugi at the snow surface could have resulted in thermal convection within the snowpack, which could have impacted snow surface temperature. The results from Chapter 6 confirm this hypothesis. Thermal convection from topography-driven airflow enhanced heat transfer from the near snow surface and the internal snowpack, and from the bottom of the snowpack to the internal snowpack. This resulted in a non-uniform snow surface temperature distribution. Snow internal properties and meteorological data impacted the simulated snow surface temperature. These results are only qualitative and an experimental campaign is needed to measure air velocity within the snowpack,

internal heat transfer, and snow surface temperature over a snow dune. This research gives insight into better understanding the coupling between the lower atmosphere and snowpacks on the ground. It should be verified by field measurements in natural conditions.

7.3 Outlook

Certain next steps in snow science can be drawn from this research. Chapter 4 suggests that future work is needed to improve the simulation of preferential flow paths in natural snowpacks. Chapter 5 presented a potential next step with a novel method to simulate capillary pressure and saturation overshoots. According to *DiCarlo* (2007, 2013), these overshoots are the cause of unstable flow. Therefore, the simulation of preferential flow paths can be expected in a multi-dimensional model that includes the water retention curve presented in Chapter 5 and a dynamic capillary pressure in the Richards equation. When this multi-dimensional snowmelt model is developed, it should be evaluated against the experimental data of *Avanzi et al*. (2016) and the in-situ data presented in Chapter 4. This model will most likely be more efficient numerically as it will not include water entry pressure, which was the cause of slow numerical simulations in Chapters 2, 3, and 4.

In this thesis, wet snow metamorphism was not considered during meltwater infiltration through snow. Wet snow metamorphism is poorly understood and additional work is needed to better understand how snow grain size evolves for different water fluxes. This conclusion is shared with *Hirashima et al.* (2017). The evolution of grain size under the presence of liquid water could be quantified through pore-scale numerical simulations, using CT-scan images of snow samples (*Heggli et al.*, 2011) as initial geometry. *Avanzi et al.* (2017) showed the coupling between preferential flow paths and wet snow metamorphism. Similar experiments should be conducted to better understand how grain growth occurs under the presence of liquid water and to quantify it. Accounting for wet snow metamorphism during the simulation of preferential flow would most likely impact the size of preferential flow paths and velocity of the water flux within them.

As snow models become more complex and more accurately represent snow physical processes, there will be an increasing need for accurate natural snowmelt data at small scales for model evaluation. Similar field studies as the one presented in Chapter 4 should be conducted on different terrains, with different snowpacks of various slope angles. The snowpack initial conditions will have to be more accurately measured (e.g. measuring the optical grain size and snow density of

each snow layer instead of at a 10 cm interval) in order to avoid uncertainties in model predictions. In addition, field measurements of ice layers would be necessary to appropriately parameterize them in snow models.

The model and theory of wind pumping presented in Chapter 6 need to be tested in real snowpacks. A similar field experiment as in *Helgason* (2009), who observed snow dunes at a site in the Canadian Prairies and hypothesized that wind pumping might have occurred and affected the snow surface energy balance, could be conducted. The snow internal temperature could be measured with an array of thermocouples of horizontal length similar to the wavelength of snow dunes. The array of thermocouples should be positioned in the field prior to the first snowfall and would be buried as snow accumulates over winter. This would allow the measurement of 2D snowpack internal temperature distribution over winter. The array of thermocouples should be placed close to a meteorological station to relate changes of snow internal temperature to meteorological conditions above the snowpack. Of particular interest would be changes of snow internal temperature with wind speed, in order to identify the occurrence of wind pumping within the snowpack. In addition, snowpit measurements should be conducted close to the meteorological station to obtain data of snow internal density, grain size an layer structure that could be used for model comparison. An infrared camera could be mounted on the meteorological station to take time-lapse pictures of the snow surface above the buried array of thermocouples in the snowpack. This could inform on the potential link between the radiative snow surface and the snowpack and the potential impact of wind pumping on the radiative snow surface temperature.

7.4 References

Albert, M.R., and W.R. McGilvary (1992), Thermal effects due to air flow and vapor transport in dry snow, *J. of Glaciology*, 38(129).

Avanzi, F., Petrucci, G., Matzl, M., Schneebeli, M., and C. De Michele (2017), Early formation of preferential flow in a homogeneous snowpack observed by micro-CT, *Water Resour. Res.*, 53, 3713–3729, doi:11002/2016WR019502.

Bartlett, S.J., and M. Lehning, (2011), A theoretical assessment of heat transfer by ventilation in homogeneous snowpacks. *Water Resour. Res.*, 47, 1–7, doi:10.1029/2010WR010008.

Clarke, G.K. C., and E. D. Waddington, (1991), A three-dimensional theory of wind pumping. *J. Glaciol.*, 37, 89–96, doi:10.1017/S0022143000042830.

Clifton, A., C. Manes, J. D. Rüedi, M. Guala, and M. Lehning, (2008), On shear-driven ventilation of snow. *Boundary-Layer Meteorol.*, 126, 249–261, doi:10.1007/s10546-007-9235-0.

Colbeck, S.C. (1989), Air movement in snow due to windpumping. *J. Glaciol.*, 35, 209–213.

Colbeck, S.C. (1997), Model of wind pumping for layered snow. *J. Glaciol.*, 43, 60–65.

Diamantopoulos, E., and W. Durner (2012), Dynamic nonequilibrium of water flow in porous media: a review, *Vadose zone Journal,* Special Section: MUSIS, doi:10.2136/vzj2011.0197.

DiCarlo, D.A. (2007), Capillary pressure overshoot as a function of imbibition flux and initial water content, *Water Resources Research*, 43, W08402, doi:10.1029/2006WR005550.

Eliassi, M., and Glass, R.J. (2002), On the porous-continuum modeling of gravity-driven fingers in unsaturated materials: Extension of standard theory with a hold-back-pile-up effect, *Water Resources Research*, 38(11), 1234, doi:11029/2001WR001131.

Helgason, W.D. (2009), Energy fluxes at the air-snow interface. Ph.D. dissertation, University of Saskatchewan.

Helgason, W. and Pomeroy, J. (2012). Problems closing the energy balance over a homogeneous snow cover during midwinter. *Journal of Hydrometeorology*, 13:557–572.

Hirashima, H., Avanzi, F., and S. Yamaguchi (2017), Liquid water infiltration into a layered snowpack: evaluation of a 3-D water transport model with laboratory experiments, *Hydrol. Earth Syst. Sci.,* 21, 5503-5515, https://doi.org/15194/hess-21-5503-2017.

Hirashima, H., Yamaguchi, S., and T. Katsushima (2014), A multi-dimensional water transport model to reproduce preferential flow in the snowpack, *Cold Regions Science and Technology*, 108, 80-90, doi:11016/j.coldregions.2014.09.004.

Katsushima, T., Yamaguchi, S., Kumakura, T., and A. Sato (2013), Experimental analysis of preferential flow in dry snowpack, *Cold Regions Science and Technology*, 85, 206-216, doi:11016/j.coldregions.2012.09.012.

Waddington E, and J. Cunningham, 1996: The effect of snow ventilation on chemical concentrations. Wolff EW, Bales RG (eds) Chemical exchange between the atmosphere and polar snow, NATO ASI series, 143, 403–451.

Würzer, S., Wever, N., Juras, R., Lehning, M., and Jonas, T. (2017), Modelling liquid water transport in snow under rain-on-snow conditions – considering preferential flow, *Hydrology and Earth System Sciences*, 21, 1741-1756, doi:10.5194/hess-21-1741-2014.

APPENDIX A: MODEL AVAILABILITY

The codes of the models presented in this thesis are available at the following URL:

https://github.com/nleroux3

APPENDIX B: FIELD DATA

In this appendix, the data collected and used in Chapter 4 are summarized. The instruments and methods used to collect the data are presented in Chapter 4.

April 1, 2015:

Measured heat fluxes from the hot plate to the snowpack:

Time	11:10	11:20	11:30	11:40	11:50	12:00	12:10	12:20	12:30
Heat flux 1 [W m^{-2}]	1082	1221	1020	868	921	932	904	776	843
Heat flux 2 [W m^{-2}]	387.4	985	929	863	952	892	885	841	996

12:40	12:50	13:00	13:10
738	697	762	799
865	778	747	610

Snow property measurements from two adjacent, vertical snow profiles:

Depth from surface [cm]	Temperature [^{o}C]	Density [kg m^{-3}]	Denoth meter value	Density [kg m^{-3}]	Denoth meter value
0-10	0	260	115	262	114
10-20	-1	250	112	241	110
30-40	-2	260	115	272	112
30-40	-1	297	116	321	114
40-50	0	325	115	327	114

The value of the Denoth meter for the air was equal to 97.

April 4, 2015:

Measured heat fluxes from the hot plate to the snowpack:

Time	11:00	11:10	11:20	11:30	11:40	11:50	12:00	12:10	12:20
Heat flux 1 [W m^{-2}]	823	1307	1150	1090	1003	998	883	984	815
Heat flux 2 [W m^{-2}]	806	1149	977	983	822	911	869	868	911

12:30	12:40	12:50	13:00	13:10	13:20	13:30
1050	737	689	788	759	760	799
956	1049	761	785	890	991	891

Snow property measurements from two adjacent, vertical snow profiles:

Depth from surface [cm]	Temperature [^{o}C]	Density 1 [kg m^{-3}]	Denoth meter value 1	Density 2 [kg m^{-3}]	Denoth meter value 2
0-10	0	380	117	298	117
10-20	0	276	116	300	122
30-40	0	347	125	310	126
30-40	-1	360	123	336	120
40-50	-1	345	119	338	120

The value of the Denoth meter for the air was equal to 101.

April 5, 2015:

Measured heat fluxes from the hot plate to the snowpack:

Time	11:10	11:20	11:30	11:40	11:50	12:00	12:10	12:20	12:30
Heat flux 1 [W m^{-2}]	657	1532	1267	1038	852	857	778	773	808
Heat flux 2 [W m^{-2}]	935	1187	1505	1276	1022	968	881	908	899

12:40	12:50	13:00	13:10	13:20	13:30
858	1007	708	866	964	843
956	977	812	869	858	629

Snow property measurements from two adjacent, vertical snow profiles:

Depth from surface [cm]	Temperature [^{o}C]	Density 1 [kg m^{-3}]	Denoth meter value 1	Density 2 [kg m^{-3}]	Denoth meter value 2
0-10	0	283	137	270	111
10-20	0	307	126	304	120
30-40	0	318	123	329	117
30-40	0	335	127	319	120
40-50	0	307	117	305	114

The value of the Denoth meter for the air was equal to 101.

April 8 2015:

Measured heat fluxes from the hot plate to the snowpack:

Time	11:10	11:20	11:30	11:40	11:50	12:00	12:10	12:20	12:30
Heat flux 1 [W m^{-2}]	260	490	646	696	706	714	719	690	698
Heat flux 2 [W m^{-2}]	210	463	553	639	667	692	668	719	664

12:40	12:50	13:00	13:10	13:20
750	857	702	652	677
984	789	589	591	608

Snow property measurements from two adjacent, vertical snow profiles:

Depth from surface [cm]	Temperature [^{o}C]	Density 1 [kg m^{-3}]	Denoth meter value 1	Density 2 [kg m^{-3}]	Denoth meter value 2
0-10	0	362	129	365	123
10-20	0	350	130	349	138
30-40	0	348	129	362	135
30-40	0	335	123	339	126
40-50	0	324	118	327	120
50-60	0	324	120	322	121
60-70	0	340	121	333	119

The value of the Denoth meter for the air was equal to 101.

APPENDIX C: NEWTON'S LAW OF COOLING AND THERMAL EQUILIBRIUM ASSUMPTION

The change of temperature of the air phase within the porous media (T_a), assuming thermal convection as the only heat mechanism, is:

$$\rho_\mathrm{a} C_{p_\mathrm{a}} \frac{\partial T_\mathrm{a}(t)}{\partial t} = h\,(T_\mathrm{a}(t) - T_\mathrm{i}), \tag{C.1}$$

where ρ_a is the air density, C_{p_a} is the specific heat capacity of the air, h is the heat coefficient and T_i is the temperature of the ice matrix. Here, we assume that the temperature of the ice matrix is constant and only the temperature of the air phase changes. Eq. C.1 becomes:

$$\Delta T_\mathrm{p}(t) = \Delta T_\mathrm{p}(0)\mathrm{e}^{-h/(\rho_\mathrm{a} C_{p_\mathrm{a}}\, t)}, \tag{C.2}$$

with $\Delta T_\mathrm{p}(t) = T_\mathrm{a}(t) - T_\mathrm{i}$.

From *Dixon and Cresswell* (1979), h can be expressed as:

$$h = a_\mathrm{fs} h^*, \tag{C.3}$$

with a_fs the specific surface area expressed by $a_\mathrm{fs} = 6(1-\phi)/d$, with ϕ the snow porosity and d the diameter of the particles, which are assumed spherical. h^* is given by (*Nield and Bejan*, 1992):

$$\frac{1}{h^*} = \frac{d}{\mathrm{N_u}\, k_\mathrm{a}} + \frac{d}{10\, k_\mathrm{s}} \tag{C.4}$$

with k_a and k_s the thermal conductivities of the air and ice phases, respectively, and $\mathrm{N_u}$ is the Nusselt number that can be expressed as follows for a forced convection in porous media (*Pallares and Grau*, 2010):

$$\mathrm{N_u} = 1 + \frac{4(1-\phi)}{\phi} + \frac{1}{2}(1-\phi)^5 \mathrm{Re_d^6 Pr}^{1/3}, \tag{C.5}$$

where $\mathrm{Re_d}$ is the particle Reynolds number ($\mathrm{Re_d} = \frac{\rho_a |\boldsymbol{q}| d}{\mu_a}$ with μ_a the dynamic viscosity of air), and Pr is the Prandtl number of the air phase.

Figure C.1 presents the difference of temperature between the air phase and the ice phase ($\Delta T_p(t)$) for an initial difference of temperature ($\Delta T_p(0)$) of 5°C, with T_i = 0°C. The velocity |q| of the air phase was taken equal to 2.4x10^{-3} m s^{-1}, which was the smallest the slowest velocity simulated within the top 20 cm (where the thermal convection between the air and ice phases could be expected to occur) of a 1-m homogeneous snowpack of density equal to 300 kg m^{-3} and a grain size of 1 mm, with a wind speed of 5 m s^{-1} two meters above the snow surface. The values for all the thermal properties of the ice and air phases were chosen for the phases at 0°C. It can be observed that the two phases reached thermal equilibrium at about t = 5 ms.

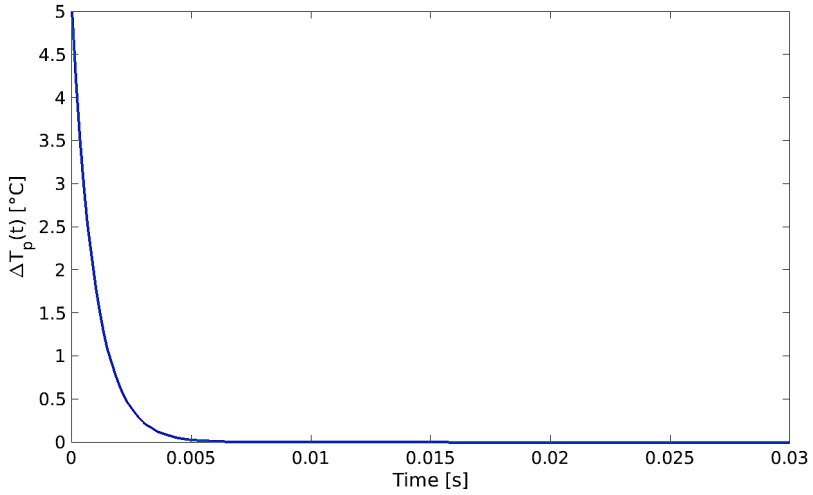

Figure C.1 a) Evolution of the difference of temperature between the air and ice phases ($\Delta T_p(t)$) for an initial difference of temperature of 5°C between the two phases, assuming a velocity of 2.4x10^{-3} m s^{-1} of the air phase, a snow density of 300 kg m^{-3}, and a grain size of 1 mm.

References

Dixon, A. G. and D. L. Cresswell (1979), Theoretical predictions of effective heat transfer mechanisms in regular shaped packed beds, *AIChE Journal*, 25, 663–676.

Nield, D.A and A. Bejan (1992), Convection in Porous Media, Springer, New York.

Pallares, J., and F. X. Grau (2010), A modification of a Nusselt number correlation for forced convection in porous media, *International Communications in Heat and Mass Transfer*, 37, doi:11016/j.icheatmasstransfer.20107.014.